

Fatigue Behavior of functionally graded Inconel 718 manufactured by selective laser melting

Saswat Sahu

Master of Science Thesis

Fatigue Behavior of functionally graded Inconel 718 manufactured by selective laser melting

MASTER OF SCIENCE THESIS

For the degree of Master of Science in Materials Science and
Engineering at Delft University of Technology

Saswat Sahu

January 17, 2020

Faculty of Mechanical, Maritime and Materials Engineering (3mE) · Delft University of
Technology



DELFT UNIVERSITY OF TECHNOLOGY
DEPARTMENT OF
MATERIALS SCIENCE AND ENGINEERING

The undersigned hereby certify that they have read and recommend to the Faculty of
Mechanical, Maritime and Materials Engineering (3mE) for acceptance a thesis
entitled

FATIGUE BEHAVIOR OF FUNCTIONALLY GRADED INCONEL 718 MANUFACTURED BY
SELECTIVE LASER MELTING

by

SASWAT SAHU

in partial fulfillment of the requirements for the degree of
MASTER OF SCIENCE MATERIALS SCIENCE AND ENGINEERING

Dated: January 17, 2020

Supervisor:

Dr. V.A. Popovich

Advisors:

Dr. Ton Riemsdag

Dr. Michael Janssen

Abstract

Functionally graded materials (FGMs) represent a new class of materials that consist of graded compositional and microstructural patterns allowing to tailor properties. Additive manufacturing (AM) or more commonly known as 3D-printing offers a paradigm shift in FGMs and engineering design due to its ability to produce components with complex geometries and functional part optimization. This study aims to investigate the concept of microstructural grading enabled via 3D-printing process and its feasibility to tailor site-specific fatigue behaviour.

Non-graded and graded specimens of Inconel 718 featuring a range of microstructural gradients were produced by selective laser melting (SLM). In the current work the grain size, crystallographic texture and precipitates, resulting in distinctly different properties, were used to develop microstructural gradients. Post-process heat treatment in terms of hot isostatic pressing (HIP) and aging was also investigated. Microstructural and elastic properties as well as in-depth fatigue crack growth behaviour were characterised and compared with conventionally manufactured wrought Inconel 718. Fatigue crack growth in FGMs under cyclic loading was investigated via novel experiments and FE approach. Results from homogeneous specimens were used for estimating spatial property distribution and crack-extension effect in the graded specimens. Hence, for the graded material a constant ΔK procedure was designed to investigate the change in crack growth rate as a function of different gradients. Additionally, Digital Image Correlation (DIC) and Potential Drop (PD) were conducted to validate the constant ΔK tests.

It was found that fatigue behaviour of the individual microstructures was primarily affected by the grain size, grain orientation and heat treatment. As opposed to the general trend, fine grain material (range of 10-70 μm) had a better fatigue crack propagation resistance than coarse grain (100 – 500 μm), which was attributed to the high compressive residual stresses developed during the 3D-printing. The crack growth rate in the graded material at a constant ΔK was found to change from one microstructure to the other following the same trend as the individual microstructures. The effect of grain orientation was found to significantly affect the crack growth rate, with grains elongated parallel to crack showing the larger and more continuous crack growth gradient. Additionally, in the heat treated (HIP+H/T) graded material, the difference in properties between the two gradients was almost entirely

diminished, indicating the necessity to optimize heat treatment regimens more suitable for developed herein FGMs.

The current study not only delivered fatigue parameters and FE model for various graded and non-graded 3D-printed Inconel 718, but also successfully demonstrated the feasibility of using 3D-printing process to alter the fatigue behaviour in FGMs components.

Table of Contents

Glossary	xv
List of Acronyms	xv
Acknowledgements	xvii
1 Introduction	1
2 Literature Review	3
2-1 Inconel 718- Material and Properties	3
2-1-1 Microstructure	4
2-1-2 Engineering Properties	7
2-2 Production of Inconel 718 (IN718)	8
2-2-1 Conventional Methods	9
2-2-2 Additive Manufacturing	10
2-2-3 Effect of Selective Laser Melting (SLM) on Microstructure	13
2-2-4 Effect of SLM on Mechanical Properties	16
2-3 Post process Heat-Treatments	17
2-3-1 Effect of AMS 5663/5383 on microstructure of SLM produced IN718	18
2-3-2 Effect of AMS 5663/5383 on mechanical properties of SLM produced IN718	20
2-3-3 Effect of AMS 5917 (Hot Isostaic Pressing (HIP)) on microstructure of SLM produced IN718	21
2-3-4 Effect of HIP on mechanical properties of SLM produced IN718	22
2-4 Fatigue properties of IN718	22
2-4-1 Crack Initiation	24
2-4-2 Crack Propagation	25
2-5 Functional Grading	28
2-5-1 Types of Functionally Graded Material (FGM)	28

2-5-2	Additive Manufacturing of FGM	29
2-5-3	Mechanical properties of FGM	30
2-5-4	Effect on fatigue and fracture mechanics in FGM	30
2-6	Conclusions	34
2-7	Problem statement and research questions	35
3	Materials and Methods	37
3-1	Materials	37
3-1-1	Manufacturing	37
3-1-2	Heat Treatment	38
3-1-3	Type and Dimension	38
3-2	Characterization	40
3-2-1	Microscopy	40
3-2-2	X-ray diffraction (XRD) analysis	41
3-2-3	Electron back-scatter diffraction (EBSD) analysis	41
3-2-4	Hardness	41
3-3	Fatigue	41
3-3-1	Set-up	42
3-3-2	Fatigue characterization of Ungraded specimen	43
3-3-3	Fatigue characterization of Graded specimen	46
3-3-4	Summary of tests	49
4	Results- Microstructural Characterization	51
4-1	Microscopy	51
4-1-1	Coarse Grain region	51
4-1-2	Interface region	55
4-1-3	Fine Grain region	57
4-2	Hardness	60
4-2-1	Ungraded Specimen	60
4-2-2	Graded Specimen	62
4-3	X-ray diffraction	64
4-3-1	Phase Identification	64
4-3-2	Residual Stress Measurement	65
4-4	EBSD	67
4-5	Summary	70
4-5-1	Microscopy	70
4-5-2	Hardness	71
4-5-3	X-ray diffraction (XRD)	71
4-5-4	Electron back-scatter diffraction (EBSD)	71

5	Results-Fatigue Behavior	73
5-1	FEM Simulation	73
5-1-1	Young's Modulus from displacement	73
5-1-2	Results of the model	74
5-2	Experimental	76
5-2-1	Fatigue Characterization of Ungraded specimens	76
5-2-2	Fatigue Characterization of Graded specimens	82
5-3	Digital Image Correlation	85
5-4	Summary	88
5-4-1	Ungraded specimens	88
5-4-2	Graded specimens	88
6	Relation between microstructural features and fatigue behavior	91
6-1	Research Question 1 : Evolution of microstructural features	91
6-1-1	Evolution of microstructure with respect to grain sizes	92
6-1-2	Evolution of microstructure with respect to different grain orientation and FGM	93
6-2	Research Question 2 : Effect of post process heat treatments on microstructure	94
6-3	Research Question 3 : Effect of microstructure on fatigue	94
6-3-1	Effect of grain size and grain orientation on fatigue	95
6-3-2	Effect of Heat treatment	98
6-4	Research Question 4 : Comparison of 3D printed and wrought Inconel 718	99
6-5	Research Question 5 : Effect of FGM on fatigue	99
7	Conclusions	103
7-1	Evolution of Microstructural features in SLM printed material	103
7-2	Effect of post process heat treatments on evolution of microstructures	103
7-3	Fatigue Behavior of SLM printed individual microstructures	104
7-4	Comparison of fatigue behavior in 3D printed and wrought Inconel 718	104
7-5	Effect of FGM on fatigue behavior	105
8	Future Recommendation	107
A	Chart showing the methodology	109
B	XRD setup and example of data analysis	111
C	Clamp drawing, setup summary	115
C-1	Clamp	116
C-2	Set-up	117
D	Young's modulus results from indentation method	119

E	Algorithm for reduction of MTS data	121
E-1	Step 1	121
E-2	Step 2	123
E-3	Step 3	126
F	Precision and accuracy	129
G	Fatigue plots of graded specimens	131
G-1	As processed	131
G-2	HIP+H/T	132
	Bibliography	133

List of Figures

2-1	Age Hardening response of Ni superalloys	4
2-2	γ dendrites in different grains	4
2-3	γ' and γ'' particles in AM IN718.	5
2-4	Delta phase on the grain boundaries.	6
2-5	Laves phase in the interdendritic spaces.	6
2-6	Different carbides in matrix.	7
2-7	Manufacturing of IN718 turbine blades	9
2-8	Schematic of a typical SLM setup	11
2-9	Schematic of component evolution in SLM and the different parameters	12
2-10	Microstructure of SLM printed material	13
2-11	Inverse pole figure (IPF) coloured map of as-built IN718 showing texture evolution	14
2-12	Dislocation networks observed in as-built IN718	15
2-13	Optical Micrograph of as-built IN718 showing 1) build direction 2) Gas pores 3) Lack of fusion void	15
2-14	IPF showing texture in heat treated SLM IN718	19
2-15	IPF showing grain orientation in HIPed SLM IN718	22
2-16	Example of FCGR curves	26
2-17	Tailored FGM composites with smooth transition in thermal properties	29
2-18	Types of FGM	29
2-19	Central crack in a layered infinite plate and the schematic of the stress distribution ahead of the crack tip	32
3-1	Figure showing manufacturing of the specimens along with the dimension	39
3-2	Experimental set-up from front	42
3-3	Experimental set-up from backside	43
3-4	Schematic of constant K_{max} procedure	44

3-5	Figure showing detail diagram of the notch	45
3-6	Figure showing reference marks. Bolts hammered into the specimen for the clamp can also be seen on the sides.	46
3-7	Mesh used in the Finite Element Modelling (FEM) analysis of the graded specimen.	48
3-8	Speckle pattern produced from paint sprays for DIC.	49
4-1	Coarse grain in AP-A specimens.	52
4-2	Coarse grain in AP-B	52
4-3	Electron micrograph of coarse grain in AP-A specimens	53
4-4	Electron micrograph of coarse grain in AP-B specimens	53
4-5	Electron micrograph of ungraded specimen AP-C	54
4-6	Electron micrograph of ungraded specimen AP-D	54
4-7	Electron micrograph of graded specimens HIP+H/T	55
4-8	Optical micrograph of graded specimen HIP+H/T-3	55
4-9	Electron micrograph of graded specimen HIP+H/T-4	56
4-10	Electron micrograph of ungraded specimen HIP+H/T-C	56
4-11	Electron micrograph of ungraded specimen HIP+H/T-D	57
4-12	Optical micrograph of graded specimen AP of the interface.	57
4-13	Optical micrograph of graded specimen AP of the interface 2.	58
4-14	Optical micrograph of AP graded specimen in fine grain side.	58
4-15	Electron micrograph of AP graded specimen showing fine grains.	59
4-16	Electron micrograph of ungraded specimen AP-E showing fine grains.	59
4-17	Electron micrograph of graded specimen HIP+H/T-A showing grains.	60
4-18	Electron micrograph of graded specimen HIP+H/T-B showing grains.	60
4-19	Electron micrograph of graded specimen HIP+H/T-A showing comparison of carbides in fine grain side and coarse grain side.	61
4-20	Electron micrograph of graded specimen HIP+H/T-B showing comparison of carbides in fine grain side and coarse grain side.	61
4-21	Electron micrograph of ungraded specimen HIP+H/T-E showing fine grains.	62
4-22	Vicker's Hardness in As-processed specimens.	63
4-23	Vicker's Hardness in HIP+H/T specimens.	63
4-24	XRD peaks for different phases in all the specimens.	65
4-25	Plot showing XRD plots for both the batches	65
4-26	EBSD results of specimen AP-C	68
4-27	EBSD results of specimen AP-D	68
4-28	EBSD results of specimen AP-E	69
4-29	EBSD color map of H/T wrought specimen	69
5-1	Results of the FEM showing variation of K in graded specimen	74
5-2	Fit of the new $f(a/W)$	75

5-3	Fatigue curves of all the ungraded specimens	78
5-4	Fatigue curve of H/T wrought specimens	79
5-5	Summary of fatigue curves of all the ungraded specimens.	79
5-6	Constant ΔK test results for as-processed specimens.	83
5-7	Constant ΔK test results for HIP+H/T specimens.	84
5-8	DIC image in AP-B specimen	86
5-9	DIC images for HIP+H/T-A at interface	87
5-10	DIC images for HIP+H/T-B at interface	87
6-1	Etched rack path in specimen AP-C	96
6-2	Etched crack path in specimen AP-D	96
6-3	Etched crack path in specimen AP-E	97
6-4	Etched crack path in HIP+H/T-C	97
6-5	Etched crack path in HIP+H/T specimen	98
6-6	Unetched crack path in AP specimen	98
A-1	Flowchart of the methodology adopted in this project	110
B-1	Arrangement of the specimen in the machine	112
B-2	Schematic describing measurement positions in the specimens	113
B-3	$d v/s \sin^2(\psi)$ example showing curvy variation. This was attributed to either a presence of shear stress or a stress gradient along the depth.	114
C-1	Drawing of the clamp	116
C-2	Specimen preparation chart	117
C-3	Chart showing the setup	117
D-1	Indentation test results for specimen AP-A	119
D-2	Indentation test results for specimen AP-B	120
D-3	Indentation test results for specimen HIP+H/T-A	120
D-4	Indentation test results for specimen HIP+H/T-B	120
G-1	Constant ΔK test results for as-processed specimens.	131
G-2	Constant ΔK test results for HIP+H/T specimens.	132

List of Tables

2-1	Tensile properties of IN718	8
2-2	Tensile properties of as-built IN718 as compared to cast and wrought counterparts.	16
2-3	Standard Heat treatments defined by the SAE	17
2-4	Summary of properties after different processes	20
2-5	Effect of HIP and heat treatment on mechanical properties	22
2-6	Paris exponent values and Paris range of ΔK for different stress ratio in forged IN718	28
2-7	Table showing different mechanical properties corresponding to different laser powers.	30
3-1	Table showing parameters used in the Selective Laser Melting (SLM) process . .	38
3-2	Table showing the Heat treatments applied	38
3-3	Table showing the nomenclature of the various specimens	40
3-4	Table summarizing all the tests performed for each batch in this project	50
4-1	Table summarizing hardness values of ungraded specimens	61
4-2	Table showing XRD results in ungraded specimens	66
4-3	Table showing XRD of graded specimens	67
4-4	Average grain sizes in AP specimens	69
5-1	Table summarizing E modulus of ungraded specimens	73
5-2	Table showing threshold values of the specimens. Load values corresponding to a cracklength at 2 mm are also shown.	76
5-3	Table showing the Paris constants of all the ungraded specimens	80
5-4	Table showing the crack growth rates in graded specimens at constant ΔK with comparison to the corresponding ungraded microstructures.	85
5-5	Table summarizing the fatigue parameters used to assess both graded and ungraded specimens.	88
E-1	Sample of raw MTS data	121

E-2	Sample data after step 1	122
E-3	Sample data after step 2 reduction	125
E-4	Sample data after final step	127
F-1	Average Error in crack-length measurement indifferent groups	129

Glossary

List of Acronyms

AM	Additive Manufacturing
DCPD	Direct current potential drop
SENB	Single edge notched bending
XRD	X-ray diffraction
EBSD	Electron back-scatter diffraction
FGM	Functionally Graded Material
SLM	Selective Laser Melting
HIP	Hot Isostatic Pressing
FEM	Finite Element Modelling
BD	Building direction
AP	As-Processed
H/T	Heat Treatment

Acknowledgements

I would like to thank my supervisor, Dr. Vera Popovich for being constantly patient and supportive not just in this thesis but throughout the second year of my masters. I consider myself immensely fortunate to have worked under her guidance which has inspired me to become not just a better material scientist but also a good human. I am immensely grateful to her to trust me with this challenging project that made me realize my potential in the true sense. The last year has increased not just my intellectual capability but also my emotional endurance. Through all this, Dr. Popovich has been a true guide and leader to me.

The project could not have been complete without Dr. Ton Riemsdag and Elise Rienton who I consider the magicians of the Mechanical Lab. I see myself just as the body of a car whose engines are basically these two immensely talented people. It is through their help that I was able to arrange the difficult set-up of my experiments. I remember annoying them with one problem after another which was always received enthusiastically. It is because of these happy people that I did not 'fatigue' on days where the experiments took annoyingly long time. They always made sure that I am doing OK, although as trivial as it may sound, which meant a lot to me. It has been a delight working with them and I offer my sincerest of gratitude towards them. This project is actually not mine it is ours.

Thanks are due to Dr. Michael Janssen for sharing his expert knowledge on fatigue in our meetings. It was through Dr. Michael Janssen's works that I was inspired to undertake a project on fatigue. In the project as well, it was through his experienced knowledge that we could anticipate many technicalities of the project. My best memories from the project involves myself presenting results in our weekly meetings and Dr. Michael Janssen questioning the validity of my results. It was my good fortune that I was guided by an expert of the field and I thank him for his patience to bear through all my erroneous results.

Huge Thanks to Quanxin Jiang (PhD candidate) for performing the FEM analysis that formed a significant part of this project. Huge thanks to Drs. Richard Huizenga for the XRD analysis that also forms a major part of the project. Thanks are also due to Evgenii Borisov and Dr. Vera Popovich for the EBSD analysis. Special thanks to Kaustubh Deshmukh (MSc student) and Virginia Bertolo (PhD candidate) for helping me in the final days of this project.

I dedicate this project to the pure consciousness present in the smallest of particles of the universe who is making everything possible through His cosmic dance. I am merely another actor in His play.

I dedicate my hard work to my parents and my sister, who are the foundation of my existence and are the infinite source of everything positive in my life. Their infinite sacrifices have made me the man I am now.

Chapter 1

Introduction

In this age of industrialization, alloys are forced to withstand extreme engineering environments. The design of such materials requires specific attention to alloying elements which would enable them to have superior properties. Used in jet engines one such nickel-based alloy is Inconel 718, which provides not only adequate mechanical properties but also good oxidation and creep resistance which is specifically suitable for the hot environment found in the engines. In addition to the above properties Inconel 718 provides good weldability which ensures assembly of complex components easier. With such wide-ranging properties Inconel 718 proves to be a material of technological importance.

Conventionally produced Inconel 718 has been used in a variety of applications. From cryogenic tankage in liquid fuelled rockets to formed sheet metal parts in land-based turbine engines, Inconel 718 has been an integral part in different industries. Recently with the advent of Additive Manufacturing (AM), Inconel 718 production has seen a new paradigm shift. Additive manufacturing provides higher design freedom to deal with complexity. External and internal features can be incorporated directly from the ground up which reduces the number of parts to be assembled thereby reducing downstream operations. This results in lower cost and less wastage of material. Additionally, additively manufactured Inconel 718 exhibits comparable mechanical properties as its conventionally produced counterpart. This makes additive manufacturing of Inconel 718 an important progress in the production of this versatile material.

An important property that all engineering materials should possess is the resistance to fatigue. Conventionally produced Inconel 718 promises good fatigue resistance however new research areas are left open with the application of additive manufacturing. Many works have been done to assess the mechanical properties in AM Inconel 718. However there is significantly less literature on the fatigue properties of AM Inconel 718 as compared to the that for conventionally produced Inconel. With additive manufacturing features like texture, defects and residual stresses, which are not generally encountered in conventionally produced

material, play a major role in the fatigue properties. For future applications of additive manufacturing on Inconel 718, it is necessary to understand the effect of the processing on the fatigue properties.

Further, from previous projects done at the Delft University of Technology, it has been seen that the concept of functional grading can be successfully linked with additive manufacturing to produce components with tailored properties. Functional grading has been in use in literature for some time now and has been widely applied on materials with different properties to produce layered components with smoother transition in the interface. Functionally graded metal-ceramic composites have been used to improve cohesion of the layers thereby resulting in better fracture and fatigue properties. Similarly, metal-metal composites with different properties are also known to exist. The previous projects showed that with just a tweak of parameters in the AM process, different microstructures of Inconel 718 could be obtained leading to different mechanical properties. In this project, such heterogeneous material is investigated for fatigue crack propagation property and the effect of various microstructural features such as grain size, grain orientation and residual stresses on the same are evaluated.

In the following text of the report, relevant literature is covered to further define the current goals and show its validity by linking to various properties of Inconel 718. The experimental methods, the results, the discussion and the conclusion are covered in separate chapters. The structure of the report is as follows:

1. Chapter 2 : Literature Review - Covers all the literature to be used in this project
2. Chapter 3 : Experimental Methods - Describes the experimental procedure used to realize the goals
3. Chapter 4 : Results about microstructural characterization - Verifies the different microstructural features with literature
4. Chapter 5 : Results from the Fatigue tests - Reports the results from the fatigue tests
5. Chapter 6 : Discussions - Theoretical explanation of the results from Chapter 4 and Chapter 5.
6. Chapter 7 : Conclusion and Future recommendation - Answer the current research questions and provides directions for future research.

Chapter 2

Literature Review

2-1 Inconel 718- Material and Properties

Inconel 718 (IN718) is a nickel-based superalloy with the major alloying elements being Al, Ti and Nb. IN718 developed in the 1960's at the INCO Huntington Alloys (now Special Metals Co.) by Herb Eiselstein as a result of a search of solid-solution strengthened age-hardenable alloy [1]. The search originally was for a non-age hardenable alloy for use in mainstream lines. The material required to have high strength and long-term metallurgical stability at 650-750°C best suited for aerospace applications [1]. The resulting alloy, IN718, had comparable strength as the erstwhile available alloys like René 41, Udimet 700, Inconel X-750, and Waspalloy [1]. The major advantage of IN718 over its competitors was its resistance to strain age cracking behaviour [1]. All the above alloys are hardened by the precipitate phase γ' ($\text{Ni}_3(\text{Al,Ti,Nb})$). Strain age cracking occurs in highly restrained weldments because of high local stresses in the temperature range where aging occurs. Cracks usually nucleate at the grain boundaries in the heat affected zone. The reason that the cracks nucleate at the boundaries is because of low ductility with the presence of high strains locally. While low ductility is attributed to brittle phases and localized deformation due to intergranular precipitates, high strains on the other hand occur due to residual stresses, thermal expansion and contraction, and aging contraction [2]. The latter is a result of the precipitation of γ' [1, 3]. This depletes the surrounding matrix of Al and Ti resulting in the decrease of the lattice parameter of the matrix or a net contraction [1, 2, 3]. This contraction hinders the relaxation of the high residual stress [2]. The high residual stresses along with low ductility cause cracking in the heat affected zones of the alloys [2]. Although, made of the same strengthening phases, the prime aging constituent in γ' in IN718 is Ni_3Nb [1, 3]. The Niobium based γ' has a sluggish aging response as shown in Figure 2-1[1]. This in turn leads to relaxation of the high residual stresses, which are beyond the local yield strength level. The ductility in this case is enough to allow deformation without cracking.

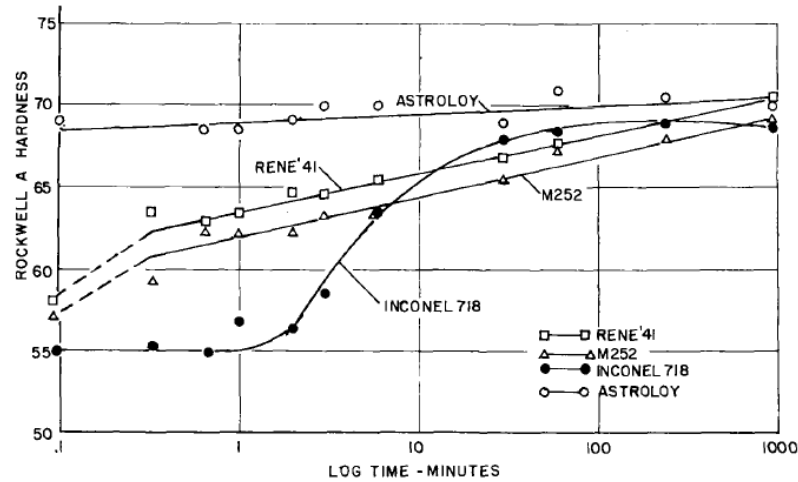


Figure 2-1: Age Hardening response of Ni superalloys [4]

2-1-1 Microstructure

The microstructure of the alloy is composed of six major phases. The gamma (γ) phase, a FCC solid solution of Ni, Cr and Fe, forms the matrix. The gamma prime (γ') and gamma double prime (γ'') are metastable strengthening phases present in the matrix that form because of aging. The delta (δ) phase is the equilibrium phase which dissolves with a solution treatment. Other phases like laves phases, carbides, and nitrides are also present in the alloy and dissolve in the matrix to some extent. These phases have different morphologies and affect the properties of the alloy differently. The phases are described in the following paragraphs.

γ phase

The γ phase (Figure 2-2) forms the matrix in the alloy. It is a solid solution of Ni, Cr and Fe in a FCC arrangement [3]. Nb, Mo, Ti and Al are also present in the solution but in minor quantities [3]. The matrix grows in form of dendrites when produced by selective laser melting [5, 6, 7, 8, 9]. During solidification the γ matrix rejects Nb, Mo and Ti into the interdendritic regions which leads to the formation of the laves phases.

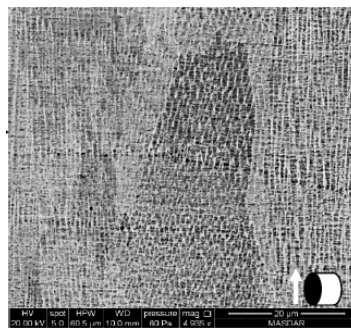


Figure 2-2: γ dendrites in different grains [8]. The arrow indicates the building direction

γ' and γ'' phase

The γ' and γ'' phase (Figure 2-3), formed as a result of aging heat treatment are the main strengthening phases in the alloy. γ' is considered to be composed as $\text{Ni}_3(\text{Al,Ti,Nb})$ whereas γ'' is considered to be composed of only Ni_3Nb with very less amounts of Al and Ti [3, 5]. γ' has a FCC L1_2 structure while γ'' phase has a DO_{22} BCT structure [5]. These phases result in the strengthening of the alloy through many different mechanisms like coherency strengthening and antiphase boundary strengthening however, γ'' is the main strength provider by precipitation hardening. The strengthening mechanisms are effective when precipitates are sheared and cut through by the dislocations. With bigger particles the hardening mechanism changes from shearing to Orowan looping [6]. The γ'' phase has a c/a ratio of 2.04 and grows in ellipsoidal/disc-shaped as well as acicular morphologies lying on $\{001\}$ planes, and c-axis is perpendicular to the disc plane corresponding to $\langle 001 \rangle$ directions [5]. The γ' phase on the other hand has a round shaped morphology. Both the phases are metastable phases and transform to equilibrium phases like δ and laves phases on heating at high temperatures for prolonged times. These phases, being metastable phases, occur only in a certain temperature range aged for a certain time. The temperature and time are determined by the Time-Temperature-Transformation curves [4].

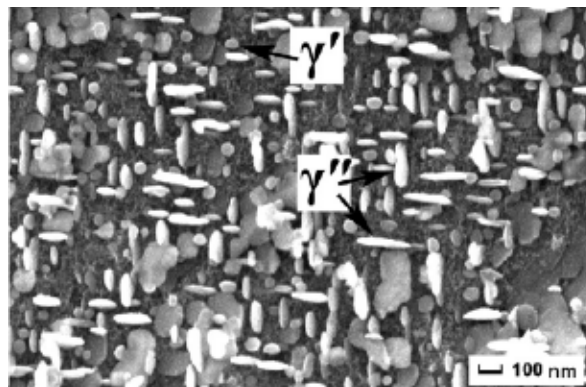


Figure 2-3: γ' and γ'' particles in AM IN718 [10]. The small scale of the micrograph is to be specially noted.

δ phase

The δ phase is the stable equilibrium version of the γ'' phase. It has the same chemical formula as γ'' but with a DO_a orthorhombic structure [5]. With lattice parameter $a = 0.514$ nm, $b = 0.423$ nm, $c = 0.453$ nm, the δ phase is present in both grain boundaries and in the interior of the matrix (Figure 2-4). The phase has both globular as well as acicular morphology [5]. The δ phase, being incoherent, provides no strength and is detrimental for the alloy in terms of strength [5]. The brittle phase cracks and leads to formation of microvoids and serves as favourable sites for crack initiation [11]. However, on grain boundaries, the phase retards grain growth and in turn improves creep resistance [11].

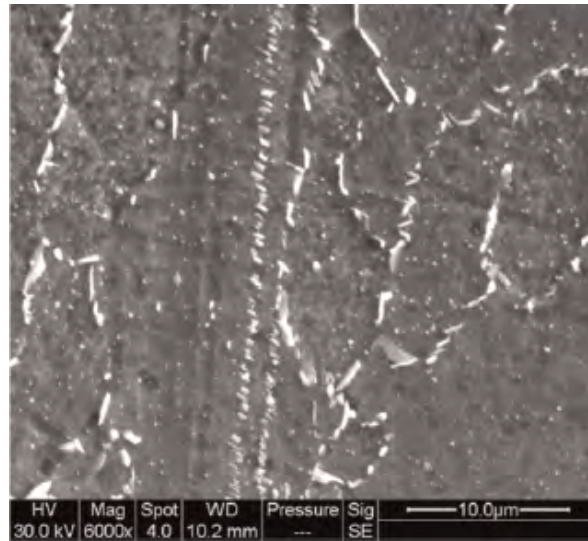


Figure 2-4: Delta phase on the grain boundaries [11].

Laves phase

The Laves phase is an intermetallic compound with the chemical formula $(\text{Fe,Ni,Cr})_2(\text{Nb,Ti})$ ([3]). It occurs in the interdendritic regions as Nb and Ti are rejected during solidification from the γ dendrites [3]. The Laves phase appears as islands (Figure 2-5) and contains about 25%Nb. The formation of Laves phase is enhanced by the presence of Mo and Si [3]. Since the Laves phase is brittle and depletes the matrix of Nb needed for γ' and γ'' precipitation, it is detrimental for the alloy's mechanical properties [3].

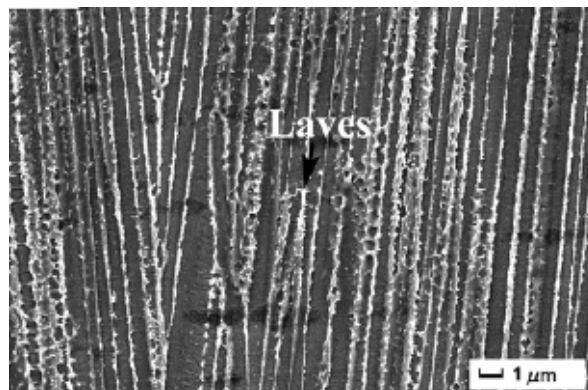


Figure 2-5: Laves phase in the interdendritic spaces [10].

Carbides

Carbides and nitrides like Nb(Ta)C, TiC, M_6C , and TiN are also present in minor quantities in the alloy [3]. The most common type among the carbides is the MC type with NbC being in major amounts [12](Figure 2-6). They are found in the interdendritic regions due

to segregation of the metal atoms while solidification [3]. These phases are brittle and their presence in the grain boundaries lead to the formation of cracks along the grain boundaries [12].

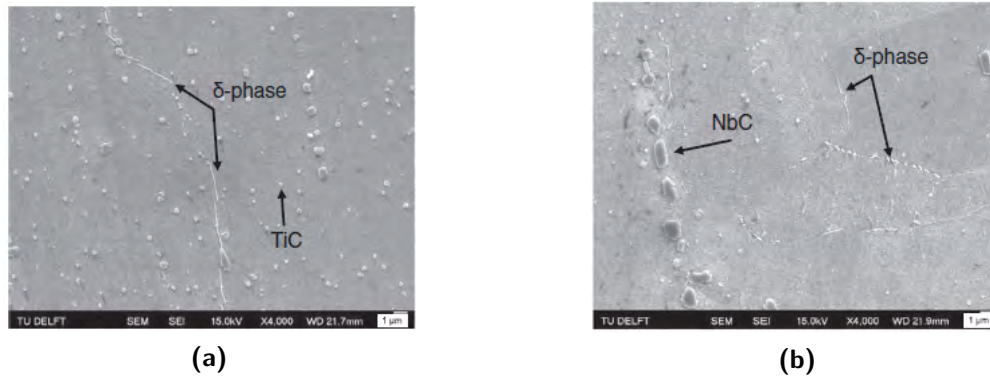


Figure 2-6: Different carbides in matrix. Delta phase is also seen at the grain boundaries as before [13].

2-1-2 Engineering Properties

IN718 is used in a variety of applications examples of which are fasteners, instrumentation parts, liquid fuelled rockets, rings, casings and various formed sheet metal parts for aircraft and land-based gas turbine engines, and cryogenic tankage parts. These applications have a wide working temperature range from -250°C for liquid fuelled rockets to 700°C in gas turbine engines. The wide range of applicability of IN718 is because of the different precipitate phases discussed above that give it good tensile, fatigue, creep strength and corrosion resistance. The same are briefly described in the following sub-sections.

Tensile Properties

Heat treated precipitate hardened IN718 has superior properties. The values for forged alloy are shown in Table 2-1. The alloy is hardened by precipitates through various strengthening mechanisms discussed earlier. Coherency strengthening, anti-phase boundary formation and precipitation hardening have been observed to be occurring in this alloy by various authors [14, 15]. Coherency strengthening occurs because of the misfit strains between the γ'' precipitates and γ matrix that impedes dislocation motion through the precipitates. Similarly, anti-phase boundary formation from the shearing of γ'' precipitates impedes dislocation motion and strengthens the alloy [5]. In addition to the shearing mechanisms mentioned above, with higher precipitate sizes Orowan looping mechanism plays an important role [6].

Table 2-1: Tensile properties of aged IN718 [16]

Property	Room Temperature	High Temperature - 650°
Tensile Strength	1375 MPa	1100 MPa
Elongation at break	25 %	18 %
Yield Strength	1100 MPa	980 MPa
Hardness	342 Hv	-

Creep Resistance

The γ'' phase plays an important role in providing strength to IN718 at high temperatures as well. Reported by Hayes in 1991 [18], γ'' are observed to impede dislocation motion at temperatures of 650°C - 760°C. The stress exponent (n) in the creep equation ($\epsilon = A.\sigma^n.e^{-\frac{Q}{RT}}$) was observed to follow a decreasing trend with temperature. This was attributed to the coarsening of the γ'' precipitates and subsequent transformation to equilibrium δ phase with temperature which reduces the precipitates' ability to impede dislocation. A high activation energy (Q) for the diffusional phenomena during creep was also observed which was attributed to the presence of Nb in the alloy. Consequently, Hayes concluded that coarsening of the γ'' particles served as a rate determining mechanism and have a stronger effect than the diffusion processes of creep [17].

Corrosion Resistance

IN718 has excellent corrosion resistance to many media. This resistance, which is similar to that of other nickel-chromium alloys, is a function of its composition. Nickel contributes to corrosion resistance in many inorganic and organic, other than strongly oxidizing, compounds throughout wide ranges of acidity and alkalinity. It also is useful in combating chloride-ion stress-corrosion cracking. Chromium imparts an ability to withstand attack by oxidizing media and sulphur compounds. Molybdenum is known to contribute to resistance to pitting in many media. [16]

Fatigue

Since its inception, IN718 has been reported to have good fatigue properties. This is covered in detail in section 2-4

2-2 Production of Inconel 718

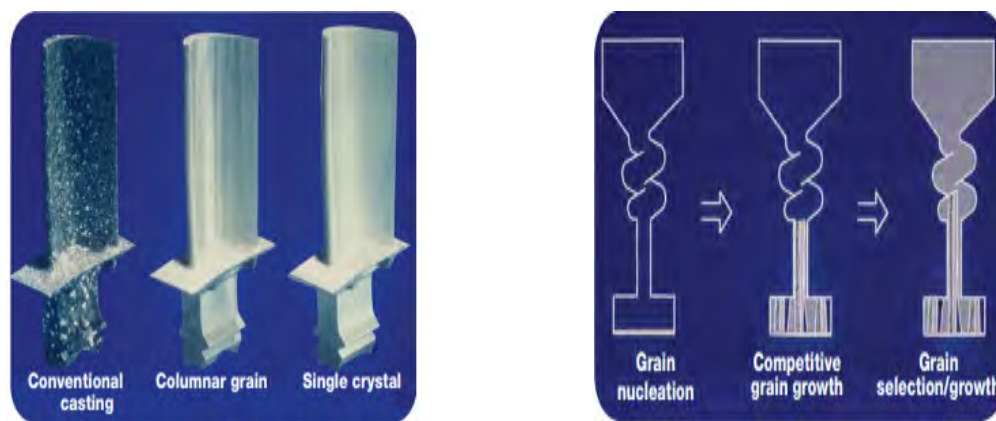
IN718 was initially introduced in wrought form [18]. Castings generally had significant interdendritic segregation of niobium and carbides to grain boundary which made structural components sensitive to cracking [19]. In addition to that, casts also were prone to chemical inhomogeneities and inclusions. Hot working after casting removed such features to some

extent and could also produce finer grain size [20]. Later with significant progress in melting techniques like vacuum induction melting (VIM), vacuum arc melting (VAR), electro-slag refining (ESR), etc and development of Hot Isostatic Pressing (HIP), cast materials was also made available [19]. The new techniques allow directional solidification of an ingot from bottom to top, yielding high density and homogeneity in its macrostructure, as well as an absence of segregation and other inhomogeneities [21]. More recently with the advent of Additive Manufacturing (AM), processing has taken another paradigm shift.

2-2-1 Conventional Methods

Conventional processing begins with the fabrication of large ingots that are subsequently used for one of three major processing routes: 1) re-melting and subsequent investment casting, 2) re-melting followed by wrought processing, or 3) re-melting to form superalloy powder that is subsequently consolidated and subjected to wrought processing operations. The initial ingots are fabricated by vacuum induction melting in a refractory crucible to consolidate elemental materials to form a base alloy [21].

Investment casting is the primary casting process for fabrication of components with complex shapes, including blades and vanes. Depending on the grain size required different approaches for solidification are employed. For example, for equiaxed grain structure a uniform solidification needs to be achieved and for single crystals the component has to be withdrawn from a hot zone to a cold zone as shown in Figure 2-7 . Shown in Figure 2-7b is the technique used to obtain a single crystal component. The whole component is solidified from the bottom up by moving it through a hot zone, as mentioned before, ensuring grain nucleation only at the bottom. Subsequently, the ‘pig tail’ feature facilitates only a single grain growth.



(a) Turbine blades manufactured with different grain morphologies.

(b) Grain selection and growth in single crystal solidification

Figure 2-7: Manufacturing of IN718 turbine blades [22]

Following initial solidification, castings are subjected to a series of subsequent heat-treatment cycles to improve the properties of the alloy [21]. An important innovation developed for cast components is to re-melt the initial cast using various methods. Cordy et al. reported

that a VIM, ESR, VAR triple melt cast had better properties due to less segregation and less inclusions [20].

Wrought processing is always preceded by a secondary remelting technique [21]. As ingot sizes increase, VIM melting often results in macro segregation or the formation of large shrinkage cavities during solidification. The formation of these solidification defects is caused by large-scale solute segregation associated with dendritic solidification under low thermal gradients. Because heat transfer during solidification of VIM ingots is limited by the low intrinsic thermal conductivity of the solidifying mass, large ingots are very prone to the formation of these features. Thus, other secondary melting processes are utilized, including VAR, ESR, and electron beam cold hearth refining (EBCHR) [21]. The alloy can then be wrought using commercial hot working operations such as rolling, forging, extrusion etc.

2-2-2 Additive Manufacturing

Additive Manufacturing (AM) or 3-D printing is the most recent innovation in the field of manufacturing techniques. AM by definition refers to a group of techniques that uses a 3-D CAD model of the object and produces 3-D objects automatically by adding material layer by layer [23, 24, 25]. Techniques like electron beam melting (EBM), selective laser melting (SLM), direct metal laser sintering (DMLS), and selective laser sintering (SLS) are the most common methods used for IN718 [24]. The above techniques are alike in the sense that they all collectively come under powder bed fusion category. Powder bed fusion refers to those techniques that involve a powder bed of the material and the component is then built layer by layer with the help of a thermal energy source. The other category is the directed energy deposition method. In this group of techniques, the thermal energy is focused on the material as it melts and forms the component [25]. The thermal source in both cases could be a laser, an electron beam or a plasma arc. IN718 produced by directed energy deposition is also reported. However, since the current project deals with alloy produced by SLM, only SLM is discussed further.

SLM technology was invented by Fraunhofer ILT in mid 1990s and is now one of the fastest growing AM technologies globally [26]. SLM involves using a high power-density laser to selectively melt powdered alloy and build the component layer by layer. SLM has proven to produce near net shape components with upto 99.9% relative density. The process starts with a CAD model of the component that is to be built. The CAD data is uploaded to the SLM machine which, with the help of a software, generates slice data for laser scanning of individual layers. A thin layer of powder is laid on a substrate situated on a platform and high-power laser is used to fuse together selected areas according to the processed data. After the laser scanning, the platform is lowered, and the process is repeated for the next layer in line. The laser keeps fusing subsequent layers and the component is built layer by layer. The process setup is shown in Figure 2-8 [27]. Once all the layers are built, loose powders are removed from the building platform and the component can be removed manually or by electro-discharge machining (EDM).

Process parameters such as scanning speed, layer thickness, laser power, scan spacing, particle size etc must be carefully controlled to produce a defect free component. These parameters can be categorized into three main categories- powder, laser, process [28]. Powder category

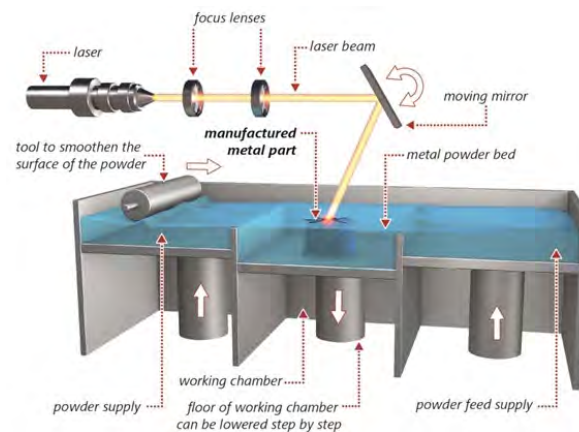


Figure 2-8: Schematic of a typical SLM setup. Adapted from [27]

involves parameters like powder size, powder flowability, size distribution and the shape of the powders. Laser category involves parameters like laser power, laser spot size, and laser mode. Finally, process category involves parameters related to the process itself like scan spacing, scan speed, scan strategy, layer thickness, building strategy, and atmospheric control.

Powder

Powder size determines the gaps between the particles. Lower the size of the particles higher the gap between them and consequently higher porosity in the final component. Size also affects flowability when small powders, instead of flowing, form agglomerates due to inter-atomic forces. On the other hand, bigger powder size leads to poor resolution and build tolerance. Hence, to optimize the process, the powder size is generally kept in the range of 20-100 μm . The distribution of powder sizes is also important. Powders of different sizes are sometimes used to fill gaps however, with a wider size distribution comes the problem of irregular melting as smaller particles melt faster than bigger particles [28].

Laser

Laser power decides the total energy put into the powder bed. This energy involves the heat needed to raise the temperature of the powder to the melting point, and the latent heat required for melting. Hence, materials with higher melting point need higher laser power. However, for a given material, laser power decides the temperature reached in the scanning spots. Beyond the melting temperature the heat increases the temperature of the melt pool that could also have implications on the microstructure of the alloy. Higher laser power for a material also means higher depth of the melt pool. Laser power along with scanning speed, layer thickness, and scan width determines the volumetric laser energy density as per Eq. (2-1) shown below. A fixed value of energy density is required to melt the alloy. Different energy density leads to different cooling rates and hence different microstructure. Additionally, laser spot size is another parameter and refers to the diameter of the laser beam on the powder bed. The spot size like the scan spacing can also affect the energy density. In Eq. (2-1), if the scan width is bigger than spot size then scan width is replaced by the spot size and vice

versa. The last parameter is the laser mode which refers to the type of beam applied. It can be a continuous beam or a pulsed beam. A pulsed beam has a peak power that is used to melt the powder suddenly. Different shapes of pulsed beam can be applied to better control the heating and cooling of the powder [28].

$$LaserEnergyDensity = \frac{LaserPower}{ScanSpacing \times ScanSpeed \times Layer} \quad (2-1)$$

Process

Scan width, scan speed, and layer thickness have been discussed already to be affecting the energy density. Scan width also called hatch width, is the distance between two neighbouring laser scans. Scan width is directly linked with production speed. Higher scan width leads to a smaller number of scans thereby reducing production time. However, it is inherent that higher scan width always requires higher laser spot size. The interplay of spot size and scan width in determining energy density was discussed already. Scan speed is the rate at which the laser beam covers the powder bed. In addition to affecting energy density and production speed, higher scan speed also leads to longer and thinner melt pool which increases the chance of forming small aggregates. Layer thickness is the thickness of the individual slices in the CAD model. In other words, it is the thickness of the powder layer that is put everytime the building platform is lowered to build a layer. Just like the above parameters, layer thickness also affects production speed in addition to energy density as specified earlier. Layer thickness has to be decided very carefully as it may also lead to ‘stairs’ on curved geometries. The remaining parameters are scanning strategy, building strategy, and the atmospheric conditions. Scanning strategy refers to the scan path taken by the laser beam. Uniformity and production speed are main aspects through which scan strategy is decided. Similarly building strategy refers to the build path decided mainly based on the component geometry. For example, building of overhangs must be planned such that a smaller number of layers and hence less time is consumed. Lastly, atmospheric conditions are controlled to prevent contamination and to prevent oxidation [28].

To summarize, the process of growth of a component being built is shown in Figure 2-9. The building direction, scanning direction and the direction of heat flow are specially mentioned.

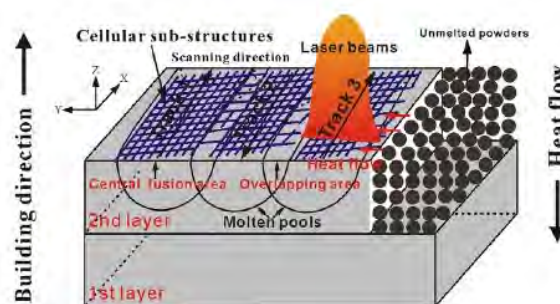


Figure 2-9: Schematic of component evolution in SLM and the different parameters [10].

2-2-3 Effect of SLM on Microstructure

Grain morphology and Phases

Microstructures of the as-processed components is shown in Figure 2-10 as reported in literature. The arched lines in Figure 2-10a shows the melt pool morphology which indicates the laser scanning path. The microstructure of such a component contains dendrites running through multiple layers in the build direction [7, 8, 9, 10, 11, 13, 29, 30, 31, 32]. This indicates an epitaxial growth of the dendrites from the substrate. As already discussed, these dendrites are the matrix phase γ and are formed due to the high cooling rate due to the heat dissipation by the cold substrate material. The highest heat gradient stays in the vertical direction and hence the dendrites are almost parallel to the building direction [9, 11, 13, 31]. The heat gradient is positive up the building direction and hence the dendrites grow up the building direction starting from the substrate. The dendrites only contain primary arms with arm spacing of 200-500 nm [9]. The yellow lines in Figure 2-10b indicate melt pool boundaries. It is clear from the figure that melt pool are not symmetrical and identical to each other. The arrows in the figure indicate growth direction of the dendrites. The direction of growth can be seen to be not perfectly aligned with the build direction. It can also be seen that the dendrites have different growth directions in a single melt pool as well. Across the melt pool boundaries, the growth either follows the same direction or is tilted 90° [9]. This is discussed further in the next sub-subsection. Laves phase decorates the inter-dendritic space due to segregation of Nb and Ti as mentioned earlier [9, 11, 13, 30, 31, 32]. Carbides and nitrides like TiC and TiN are also reported to be present at the grain boundaries along with laves [11, 13]. The size of the phases is in the range of 100-200 nm and are observed only under TEM [11, 32]. A TEM analysis also reported the presence of γ' and γ'' precipitates in trace amounts [11]. This trace amounts of these phases can be attributed to the depletion of Nb by the laves and δ phases.

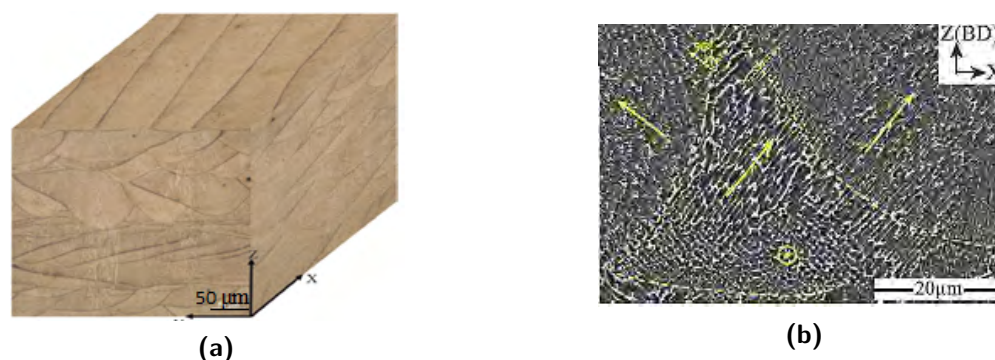


Figure 2-10: a) 3-D optical metallograph composite showing microstructures of as-fabricated sample in the building direction [11]. b) Cellular dendritic structure in as-built samples. The dashed yellow lines represent melt pool boundaries. The arrows represent the growth direction of the dendrites. [9]

Texture

The evolution of texture is attributed to epitaxial growth. It was reported that the growth of the dendrites follows the same direction or tilted by 90° across the melt boundaries [9]. This is because of the preferential growth of fcc γ phase in not just one direction but all the directions in the $\langle 100 \rangle$ family of crystallographic directions [9] as shown in Figure 2-11. If the heat flow is along the $[100]$ direction, then that forms the primary dendrites' direction. Any secondary dendrite then has a $[010]$ or $[001]$ direction. Although, the heat flow has a strong gradient in the build direction, local disturbances due to convection and scanning parameters may cause heat gradient to be aligned along other directions for another neighbouring melt pool. For this melt pool the tip of a growing secondary dendrite in the previous melt pool will form the primary dendrite. Hence, the dendrites in this melt pool will grow perpendicular to the original direction. The situation is also seen in Figure 2-10. This effect essentially establishes a relation with the heat gradient and the growth direction or texture.

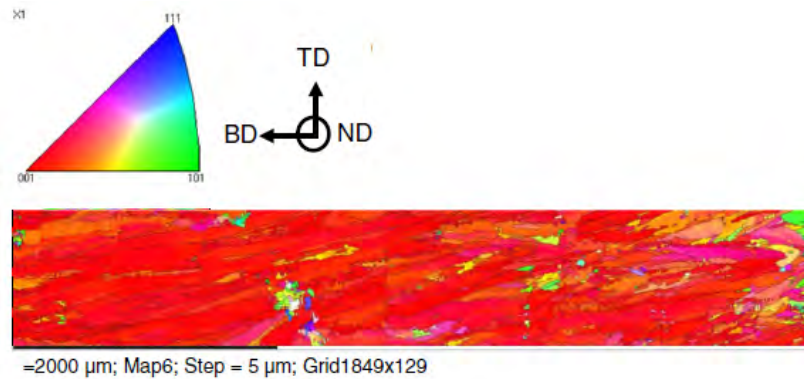


Figure 2-11: Inverse pole figure (IPF) coloured map of as-built IN718 showing texture evolution [13].

Residual stress

TEM also reported the presence of dislocation networks in the matrix as well as the intergranular regions [9, 11, 32]. This is shown in Figure 2-12 where dislocations can be seen as black lines. The dislocations are because of the large plastic strain due to the residual stress. The high temperature gradient because of the repeated heating and cooling causes this residual stress. The presence of this dislocation networks leads to recrystallization during heat treatment [11].

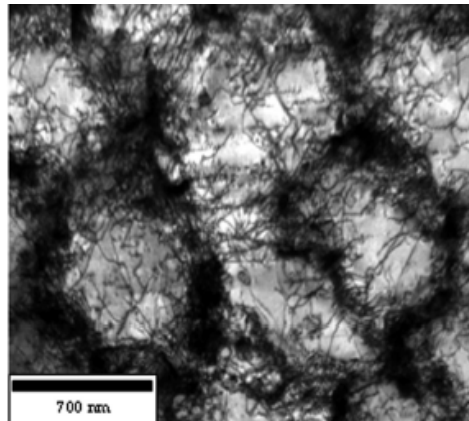


Figure 2-12: Dislocation networks observed in as-built IN718 [11]

Defects

In addition to metallurgical effects, SLM of IN718 also causes geometrical defects. These defects can be identified as two main types- spherical gas pores and lack of fusion voids [33, 34, 35, 36]. This is shown in Figure 2-13.

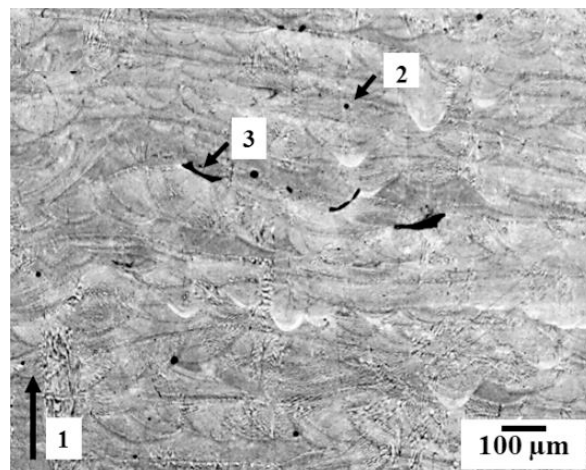


Figure 2-13: Optical Micrograph of as-built IN718 showing 1) build direction 2) Gas pores 3) Lack of fusion void [35]

Gas pores occur because of entrapped gas that formed bubbles and could not escape through the surface before solidification [33, 36]. The entrapped gas could be from the powder particles due to the atomization of powders or could be from the inert gas used during melting [33, 34, 36]. These pores are generally reported to have a spherical geometry. In addition to reducing the relative density, these pores also serve as crack initiation sites and thus have a negative impact on mechanical properties [33, 37, 38].

The second type of defects, the lack of fusion voids, occurs between two layers and arises due to un-melted powders. Powders are left un-melted due to insufficient heat input which is directly linked to the process parameters discussed earlier [33]. Hence, an erroneous balance

of parameters that may lead to insufficient heat input leads to such effects. For example, high scan speeds leaving very less time for the melt to flow or high scan width leading to insufficient mixing. In both the examples the newly solidified material fails to form a continuum with the previously solidified material and hence leads to gaps [33]. Lack of fusion can also occur due to shrinkage of the melt while cooling [35]. Neighbouring scan tracks experience contraction while cooling and form gaps between them. These voids generally have very sharp geometries and hence are more dangerous than pores as they have a higher stress concentration [35, 36].

2-2-4 Effect of SLM on Mechanical Properties

Tensile properties of IN718 manufactured by SLM are summarized in the Table 2-2. Properties of wrought and cast alloys are also tabulated. Although, the exact values of the properties vary from report to report, there exists a consistency in the trend of properties observed across different processing methods.

Table 2-2: Tensile properties of as-built IN718 as compared to cast and wrought counterparts [11].

Properties\Process	SLM (as-processed)	Wrought (h/t)	Cast (h/t)
Yield Strength (in MPa)	849	1034	758
Ultimate Tensile Strength (in MPa)	1126	1276	862
Elongation (in %)	22.8	12	5
Hardness	32.5	34	25

From the table, components manufactured by SLM are observed to be generally inferior compared to typical wrought alloys. Yield strength and ultimate strength of wrought alloys are both more than that of SLM alloys. This is because the SLM alloys are devoid of the strengthening phases as discussed earlier. The conventionally produced alloys compared here are heat treated and thus contain appropriate amounts of strengthening phases. In addition to that, as-built SLM components also contain detrimental entities like the laves phase, the carbides and defects discussed earlier. These entities, as mentioned before, serve as crack initiators and decrease the strength of the material. Fatigue strength is also affected by these entities and is covered in detail later. In a summary, as-processed SLM components can be said to not stand as good as wrought components but are clearly superior to cast counterparts in terms of tensile properties.

Directionality of properties

The most significant effect of SLM as a manufacturing process is the directional properties it gives to components. It has been widely reported that AM processes including SLM give rise to weaker components along the build direction than in the transverse direction [9, 39]. This is principally because of defects in the plane perpendicular to the build direction [29]. As discussed earlier, voids occur between consecutive layers of printed material and have very sharp geometries. In the case when the loading direction coincides with the build direction, the sharp defects being perpendicular to the loading direction serve as the weakest spots for

crack initiation and propagation. In addition to these sharp voids, spherical pores in the printed component also worsen the situation. Fatigue lives of components have been reported to be short when the cyclic stresses are applied in the build direction compared to when it is applied in any other direction [29, 40]. Fractography analyses in such component generally report crack initiation at pores and voids near the surfaces [29].

The dendritic grains also contribute to the directionality [9, 39]. The grains are oriented along the build direction hence resist deformation across the grains. This can be explained better with dislocations. Dislocations face higher number of obstacles along the perpendicular directions than along the build direction. Although, this may increase the strength in a defect free component, in a defect infused component, the accumulation of dislocations at the grain boundaries actually leads to the formation of micro-voids, hence higher number of crack initiation sites and thus lower strength.

Literature also reports that in addition to the above two factors, residual stresses also has a non-insignificant role towards the directionality [9]. SLM leads to different levels of residual stresses depending on the building strategy. Building strategy decides the heat gradient experienced at different parts of the component and thus the level of residual stresses. Higher residual stresses would mean more dislocations and thus more micro-voids. However, the local heat gradient, which decides the level of residual stress, also depends on the geometry of the component that is printed. Thicker sections of a component have higher constraints and thus higher residual stresses than thinner sections.

2-3 Post process Heat-Treatments

Heat treatment of IN718 is necessary to form the precipitate phases γ' and γ'' that strengthen the alloy. It was reported in the previous section that the mechanical properties of as built SLM component are inferior to heat treated wrought alloys, which proves that heat treatment is necessary for any manufacturing process including SLM. Hence, standard heat treatments have been defined by the Society of Automotive Engineers (SAE) that can be applied to IN718 irrespective of the manufacturing process. The standard heat treatments are described in Table 2-3.

Table 2-3: Standard Heat treatments defined by the SAE [41, 42, 43].

Standard	Treatment	Temperature	Hold Time	Cooling
AMS 5663 (For Wrought IN 718 [41])	Solution	980°C	1h	Air cooling
	Aging	720°C 620°C	8h 8h	Furnace cooling at 55°C/h to 620°C Air cooling
AMS 5383 (For cast IN718 [42])	Homogenization	1080°C	1.5h	Air cooling
	Solution	980°C	1h	Air cooling
	Aging	720°C 620°C	8h 8h	Furnace cooling at 55°C/h to 620°C Air cooling
AMS 5917 [43]	Hot Isostatic pressing	1160°C/103MPa	3h	Furnace cooling

The standard AMS 5663 is applicable for bars, rings and other forgings and thus is applicable for wrought IN718. On the other hand, the standard AMS 5383 is applicable to investment

castings and thus contains an extra step of homogenization. Castings generally have significant segregation due to which it is necessary before any further heat treatment. It is reasonable to expect that components processed with AM also have significant segregation and hence AMS 5383 is more suitable, however, both standards are used in literature. The last standard is a simple hot isostatic pressing treatment that is generally applied to injection molded IN718 and is done to densify the components.

2-3-1 Effect of AMS 5663/5383 on microstructure of SLM produced IN718

Precipitates

As mentioned before, the as-built microstructure of IN718 contains the brittle Laves phase, the δ phase and the carbide phases. These phases formed primarily because of segregation of Nb and Ti not only weaken the alloy, but also consume Nb and Ti that is needed for the precipitation of γ' and γ'' phases. Homogenization and solutioning reduces this segregation releasing Nb and Ti back into the matrix. Laves phases and the carbides are dissolved while δ phase is precipitated [9, 10, 11]. A solution treatment at 980°C, dissolves majority of the laves phases but leads to local areas rich in Nb because of the poor diffusivity of the Nb atoms [10, 11]. At these areas, δ phase precipitate consuming the Nb that could have been used by the precipitation phases [11]. However, with a prior homogenizing treatment at 1080°C, the Nb is more uniformly distributed hence making less Nb available for the precipitation of the δ (6-8% Nb) phase [11]. Another way of reasoning is that the precipitation temperature for δ phase lies between 650°C to 980°C and hence beyond 980°C, δ phase is not precipitated in the homogenization step [10, 9]. In the following solution treatment at 980°C, δ phase is then precipitated at the grain boundaries. With only a solution treatment that leads to local areas rich in Nb, acicular δ phases are found both in the interior and the grain boundary [11]. On the other hand, a solution treatment following a homogenization treatment results in needle shaped δ precipitates only at the grain boundaries [5, 6, 7, 8, 10, 11]. The grain boundaries collect the Nb from the interior during the homogenization and become preferable sites for δ precipitation in the following solution treatment. The presence of the needle shaped δ precipitates pin the grain boundaries and impede their motion while recrystallization thereby controlling the amount of grain growth during the following aging treatment [11]. Finally, with the aging treatment the main strengthening phases γ' and γ'' are formed [5, 6, 7, 8, 9, 10, 11, 41, 42].

Residual Stress

After the homogenization treatment, residual stresses are reported to be completely removed. But with only a solutioning treatment, only 80% residual stresses are removed [9, 11]. The higher temperature of homogenization is needed to achieve complete stress relief. With the removal of residual stresses, the dislocation networks shown in Figure 2-12 also disappear.

Pores

Sangid et.al. [44] with the help of tomography have reported that there is a decrease in the number of large pores after heat treatments. Although, small pores remain, most large pores

from the bulk are removed. Large pores were observed near the free surface, but the number is drastically reduced as compared to as-built specimens [44]. Small pores are not as sensitive to heat treatments as the large pores and show significantly less reduction.

Grain size and morphology

As above, there is marked difference between the grain size and morphology obtained after just solutioning and that after homogenization along with solutioning. In the former, partial recrystallization takes place and the grain sizes remain fine as obtained in the as-built condition [11]. However, in the latter, complete recrystallization takes place resulting in alternating layers of fine and coarse grain structures along the transverse direction [8, 11]. The alternating grains follows the path of the laser scan with the overlapping regions resulting in finer grains and the adjacent regions in coarse. Zhang et al. [11] reasoned this using residual stresses. The overlapping regions lead to more residual stresses offering a greater driving force for recrystallization and thus finer grain. While the grain size in the adjacent areas lead to coarse grains due to small driving force. The morphology of the grain is serrated along the grain boundary due to the needle-shaped δ precipitates [11]. The rough morphology restricts grain boundary sliding and improves creep properties of the alloy [11, 13]. The highly dendritic grain structure is lost and gain a more equiaxed morphology [8, 35].

Texture

Most grains maintain the longer length along the build direction. This also implies that the crystallographic orientation remains significantly unchanged. The elongated grains have $\langle 100 \rangle$ set of directions parallel to the build direction which is maintained after the heat treatment [8, 13]. This establishes the fact that heat treatments had enough driving force to relief stress and recrystallize the grains but not high enough to erase the texture.

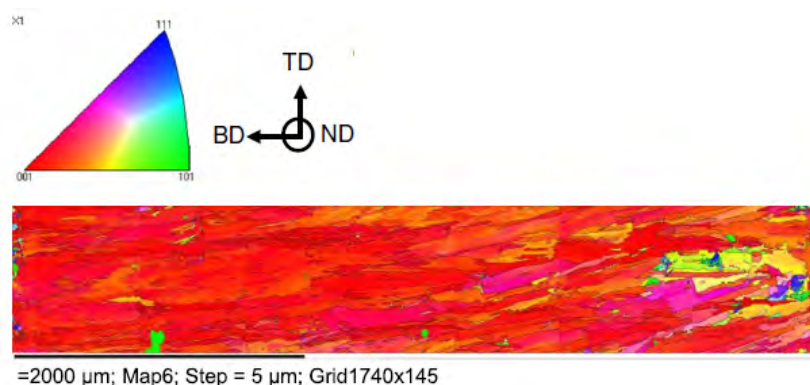


Figure 2-14: IPF showing texture in heat treated SLM IN718 [13]. Note the similarity with Figure 2-11.

2-3-2 Effect of AMS 5663/5383 on mechanical properties of SLM produced IN718

The main goal of the heat treatments for IN718 is to improve the mechanical properties by introducing strengthening phases. A significant improvement in properties can be seen in the tensile properties as described in Table 2-4.

Table 2-4: Summary of properties after different processes.[11]

Standard	Yield Strength (in MPa)	Ultimate Tensile Strength (in MPa)	Elongation (in %)	Hardness (in HRC)
As-processed	849	1126	22.8	32.5
AMS 5663	1084	1371	10.1	43
AMS 5383	1046	1371	12.3	42.5
Cast	758	862	5	25
Wrought	1034	1276	12	34

Both standards of heat treatment result in a significant increase in strength as compared to the as-built specimens. It can also be observed that the heat treatments make the alloy comparable to wrought alloy in terms of strength. This is primarily because of the appearance of the strengthening phases γ' and γ'' in the matrix [5, 9, 10, 11, 45]. These precipitates provide strength by impeding dislocation motion by different mechanisms as mentioned earlier. The piled-up dislocations after reaching a certain limit cut through the precipitates and keep moving until they encounter δ precipitates [11]. The δ precipitates are incoherent with the matrix and can't contain any plastic deformation. It is here where further piling, cracking and subsequent formation of micro-voids take place [9, 11]. The micro-voids serve as crack initiation sites and help in crack propagation. This is the reason for the decreased ductility when compared with as-built specimens. It should be noted that the standard with a homogenization treatment (AMS 5383) results in a lower yield strength and higher ductility than the standard with just a solution treatment (AMS 5663). This is because of higher content of δ precipitates in the latter [9, 11, 45]. It was reported that the δ precipitates are present both in the interior and in the grain boundaries in that heat treatment. Hence, dislocations are more restricted in such alloys and more micro-voids form. The higher yield strength then can be linked to the higher restriction of dislocations and the lower ductility then can be linked to the presence of more micro-voids that also serve as cracks. A similar reasoning can also be applied to the hardness values which follow the same trends. The ultimate tensile strength stays exactly the same for both the standards in this case. Although, exact values vary from experiments to experiments, the trend of similar tensile strength is expected to hold true.

Fractographic analyses show that the fracture in these alloys is largely transgranular ductile fracture as evidenced by the presence of dimples on the fracture surface [9, 11]. However, as some literature report, the surface is also marked by areas of brittle cleavage [9]. These areas correspond to the brittle phases like carbides and laves phases that didn't completely dissolve while the heat treatment. Since laves and carbides are expected to dissolve during the heat treatment and by a matter of chance only do small remnants of the phases remain, that not all literature report the presence of this phases in heat treated specimens.

The directionality of properties also decreases though not completely removed. With the decrease of residual stresses and pores [9], and the homogenization that lead to uniformly

distributed strengthening phases, the anisotropy is relatively less. However, the main reason for this directionality is the presence of pores and lack of fusion cracks that see almost negligible change. Pores that were reported to have decreased only refer to large pores. Several small pores still remain in the specimens. The more dangerous lack of fusion cracks were left untouched [44] during heat treatments which pose a major setback for mechanical properties. These defects are not addressed by the standard heat treatments discussed above and need to be dealt with by additional treatments discussed further.

2-3-3 Effect of AMS 5917 on microstructure of SLM produced IN718

Pores and voids

The main effect of HIP on the microstructure of SLM IN718 is the reduction of the number of pores and voids. The voids are simply closed and consolidated again under the effect of the high temperature and pressure [46].

Phases

It is reported that carbides grow after HIP on the grain boundaries [8, 13]. Lump carbides are found to grow in contrast with the dissolution of carbides after homogenization treatment. This is attributed to Ostwald ripening of the carbides during HIP that occurs at a higher temperature and in the presence of isostatic pressure [47]. Ostwald ripening is found to occur at temperatures above 1177°C [48] and with the combination of high temperature and pressure, is supported by HIP. Whereas in homogenization treatment the temperature is not high enough (1080°C) and the carbides dissolve to match the solubility limit at that temperature [48]. However, when homogenization is applied after a HIP treatment, carbides are coarsened further. Some reports suggest that Ostwald ripening of the carbides does occur during homogenization but due to small size of the precipitates is not identified [48]. In such a case, the lump carbides formed during a prior HIP just serves as a nucleation site for further growth of the precipitates during the homogenization. This is in contrast with papers that identify carbides in as-processed samples but don't identify carbides in heat treated samples [11]. Other phases like δ phase and laves phase are dissolved under the high temperature [13, 47]. The solvus temperature of both δ (980°C) and laves phase (1025°C) are well below HIP temperatures due to which dissolution of both the phases takes place.

Morphology

Grains become less columnar. Under the effect of the high temperature, partial recrystallization takes place and the grains attain a more equiaxed structure [8, 49]. The grains also lose texture with the recrystallization [13]. A further homogenization, however, doesn't change the grains much due to the carbides that impede their growth [13].

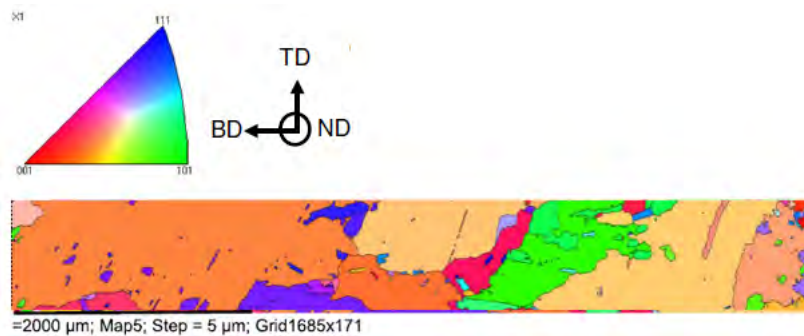


Figure 2-15: IPF showing grain orientation in HIPed SLM IN718 [13]. Note the equiaxed grains as compared to Figure 2-11 and Figure 2-14.

2-3-4 Effect of HIP on mechanical properties of SLM produced IN718

Table 2-5: Effect of HIP and heat treatment on mechanical properties [13].

Treatment	Yield Strength (MPa)	UTS (MPa)	Elongation (%)	Hardness (HV ₁)
After HIP	645	1025	38	310
After H/T	875	1153	17	360
After HIP and H/T	1145	1376	19	468

The major effect of HIP is the improvement of strength due to the reduction of pores and voids. Not only does the strength improve after the treatment, it also results in an improvement of fatigue life times. Pores serve as crack initiator during fatigue which reduces the lifetimes of the component. HIP eliminates these pores and reduces the number of crack initiation sites. Elastic modulus, elongation and hardness values have been reported to improve with just a HIP treatment. However, optimum properties are achieved only after a standard heat treatment following the HIP. Popovich et al. [13] studied the impact of heat treatments, HIP and HIP followed by heat treatment and concluded that optimum properties are achieved in the latter. The difference in properties can also be attributed to the change in microstructural features. The appearance of carbides in the grain boundaries, the dissolution of laves phases and the change of the grain morphology lead to properties as described by Table 2-5.

In a summary, the best properties are obtained after both HIP and heat treatments. Although, the ductility is lower, it is more than compensated by the increase in strength.

2-4 Fatigue properties of IN718

IN718 by the definition of its patent promises to have good fatigue strength. However, since SLM as an AM process introduces so many defects, assessing fatigue in SLM produced IN718 components is necessary from the perspective of this report.

Fatigue in additive manufactured IN718 has been recently investigated [38, 40, 50, 50, 51, 52]. The endurance strength of additive manufactured IN718 is found to be less than that of wrought counterparts [50]. This is attributed to the presence of pores and voids in the as-processed components [53]. Endurances for short-life regimes was reported to be comparable to that of wrought whereas endurances for long-life regimes was at-least an order lower [50]. In contrast to the above result, Gribbin et al. [51] reported that the endurances for long-life regimes in additive manufactured IN718 was higher than wrought counterparts and not lower. Long-life regimes which had lower strain amplitudes showed higher lifetimes for additive manufactured IN718. This was attributed to the higher strength in the as-processed IN718 components and the strength dependence of fatigue behaviour at those strain levels. On the other hand, additive manufactured IN718 had lower lifetimes for high strain amplitudes that involved plastic deformation. With the same explanation, when fatigue is controlled by plastic deformation mechanisms, components that are more ductile i.e. the wrought IN718 performed better.

Anisotropy of fatigue properties has been established in additive manufactured IN718 [29, 40]. Kirka et al. [40] reported that the texture with respect to build direction changes the failure mode in additive manufactured IN718. The presence of columnar grains in IN718 affected growth of crack. Konecna et al. [29] demonstrated that the fatigue lives of SLM produced IN718 are the least when loaded parallel to build direction. This was reasoned, as above, with the help of columnar grains that result in more grain boundaries in one direction than in other. Since grain boundaries are known to resist dislocation motion, loading along build direction where columnar grains are parallel to the load and perpendicular to the dislocation motion results in the build direction to be weak. The weakness of build direction is also related to the presence of defects and residual stresses [29].

The fatigue strength of SLM-fabricated IN718 significantly improves after the heat treatment owing to the elimination of the laves phases and the precipitation of γ''/γ' strengthening phases [30] and carbides.

In the following paragraphs, fatigue crack initiation and propagation in IN718 are discussed in detail along with the general idea of each of the events.

Fatigue involves three main events- the initiation, the propagation and the final fracture. These three events define the lifetime of a component. Hence, factors affecting each of the three events also affect the lifetime of the component. The initiation part of the life is when the weakest parts of the component, for example pores and precipitates, reach their limits of accumulating strain. Initiation leads to a situation where multiple microscopic cracks are activated from each weak point. Microscopic cracks in this case are limited to the length scale of that weak point. The multiple cracks grow to form a macroscopic crack through different mechanisms. This macroscopic crack could be of microscopic length scales but has overcome microscopic barriers in the microstructure. The propagation phase of the life refers to the growth of this macroscopic crack. After growing to a certain size, the growth becomes unstable as the crack fails to accumulate anymore strain. This leads to final event where fracture of the component takes place. The amount of lifetime spent in this final regime is minimal and

most design protocols consider full lifetime of a component before the final fracture event. From the perspective of this report only crack propagation is relevant however for theoretical completeness crack initiation is also covered in the following subsection.

2-4-1 Crack Initiation

Crack initiation in Ni alloys, including IN718 is generally attributed to brittle phases like carbides, pores, and twin boundaries. Although, pores and twin boundaries are reduced in the previously discussed heat treatments, they play a significant role in the initiation of as-built samples. AM brings with it an additional initiation site in the form of surface roughness. Due to the step wise processing protocol of SLM, surface of components contains numerous crests and troughs which could otherwise serve as small cracks. Other phases like the γ' and δ phases can also serve as initiation sites in IN718. However, except the geometrical features like the pores and the voids, the effect of all the microstructural features happens by the same mechanism. The exact definition of crack initiation is very varied in literature. From an atomistic view, a crack is initiated when the atoms overcome the local cohesive forces resulting in the creation of new surfaces [54]. Another way of defining crack initiation as some literature report is through cyclic slip irreversibilities [55, 56, 57]. It results from the slip displacements caused by the movement of dislocations in the forward part of the fatigue loading cycle that are not fully recovered in the reverse part of the fatigue loading cycle. Cyclic slip irreversibilities may have different causes and manifest themselves in different ways. Clavel and Pineau illustrated that irreversible cutting of the γ' precipitates in the nickel superalloy, Waspaloy, results in the irreversible plastic strain [58]. Other sources include persistent slip bands, pores, cross-slip of dislocations etc [56]. Ho et al. [57] showed that there exists a critical value of cumulative irreversible cyclic plastic strain to crack initiation for Waspaloy. The following paragraphs summarize the relevant sources of crack initiation for IN718 that can also be explained with accumulation of irreversible plastic strain.

Surface Roughness

AM including SLM results in components with significant surface roughness [29, 36, 37, 38]. The roughness is a direct result of the step wise processing which renders partially melted material on the periphery leading to uneven surface. The un-polished surface consists of sharp edges that can also function as notches. These process-induced notches have sharp geometries and experience high stress concentrations.

Pores

Pores and voids, as discussed earlier, are common initiation sites for both conventional and additive manufactured IN718. Pores being spherical in shape experience lesser stress concentration than voids that have very sharp geometries. Although, treatments like HIP are incorporated to reduce these defects, they are not completely removed from the bulk of the sample. HIP closes the pores and voids in the bulk but doesn't completely remove the absence of material from pores near surfaces [59]. These defects become more dangerous when they

are at or near the surface as they increase the stress intensity. Surface roughness along with these defects result in well-defined crack initiation sites from the surface [29, 37, 38].

Twin and Grain Boundaries

Strain is reported to be localized at twin and grain boundaries. Miao et al. [60] reported that for nickel base superalloy René 88 DT, crack initiation took place near a twin boundary. Dislocations pile up at these boundaries and lead to crack nucleation. However, not all boundaries lead to pile ups. Slip transfer can happen at boundaries that are less misoriented ($<20^\circ$). Dislocations piling up in this case is the source of the cyclic irreversible plastic strain discussed earlier. After attaining a certain limit of irreversible strain, a crack is initiated. Although, no such literature is published for IN718, the presence of twin boundaries in IN718 like that in René 88 DT puts IN718 under the same risk.

Precipitates

The detrimental effect of brittle phases like laves [9], δ [61] and carbides in the microstructure has already been established. Under cyclic loading, these phases crack and lead to formation of micro-voids.

Persistent Slip Bands

In the absence of all the above sites, persistent slip bands (PSBs) lead to formation of surface roughness [62]. This roughness is a result of dislocations escaping from the surface [54, 56, 63]. In other words, irreversible slip occurs near the surfaces leading to sharp edges that serve as cracks.

2-4-2 Crack Propagation

The second major phenomenon during fatigue is the propagation of the initiated crack. Propagation of cracks is generally studied with a fatigue crack growth rate (FCGR) curve shown in Figure 2-16. An FCGR curve contains three regions- the threshold region, the Paris region, the final fracture region. Crack propagation includes four main types of growth depending on the length of the crack [54]. Just after the initiation of a crack, the crack grows through the local grain along the weakest slip plane or along the direction that has the highest resolved shear stress [54]. This leads to a crack that is of the order of the grain size and is highly affected by various microstructural barrier, e.g., grain, precipitates etc [54, 65]. At this length scale the crack is a microstructurally short crack [54, 65]. Once the crack length exceeds several grain diameters or the largest barrier [65], the crack propagation is driven by the plastic zone ahead of the crack tip i.e. crack-tip opening displacement [54]. This crack is called a mechanically short crack. As the crack grows and the plastic zone size becomes negligible in size as compared to the crack, concepts of stress intensity or Linear Elastic Fracture Mechanics (LEFM) become valid [54, 65]. This crack is called a physically small crack. At this scale of crack lengths, further propagation is controlled by the stress intensity factor K . Since fatigue involves a cyclic load, the crack growth is directly linked with the change in K in each

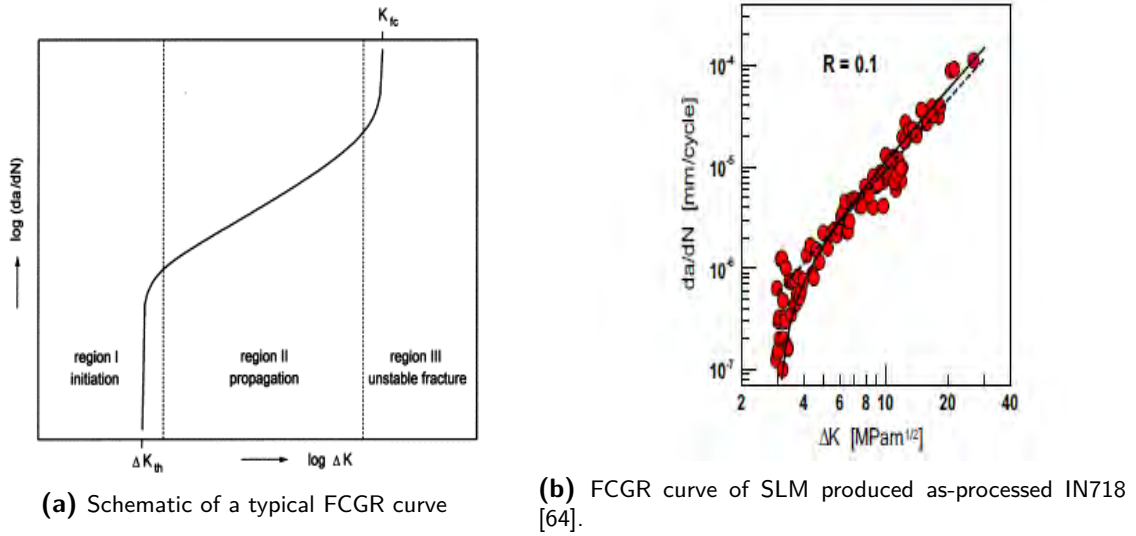


Figure 2-16: Example of FCGR curves

cycle or $\Delta K = K_{max} - K_{min}$. Further growth of this crack leads to long cracks where factors such as crack closure start affecting the effective ΔK . Crack closure essentially shields a part of the stress due to a variety of reasons like plastic deformation at the crack tip, corrosion etc [63]. However, with a higher stress ratio or $R = K_{max}/K_{min}$, crack closure is less likely to take place. The threshold region discussed earlier includes cracks when they are physically small [65]. Short cracks including both microstructurally short and mechanically short are not represented in the FCGR curve as stress intensity as a concept cannot be defined at such length scales. On the other hand, the Paris region refers to long crack growth that is not affected by local intrinsic factors and has a stable growth. The Paris region is described by the Paris law given by,

$$\frac{da}{dn} = C (\Delta K)^m \quad (2-2)$$

where C is the Paris constant, m is the Paris exponent, $\frac{da}{dn}$ is the crack growth rate and ΔK is the stress intensity range.

Short crack growth in IN718

Short crack growth is a rather limited researched topic as it contains many abnormalities. However, information such as barriers in IN718 can be tapped from literature that focus on microstructural aspects of fatigue. Yoo et al. [66] carried out strain measurements in fatigued SLM IN718 using digital image correlation (DIC) and reported that strain in heat treated is localized along certain grain boundaries. These strain localizations are oriented 45° with the loading direction which coincides with high shear strain direction. This was also related to the grain size as coarse grains in the heat-treated specimens lead to an inhomogeneous distribution of strain inside the grain. Process induced cell boundaries are also reported to serve as barriers until the gliding dislocations pile-up, rearrange themselves into PSBs and pass the boundary. PSBs are also reported to pass grain boundaries. For heat-treated

specimens, annealed twin boundaries and precipitates serve as better barrier to short crack growth than grain and cell boundaries.

Long crack growth in IN718

Long crack growth in IN718 is relatively more explored. Although, literature regarding SLM IN718 is limited, results from literature on conventional IN718 are noteworthy. Clavel and Pineau [58] report a planar slip mechanism for fatigue in IN718. The entire crack path is also reported to be transgranular [58, 64, 67, 68]. The threshold region is marked by the formation of microtwins [58] while the fracture surface is reported to be faceted [58]. Locally flat fracture surfaces were also observed by Mercer et al. [67] and Andersson et al. [68]. These locally flat or faceted surfaces are attributed to the crystallographic crack growth. Mercer et al. reported that the crystallographic fracture in favoured crystallographic directions is associated with the cleavage of atomic bonds ahead of the crack tip. In such a case plastic strain is accommodated by the shearing of brittle δ precipitates. In contrast to Clavel's report of microtwins, Mercer et al. report very little dislocation or twinning activity. As a result, only very fine striations were reported by the latter. This is in line with the findings of Andersson et al. who concluded a mix of both crystallographic and plastic blunting mechanisms for the crack growth. However, depending on the stress intensity levels one of the two mechanism dominates.

The ΔK_{th} (threshold stress intensity range) was reported to be in the range of 13-14 MPa \sqrt{m} for wrought IN718 at a stress ratio $R=0.1$ and frequency 20 Hz [58]. Konecna et al. [64] who studied as-processed SLM IN718 report both faceted and non-faceted fracture surfaces. They reported a rather low threshold value of 3 MPa \sqrt{m} as can be expected from as-built specimens. It is a general fact that the threshold value depends on a variety of factors like-microstructure, the elastic modulus, the stress ratio and the environment of testing [63]. Evidently, Konecna et al [64] tested as-built SLM IN718 which has significantly different microstructure than wrought material. Microstructural features in the SLM alloy tested, like grain size, phases, texture, etc decide the threshold of the material. Coarser grains have higher threshold and vice-versa as more damage can be accommodated in larger grains. Similarly, lower volume fraction of precipitates also leads to higher threshold.

The Paris region is marked by a transition to the plastic blunting mechanism resulting in coarse striations [64, 67, 68]. At high ΔK for a stress ratio $R=0.1$, dislocation associated features like slip bands, dislocation networks and stacking faults associated with the shearing of the γ'' precipitates are observed [58, 67]. It is interesting to note that with the increase of the stress ratio R to a value of $R=0.8$, the mechanism is again dominated by crystallographic fracture with appearance of faceted fracture surfaces [67]. The role of K_{max} at this stress ratio was considered to be of significance. As already mentioned, a mix of both mechanisms are active simultaneously in crack growth in this material. However, both are locally not additive as only one of them dominates depending on the ΔK and R values [68]. The direction of the crack growth is also dependent on the local situation in the microstructure. If the slip bands at the crack tip are away from the maximum shear stress direction (45°), slipping may occur parallel along the slip band through a redistribution of stresses or

microcracks are formed ahead of the main crack and subsequently linked together [68]. A variety of local variations have been reported by Andersson et al. [68] in the Paris region. An et al. [61] studied the effect of δ phase on the FCGR and concluded that needle like δ phases help more in propagation than granular δ phase. It was reported that the presence of a precipitate free zone around needle like δ phase accumulates more strains and thus cracks propagate easier near a δ phase. Additionally, needle shaped δ phases, being brittle, break easier when faced with crack perpendicularly.

Modelling of the crack growth for IN718 involves modelling the different crack mechanisms active in different regimes of the FCGR curve. Mercer et al. modelled the three different regimes using results obtained from their FCGR curves and fractography studies. The Paris exponent values and Paris range of ΔK are presented in Table 2-6 below. For more details, the reader is referred to [67].

Table 2-6: Paris exponent values and Paris range of ΔK for different stress ratio in forged IN718

Stress Ratio	Paris Exponent m	Paris Range (in $\text{MPa}\sqrt{m}$)
0.1	3	21-48
0.3	3.4	15-38
0.5	2.5	15-30
0.8	1.8	9-11.5

2-5 Functional Grading

The concept of functionally graded materials (FGMs) was first introduced in the 1980s by Japanese scientists for high temperature applications in space planes [69, 70, 71]. The motivation for this development was the separation of ceramic tiles from the metal fuselage at the interfaces in the space planes due to different thermal expansions. With FGMs steep changes in material properties can be minimized and distributed over a wider volume. Hence, in FGMs properties are not concentrated at the interface, for example thermal stresses at metal-ceramic interface are essentially lower with the gradation of thermal expansion as shown in Figure 2-17. Although, in general the concept of FGM is applied to materials with radical heterogeneity like metal-ceramic composites, it can also be applied to traditional monolithic materials by the help of different microstructures having varied properties as discussed later. Microstructural features like phases, texture and grain sizes can be tailored to meet certain required property like toughness, ductility etc.

2-5-1 Types of FGM

FGM can be of different type depending on the classification criterion used. One way of classification is the gradation mode which may be continuous or layered (Figure 2-18). In the former the properties are changed from one side to other in a continuous manner and in the latter the material is composed of monolithic layers that show gradation in some property [72]. Another way of classification is based on the entity that is used to produce these gradations.

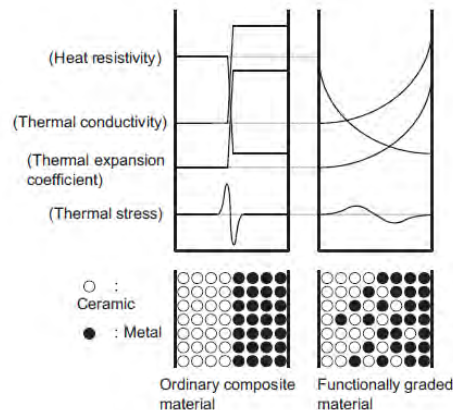


Figure 2-17: Tailored FGM composites with smooth transition in thermal properties [69].

These entities as used in literature are primarily- chemical elements, phases and pores. With a gradation in these entities variation in different properties can be achieved.

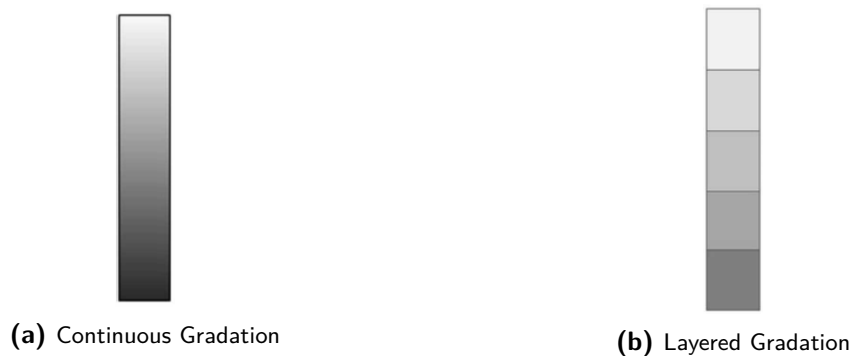


Figure 2-18: Types of FGM [72].

2-5-2 Additive Manufacturing of FGM

Conventionally, FGM specifically the metal-ceramic type has been produced by a variety of processes like vapour deposition, centrifugal casting and powder-based processes [69, 70, 73]. The introduction of AM has further enabled economic and efficient production of these materials. AM being a fairly automated process involves many parameters, the precise control of which can be used to produce FGMs with greater ease [74, 75]. Qian and Dutta [76] had paved the way for layered manufacturing of heterogenous materials through their modelling approach of the process. With further developments in the field of AM, researchers have attempted modelling and controlling the various AM processes to better their practical applicability. In the recent years, better integration of AM with FGMs has been a common attempt by various researchers [74, 75, 77]. Although, FGMs investigated by most works are of metal-ceramic composites, the concept can also be applied to heterogenous metal components with the same prospects [70, 78]. SLM, which was mentioned earlier has also seen application to produce such components very efficiently [13, 78, 79]. In a previous project

done at TU Delft, Popovich et al produced functionally graded IN718 with SLM with the help of different powers of laser [13, 78]. The different power of lasers used were 250W and 950W which yielded different zones of fine and coarse grains respectively in the same component. Additionally, in line with the effect of SLM on the microstructure of IN718 discussed in section 2-2-3, a significant texture was observed in the coarse region of the components. This resulted in significant heterogeneity in tensile properties. Young's modulus, yield strength and tensile strength were observed to be different on both sides validating the applicability of FGM concept to these components.

2-5-3 Mechanical properties of FGM

In Figure 2-17 it was shown that with FGM of the metal-ceramic type, thermal properties see a smooth transition instead of the steep change across the interface. However, since only mechanical properties are important for the current review, only the latter is discussed further. In the previous section, the project by Popovich et al [13, 78] was mentioned where the mechanical properties of FGM seem to have been affected by the gradient microstructure. This is summarized in table.

Table 2-7: Table showing different mechanical properties corresponding to different laser powers [78]

Laser Power	Young's Modulus (GPa)	Yield Strength (MPa)	Tensile Strength (MPa)
250W	173	668	1011
950W	113	531	866
Graded	155	585	880

The effect of FGM on mechanical properties have also been covered by other works [80, 81, 82, 83, 84]. The common finding was that the balance in mechanical properties is significantly improved by following the rule of mixtures. This was attributed to the strain gradient in these materials that lead to additional strengthening mechanisms. In layered gradient structures where one layer is more ductile than other, the strengthening is specially attributed to change of stress state from uni-axial stress states to bi-axial stress states [81, 82]. In continuously graded materials it is attributed to emergence of geometrically necessary dislocations leading to additional strain hardening [80, 83, 84].

2-5-4 Effect on fatigue and fracture mechanics in FGM

Gradient microstructures have been studied in literature regarding their relationship with fatigue [85, 86, 87]. Benedetti et al. [85] studied the influence of gradient microstructure in Ti alloys on the fatigue resistance. They concluded that the fatigue propagation rate in the alloy was intermediate between the two extreme microstructures used to create the gradient. Zhang et al. [86] used a surface strengthened axle steel with gradient microstructure to show fatigue crack growth. It was found that the parameters of the Paris equation and ΔK_{th} varied over the depth of the gradient microstructure. An initiated crack was found to be arrested

or decelerated while propagating on encountering a higher threshold microstructure. Ma et al. [87] investigated fatigue resistance in strength gradient steels and affirmed the idea of improving fatigue resistance by using gradient microstructure. They used graded steels and concluded that a microstructural change can significantly affect plastic deformation during fatigue propagation.

However, the above studies don't mention the effect of gradient properties on the fracture mechanics in such materials. Investigations like [88, 89, 90, 91, 92, 93, 94] have attempted to explain the fracture mechanics in these materials. To explain the fracture mechanics, these investigations basically assess the crack tip stress fields and displacement fields as compared to that in homogenous materials. Delale and Erdogan [89] were the first to make the progress in this direction. They showed that the crack tip singularity in these materials were identical to that of homogenous materials as long as the elastic modulus varies in a continuous manner. This has been confirmed by many other works [88, 89, 90, 91] and stress intensity solutions for many specific cases have been produced by finite element modelling [90, 92, 93, 94] using the above result. Although, the different results provided in the works mentioned above are interesting, with regard to the scope of this report only the theoretical formulation of the problem is discussed further. Hence, in the following paragraphs a summary of the theory regarding the crack tip stress fields and the approaches used to formulate the finite element modelling is mentioned.

Crack tip fields

Due to the geometry of the crack, the stress around a crack tip is not the same as the applied stress but instead a function of the distance from the crack. This stress distribution for homogenous materials was given by Westergaard [94] as follows,

$$\sigma(x) = \frac{\sigma_{nom}}{\sqrt{1 - (\frac{a}{x})^2}} \quad (2-3)$$

where $\sigma(x)$ is the stress at x distance from the centre of the crack, σ_{nom} is the nominal stress applied and 'a' is the half crack length. A more general solution is as follows

$$\sigma_{ij} = \frac{K_I}{\sqrt{2\pi r}} f_{ij}^I(\theta) + \frac{K_{II}}{\sqrt{2\pi r}} f_{ij}^{II}(\theta) + \dots \quad (2-4)$$

where σ_{ij} is the stress at a position of (r, θ) , K_I , K_{II} are the applied mode I and II stress intensities respectively and f_{ij} is a unique angular function valid for that mode [93]. The singularity mentioned previously comes from the above equations as at the crack-tip i.e. $x = a$ in Eq. (2-3) and $r = 0$ in Eq. (2-4), the function shoots up to infinity. It is this inverse square-root singularity that was found to be also present in FGMs. For FGMs Eq. (2-3) also includes the variation of the elastic modulus E . This was shown very simply by Ravi Chandran and Barsoum [94] using the above assumption. Since the nature of the singularity remains the same, they discretized the material in homogenous layers considering a constant E in the layers (refer to Figure 2-19). With an isostrain constraint the stress in the $i+1^{th}$ layer (Eq. (2-6)) can be correlated with the stress in i^{th} layer (Eq. (2-5)).

$$\sigma_{yy,i} = \frac{K_i}{\sqrt{\pi a} \sqrt{1 - (a/x)^2}} \quad (2-5)$$

$$\sigma_{yy,i+1} = \frac{E_{i+1}}{E_i} \frac{K_i}{\sqrt{\pi a} \sqrt{1 - (a/x)^2}} \quad (2-6)$$

Balancing the forces in all the layers to the force applied at the top specimen boundary yields the following equation for a centre-cracked tension (CCT) specimen of width $2W$.

$$\sigma_{nom} W = \frac{K_a}{\sqrt{\pi a}} \int_a^W \frac{E(x)}{E_a} \frac{1}{\sqrt{1 - (\frac{a}{x})^2}} dx \quad (2-7)$$

where K_a is the stress intensity at the crack length, E_a is the elastic modulus at the crack length and $E(x)$ is the variation of E . Depending on the function $E(x)$, K_a can be calculated in closed form solution. The derivation is made simpler with the following figure.

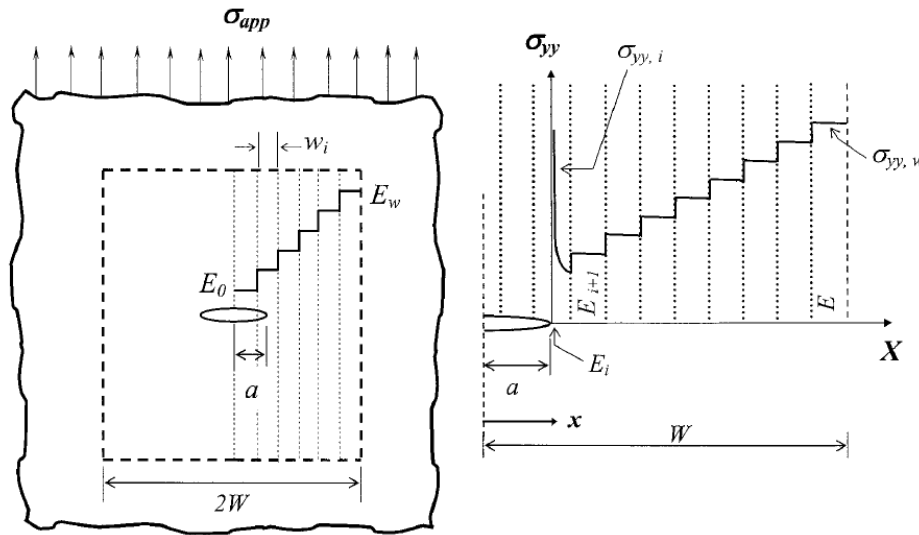


Figure 2-19: Central crack in a layered infinite plate and the schematic of the stress distribution ahead of the crack tip [97]

Ravi Chandran and Barsoum [94] presented closed form solutions for CCT specimen for different ratios of E_w/E_o (refer to Figure 2-19) and at different crack ratios a/W and verified it with a finite element model which showed an error of few %. The above analysis can be also be performed by Eqn (4) as done by Delale and Erdogan [89] which essentially implied that the parameters in the $E(x)$ are also included in the stress fields. A simple representation is as follows:

$$\text{Modulus - Variation : } E(x, y) = E_o e^{(\beta x + \gamma y)} \quad (2-8)$$

$$\text{Stress - distribution : } \sigma_{ij}(r, \theta) = e^{(r(\beta \cos \theta + \gamma \sin \theta))} \sigma_{ij} \quad (2-9)$$

$$\text{Stress - Intensity} : K_I = \lim_{x \rightarrow a} \sqrt{2(x-a)\sigma_{yy}(x,\theta)} \quad (2-10)$$

It can be noted that the parameters from $E(x,y)$, β and γ , are also present in the stress distribution $\sigma_{ij}(r,\theta)$. For brevity the derivation of the above solution is not covered here. However, the final conclusion regarding the crack tip stress fields is that the singularity remains the same with the addition of the level of inhomogeneity.

Finite Element Modelling (FEM)

As mentioned above, many works have formulated different ways for the FEM analysis of FGMs. A brief summary of the major approaches is presented here. There are three major techniques [93] by which FEM analyses in FGM can be performed:

Displacement correlation technique This is one of the simplest methods to evaluate stress intensity factors. It consists of correlating numerical results for displacement at specific locations on the crack with available analytical solutions. Like stress fields, a crack also has an associated displacement field. In this finite element method, the displacement at the elements behind the crack tip are correlated with the displacement at the crack tip. On the other hand, the displacement at the crack tip can also be obtained using the displacement field formula. On correlating the above two, the stress intensity can be expressed in terms of the displacements at the elements behind the crack tip. This is the basic idea of this method. For brevity the equations are not covered here, and the reader is referred to the following article for more information [93, 94].

Modified Crack closure integral Based on Irwin's virtual crack closure method [95] using the stresses ahead of the crack tip and the displacements behind the crack tip, the energy release rates can be obtained for mode I and II separately. The advantage of this method is that it doesn't need any assumption of isotropy or homogeneity around the crack making it more suitable for FGMs. The strain energy release rates for the mode I (G_I) and II (G_{II}), as obtained by Irwin, can be related to the work done by the stresses over the displacements produced by the introduction of a virtual crack extension. On the other hand, G_I and G_{II} can be related to stress intensity K and modulus as follows:

$$G_i = \frac{\kappa + 1}{8\mu} K_i^2 \quad (2-11)$$

where $\kappa = 3 - 4\nu$ for plain strain or $\kappa = \frac{3-\nu}{1+\nu}$ for plane stress, μ is the shear modulus and i represents the mode. This way the stress intensity at different crack lengths can be obtained using this method [93].

J* integral or domain integral As the name suggests this method uses the J integral to correlate strain energy with the stress intensity factor. For homogenous materials, the energy release rate is represented by the following line integral:

$$J = \lim_{\Gamma \rightarrow \theta} \int (W \delta_{1i} - \sigma_{ij} u_{j,1}) n_i dC \quad (2-12)$$

where W is the strain energy density and n_i is the outward normal of the path Γ , which starts from a point on the lower crack face and ends at another point on the upper crack face and u is the displacement. For non-homogenous materials J is better represented as:

$$J = \int (\sigma_{ij} u_{i,1} - W \delta_{1j}) q_{,j} dA - \int W_{,1} q dA \quad (2-13)$$

where W is a function of $E(x)$, $\nu(x)$ and $\epsilon(x)$. Hence, the derivative in the second integral $W_{,1}$, represents the effect of non-homogeneity. For the homogenous case, the second integration gives a value of zero and hence is the same as the Eq. (2-12). For brevity, further formulation is not covered, and the reader is referred to the following articles [93, 94].

2-6 Conclusions

To define the goals of the current project, it is necessary to summarize those aspects of the previous sections that form the basis for the current project. The following are the main conclusions of each section:

1. Section 1: The different phases of IN718 includes the γ phase (the matrix), γ'/γ'' phase (the strengthening phase), the detrimental laves phase, the carbides and the δ phase. The good corrosion and creep resistance are attributed to the presence of chromium and high temperature phase transformation respectively.
2. Section 2: It was shown that SLM as an AM process produces IN718 components with significant levels of residual stress, brittle phases, defects and texture. This led to anisotropy in the components. The different parameters of SLM affect the microstructure depending on the cooling rate it experiences. The resulting tensile properties were inferior as compared to their wrought counter parts.
3. Section 3: It was shown that the standard heat treatments improve the tensile properties of IN718 significantly which can be attributed to the change in its microstructure (appearance of strengthening γ'/γ'' phases, disappearance of brittle phases, decrease in residual stress). It was concluded that the best tensile properties were obtained with a combination of heat treatments and HIP which also reduced geometrical defects like voids and pores.
4. Section 4: It was shown that crack initiation in IN718 occurs at pores, twin boundaries etc. It was also shown that the threshold varies with different microstructure of IN718. Crack propagation in IN718 was predominately transgranular and is affected by the morphology of certain phases and the local situation at the crack tip. Different mechanisms of crack propagation were mentioned and depending on the local situation (phases, slip plane orientation etc) these mechanisms are dominant in the material. These mechanisms were the main deciding factor for the crack growth rate.

5. Section 5: The concept of FGM was introduced and it can be easily produced with AM. It was also shown that the concept of FGM significantly improves the balance of strength and fracture resistance. The fatigue resistance is also improved in such materials. The stress fields in these materials have the same nature as that of homogenous materials, with an addition of the level of inhomogeneity. Stress intensity solutions for such materials are calculated using special approaches in its FEM analysis.

2-7 Problem statement and research questions

In a previous project by Popovich et al [14, 81], mentioned before, graded IN718 produced by SLM using two different laser powers was assessed for their tensile properties. The component had two different microstructures with coarser grain and significant texture on one side and fine grain on the other side. The effect of laser power is in line with the main conclusions from section 2. They produced positive results with such a material improving the properties of IN718 with FGM concept. They also affirmed the effect of standard heat treatments [13] on the component which is also in coherence with the conclusions from section 3. In line with the previous project and the literature mentioned above, it can be hypothesized that there might be a significant effect on the fatigue properties. Specifically, according to the main conclusions from section 4, that show an effect of texture and grain size on the threshold and crack growth mechanisms, and section 5, that show the effect of FGM on the stress fields and the stress intensity solution, it is expected to show considerable effect on fatigue of graded IN718. Hence, the primary research objective of this study is to

“Investigate if the functionally graded microstructure can be used to affect the fatigue behaviour of Inconel 718 manufactured by selective laser melting”

In order to achieve the primary objective the following research questions are set:

1. How does the individual microstructure and mechanical properties develop during 3D-printing of Inconel 718
2. What is the effect of post process heat treatment on individual microstructure and mechanical properties
3. How does the fatigue parameters obtained for ungraded Inconel 718 depend on the various microstructural features like grain size, grain orientation, residual stresses, etc.
4. What is the difference between fatigue properties of 3D-printed and conventional wrought Inconel 718
5. Based on the results of this study and literature can the developed herein relations be used to tailor fatigue behaviour in 3D-printed functionally graded materials

Chapter 3

Materials and Methods

In this chapter, the experimental procedure is covered. In the subsequent sections, the material, the post process heat treatments and the microstructural and fatigue characterization are covered. Each section also covers further details in various subsections. A summary of all the tests performed in this project is also included in the last subsection.

3-1 Materials

Different types of specimens were utilized in this project to examine different aspects of the project. This section describes the type and other relevant details of the manufactured IN718 material. The section is divided into the following subsections-the manufacturing, heat-treatment and the final type of dimension.

3-1-1 Manufacturing

The specimens used for this project were produced by Selective Laser Melting (SLM) using gas atomized IN718 powder. Different microstructures were achieved using different parameters in the SLM process, mentioned in Table 3-1. This was based on the previous projects mentioned in the previous chapter. It was observed that the 250 W laser power lead to fine grain size and the other lead to coarse grain size. In the current project, both the individual and the gradient microstructure are produced using the same parameters which is also mentioned in the table below. Although, further details are covered in the subsequent subsections, at this point, it is sufficient to note the different grain sizes obtained for the different parameters. This will also be verified in this project.

Table 3-1: Table showing parameters used in the SLM process

Laser Power (W)	Laser Scanning speed (mm/s)	Hatch Distance (mm)	Layer thickness (μm)	Expected microstructure
250	700	0.12	50	Fine Grains
950	320	0.5	100	Coarse Grains

Additionally wrought material in the heat treated condition was also used as reference for the tests.

3-1-2 Heat Treatment

The effect of heat treatments on the microstructure and properties of SLM was covered in the previous chapter. Two standard heat treatments were discussed and it was mentioned that the best properties of SLM material are obtained with the combination of both. Hence, in this project half of the specimens underwent the combined heat treatment and were compared with SLM material in the as-processed condition. Additionally, the wrought material mentioned in the previous subsection was received in the standard heat treated condition. In the rest of the report the combined heat treatment is referred as HIP+H/T, the standard heat treatment is referred as H/T and the as-processed material is referred as AP. The above heat treatments are summarized in the table below.

Table 3-2: Table showing the Heat treatments applied

Heat Treatment	Application on	Step	Temperature	Hold Time	Cooling
H/T	Wrought Material	Solutioning	980°C	1h	furnace cooled at 55°C/h to 720°C
		Aging	720°C	8h	furnace cooled at 55°C/h to 620°C
			620°C	8h	air cooled
HIP + H/T	SLM printed material	HIP Solutioning	1180°C , 150 MPa	3h	furnace cooled
			1065°C	1h	furnace cooled at 55°C/h to 760°C
		Aging	760°C	10h	furnace cooled at 55°C/h to 650°C
650°C	8h		air cooled		

3-1-3 Type and Dimension

Five groups of specimens representing different combinations of microstructures, henceforth named as A,B,C,D,E, were used for this study. These were designed in the form of Single edge notched bending (SENB) specimens mentioned in ASTM-E399 for the fatigue tests. Out of the five groups, group A and B were designed to have the graded microstructure and were of 12×6 mm dimension. On the other hand, group C, D and E had only the individual microstructures that were used to produce the former and were of 10×5 mm. In the rest of

the report groups C, D and E are collectively called as ungraded specimens and groups A and B are collectively called the graded specimens. Of the ungraded specimens, C and D were processed with 950 W laser power and E was processed with 250 W. Since groups C and D were expected to have a coarse grain microstructure, two building directions of the SLM process are employed. The effect of building direction in SLM was covered in chapter 2 where preferential growth direction and texture were linked to the former. Hence, having two building directions adds an important aspect in the current project. In terms of the geometrical shape of the specimens, Building direction (BD) of C was along the length and that of D was along the width (refer Figure 3-1). The lines in Figure 3-1a and 3-1b represent the elongated grains expected to be found in these specimens. On the other hand, specimen E was expected to have fine grain microstructure and hence building direction was assumed to be of no significance. Lastly, the graded specimen were combinations of the ungraded microstructures. Specimen A was a combination of the ungraded specimens C and E whereas specimen B was a combination of D and E and therefore, had the same corresponding building directions (Figure 3-1d and 3-1e). In the SLM process the parameters were changed half-way to produce the graded specimens. In this way the gradient microstructure was obtained expectedly containing fine grain on one half and coarse grain on the other (Figure 3-1d and Figure 3-1e). The basis of nomenclature of all the specimens are summarized in Table 3-3.

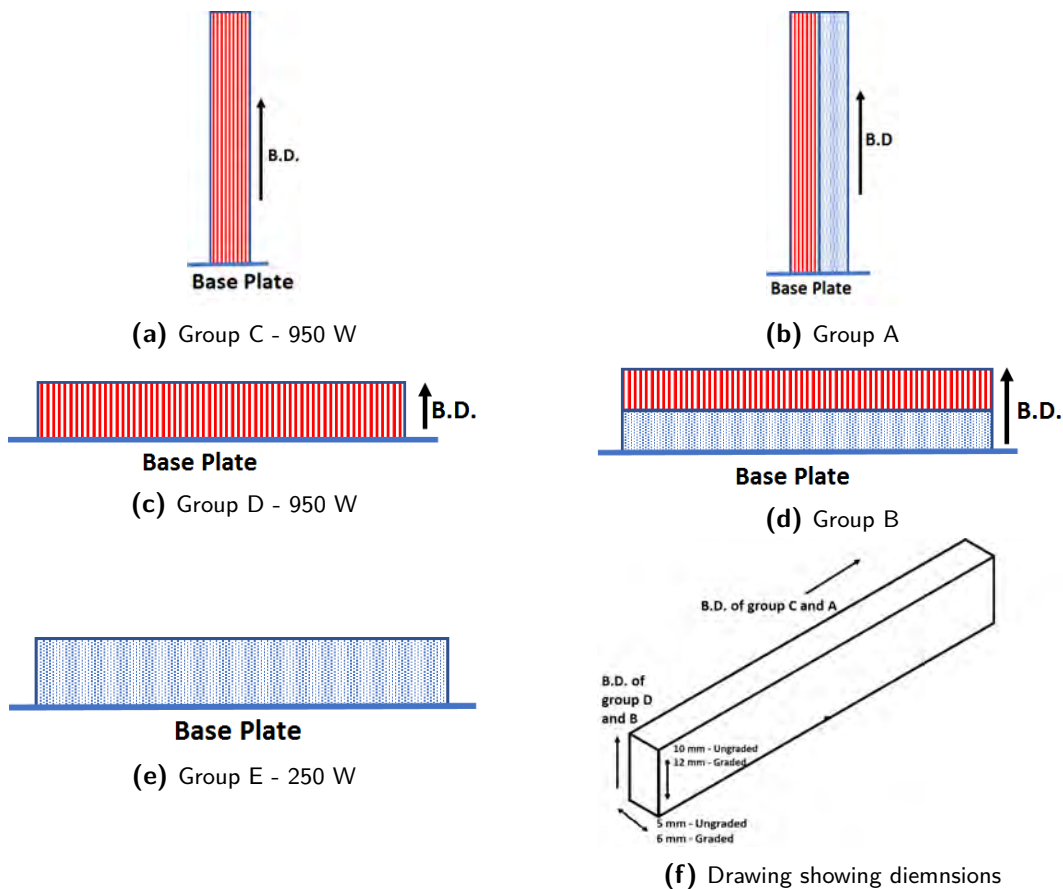


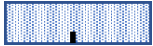




Figure 3-1: Figure showing manufacturing of the specimens and their dimensions

Table 3-3: Table showing the nomenclature of the various specimens

Type	Building direction/- Combination	SLM laser power	Dimension	Collective name	Symbolic Icon
C	Along the length	950W	10x5	Ungraded	
D	Along the width	950W	10x5	Ungraded	
E	Not applicable	250W	10x5	Ungraded	
A	C+E	Both	12x6	Graded	
B	D+E	Both	12x6	Graded	

The actual dimensions, shown in Figure 3-1f, were achieved by milling. The building directions of the specimens are shown in the figure. Notch of depth 0.5 mm and radius 0.2 mm, which is shown in Figure 3-5, was machined in all specimens with EDM. The notch in the graded specimens was machined on the fine grain side which was achieved with prior microscopy done as per procedure mentioned in the following section. Additionally, the wrought material had a dimension of 12×6 mm.

3-2 Characterization

All the SLM printed specimens were characterized using microscopy, X-ray diffraction (XRD), Electron back-scatter diffraction (EBSD) and hardness measurements. This section mentions the above topics in separate corresponding sub-sections.

3-2-1 Microscopy

The specimens were ground using sandpaper of upto 2000 grit size and then polished with 3μ , 1μ liquid. The as-processed specimens were also polished with OP-S liquid to remove fine scratches that still remained after 1μ liquid. On the other hand the HIP+H/T specimens were polished with alumina liquid instead of 1μ liquid. This was because of fine scratch like features that were observed after etching when polished with 1μ liquid. The choice of alumina was made from reports in literature that have seen a similar phenomena with Ni based alloys [96]. The scratches were reportedly made by agglomerates which became particularly visible after reaction with the etchant.

The HIP+H/T specimens were etched using waterless Kalling's agent (HNO_3 , Glycol, CuCl_2) while the AP specimens were etched with Glyceregia. The etched surfaces were then observed under both optical and electron microscopes. The primary goal of optical microscope was to observe the transition from one zone to another in the graded specimens. Both the interface and the individual zones are observed for grain features like grain boundaries, grain size and grain morphology. Further electron microscopy was used to study features related to different phases along with the above features. The optical microscope used was a Leica DMLM and the electron microscope was a Jeol JSM IT-100.

3-2-2 X-ray diffraction (XRD) analysis

XRD analysis was performed on the SLM printed specimens to identify the phases present in the specimens and to measure residual stresses. In chapter 2 it was mentioned that the materials processed with SLM have considerable levels of residual stresses which also affects fatigue. Hence, measurement of residual stresses was expected to serve as an additional information which could be related to results from the fatigue tests (discussed further). The identification of phases were done to verify their presence in the AP and HIP+H/T as per literature mentioned in chapter 2.

Both the measurements were conducted for the ungraded specimen whereas only residual stress measurements were done on the graded specimen. The stress measurements for the ungraded specimens were done at approximately the mid region along the width. The same was also repeated for the graded specimens only now the measurement was carried out on both coarse and fine grain sides. The specimens were analyzed in the polished condition. The graded specimens were also additionally etched to facilitate measurements on both the distinct sides.

The analysis was conducted on a Bruker D8 discover machine with a $\text{CoK}\alpha$ radiation of 45kV and 25mA achieving a penetration depth of 6 μm . Further details are covered in appendix B.

3-2-3 Electron back-scatter diffraction (EBSD) analysis

EBSD texture characterization were conducted on the as-processed specimens. The samples were polished using colloidal silica (0.05 μm) and the analysis was performed using SEM Mira 3 Tescan at accelerating voltage of 20 kV and a step size of 5 micron using channel 5-HKL software. A total of 14 individual maps (700 X 700 μm) were stitched together to cover the entire area of interest. The orientation maps were always presented parallel to the build direction (Z).

3-2-4 Hardness

It is known that hardness can be linked with yield strength and since the yield strength of materials generally depends on the microstructural features like grain size and phases, vicker's hardness measurements were conducted on all the different specimens. For ungraded specimens where the hardness was expected to show a constant value for a particular microstructure, 10 repeat measurements were conducted for each subgroup of specimen under each batch. On the other hand, for graded specimens multiple hardness measurements were done at intervals of 0.3 mm along the entire width direction where it was expected to vary because of the gradient microstructure. The hardness measurements were done at 1kgf with a Struers instrument, hence giving HV_1 values for the specimens.

3-3 Fatigue

The main goal of this project is to investigate fatigue properties. This section describes the different fatigue tests performed to achieve the goal of this project.

All the fatigue tests were done with three point bending configuration. Different type of tests

were conducted for the ungraded and the graded specimen. The primary goal for fatigue tests on the ungraded specimen was to establish the fatigue crack propagation behavior of the individual microstructures. On the other hand the goal of fatigue tests on the graded specimen was to check the effect of Functionally Graded Material (FGM). The results from the former were supposed to serve as a reference for the tests in the latter. However, the basic test-setup remained the same in both type of tests. Hence, this section is divided in the following subsections: Set-up, ungraded specimens and graded specimens. A summary of all the tests is also covered in the last subsections.

3-3-1 Set-up

The fatigue setup consists of the MTS machine(1), the platform(2), the rollers(3), the clamp(4), the cameras(5) and the Direct current potential drop (DCPD) equipment(6) as shown in Figure 3-2 and Figure 3-3.

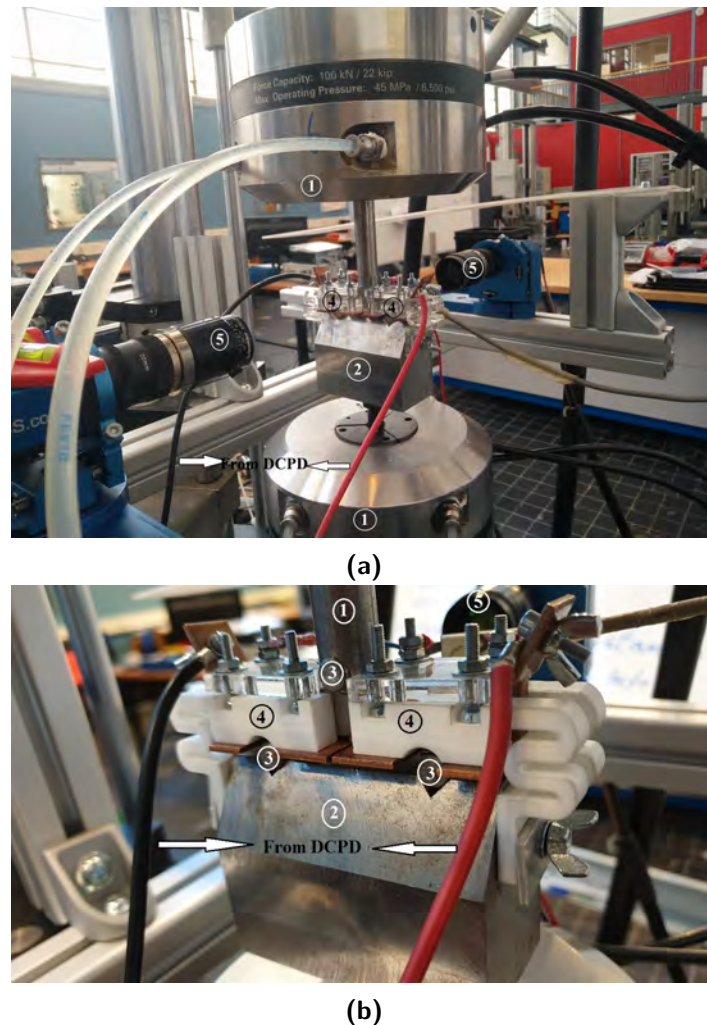


Figure 3-2: The experimental setup from the front side. The arrows show the connection with DCPD. Additionally the numbers denote the different parts.

The table-top MTS machine with a hydraulic servo was the main loading machine. The platform, as the name suggests is the main support frame for the SENB specimens and was made with S690 steel with specified slots for the rollers. The rollers, which serve as the contact points for the specimens, were as per ASTM-E399 [97] dimensions applicable for a SENB specimen of 12 mm×6 mm. The clamp was designed so as to facilitate stable connection for the DCPD probes. It also served to ensure right alignment of the specimens on the platform. Two digital cameras were arranged so as to facilitate the DIC(digital image correlation) analysis on the specimens. The DIC analysis was done with a Limes system with ISTR4 4-D software. The camera system also served as an alternate cracklength measurement technique. The primary cracklength measurement was carried out with the DCPD equipment, the probes of which were situated in the clamps at two positions-close to the crack and away from the crack. The probes of the DCPD are shown in figure. The drawing of the platform along with the rollers and the clamp is provided in appendix C. All the equipments were carefully tuned and calibrated. The MTS hydraulic system was tuned according to the stiffness of the different specimens. The voltage gain on the DCPD equipment of the two probes were chosen on a trial and error basis such that the voltage levels remain under the range of the equipment for all cracklengths. The setup and the procedure to prepare the specimen for the clamp are further mentioned in appendix C.

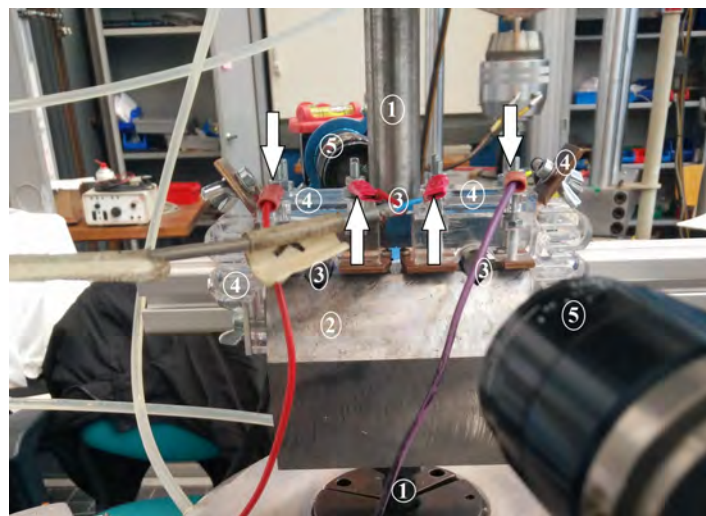


Figure 3-3: The experimental setup from the back side. The arrows denote the probes of the DCPD. In between the closer two arrows, the notch can also be seen and the probes making contact with the specimen are also seen.

3-3-2 Fatigue characterization of Ungraded specimen

As mentioned above the goal of the tests on these specimens was to investigate the fatigue crack propagation behaviour of the individual microstructures. The specimens were tested for both ΔK threshold and fatigue crack growth under constant load amplitude. One of the three ungraded specimens of type C, D and E in each batch (AP, HIP+H/T) were tested for ΔK threshold while the other two were tested under constant load amplitude tests. Given the fact that not much reliable literature is present on the fatigue crack propagation in SLM

IN718, the threshold tests were done to have an estimate of the load levels required to initiate a crack in the constant load amplitude tests.

Threshold Tests

The ΔK threshold tests were done at a frequency of 30 Hz in K control mode in the MTS machine with a constant K_{max} procedure mentioned in references [98, 99]. The value of K_{max} was chosen according to a sufficiently high ΔK and a starting stress ratio of $R=0.1$. In other words, an appropriate ΔK was chosen first such that there is high enough crack growth and then based on a starting stress ratio of $R=0.1$, the required K_{max} was calculated according to equation $K_{max} = \frac{\Delta K}{1-R}$. The K_{min} was then changed according to the equation,

$$K_{min} = K_0 \exp(C(a - a_0)) \quad (3-1)$$

where K_0 is the initial K_{min} , C is the stress intensity gradient defined as $\frac{1}{K} \frac{dK}{da}$, a_0 is the initial crack length and a is the instantaneous crack length. A value of $C = -0.4 \text{ mm}^{-1}$ was chosen for this test. At every crack extension of 0.1 mm the K_{min} is calculated according to Eq. (3-1) and manually reset. The process was carried on until the crack didn't grow by 0.1 mm in 100000 cycles achieving a crack growth rate of atmost $1 \times 10^{-6} \text{ mm/cycle}$. The final reading of ΔK was treated as the threshold value and the load values corresponding to the threshold value was noted to be used as a reference for the subsequent constant load amplitude tests.

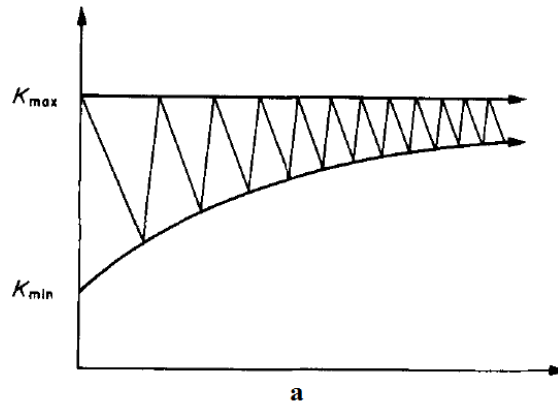


Figure 3-4: Schematic of constant Kmax procedure [98].

Fatigue crack growth rate tests

The fatigue crack growth tests were done under constant load amplitude at a frequency of 50 Hz using procedure mentioned in the standard ASTM-E647 [100]. Although, the standard doesn't recommend SENB specimens for such tests, the general guidelines mentioned in the standard were anyhow followed in these tests. The following paragraphs mention the guidelines used for the notch, the prefatigue crack and the actual crack.

Notch As mentioned before, the notch machined in these specimens was of 0.5 mm depth and 0.2 mm radius. This value of the depth was chosen from literature where SENB specimens were used for fatigue tests. The value of radius was in accordance with guideline 7.3 of ASTM-E647-15 [100].

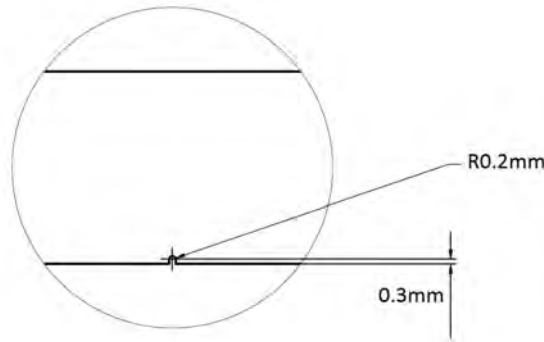


Figure 3-5: Figure showing detail diagram of the notch

Pre-fatigue crack The pre-fatigue crack necessary to overcome the effects of the notch was produced as per the standard [100]. This crack was of length 1.5 mm in these tests. The load levels obtained from threshold tests before, guided the choice of initial load level necessary for this part. As mentioned in guideline 8.3 (of the standard [100]), special care was taken to control the level of the final K_{max} in this part of the test below the actual K_{max} value. To initiate a crack, higher load levels were preferred which was then subsequently stepped down as the crack approached required length. This helped in recognizing the actual load level corresponding to near threshold stress intensity levels. The crack was monitored with the help of camera and the reference marks. These reference marks were marked at an interval of 0.5 mm starting from the edge of the notch up to a length of 7 mm in ungraded specimens and 9 mm in graded specimens as shown in Figure 3-6. Additionally, this part of the test is also used to calibrate the DCPD. Voltage and crack length data collected during the pre-fatigue is used to calculate the calibration constants of the DCPD.

It should be noted that this procedure is also followed before the threshold tests with the initiation of crack achieved by estimating sufficient load levels on a trial and error basis. In addition to the requirement of getting a sharp crack, the pre-fatigue was specially needed because the threshold tests are K controlled tests and need accurate measurement of crack lengths from the DCPD before beginning. Additionally this also helped in choosing the initial ΔK level for the threshold tests as high load levels could be used until the end of pre-fatigue crack length. From the first threshold test it was observed during the pre-fatigue that at $\Delta K = 22.5 \text{ MPa}\sqrt{m}$ these specimen showed a rapid crack growth and thus this was the chosen initial ΔK level for all the tests.

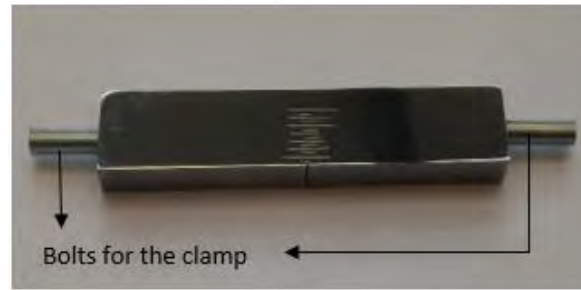


Figure 3-6: Figure showing reference marks. Bolts hammered into the specimen for the clamp can also be seen on the sides.

Actual crack In addition to the automatic acquisition of the cracklength by the DCPD, it was also manually recorded on both faces at different cracklengths using the camera and the reference marks. The crack length was also verified using optical microscope after the test and if required, necessary correction in the DCPD calibration constants were incorporated in the data.

It should be noted the above check procedure was followed in the threshold tests as well. However, since the threshold tests were in K control only at the final crack length the K value was adjusted.

3-3-3 Fatigue characterization of Graded specimen

On the other hand, the graded specimens (A and B) were tested with constant K amplitude tests to see the effect of graded microstructure on the crack growth rate. At a given ΔK level the crack growth rate should be a constant value for a particular microstructure. Hence, maintaining a constant ΔK through out the cross section of the specimen, the effect of graded microstructure was expected to be singled out. The ΔK level was chosen from the fatigue crack growth curves obtained before. A ΔK level corresponding to a crack growth rate of 10^{-5}mm/cycle at the notch side (corresponding to microstructure of E) was chosen for the specimens in a particular batch.

These tests required accurate solutions of K to calculate the load levels as the crack moved across different microstructures. But the standard solutions of K are all specially applicable to homogenous materials where the young's modulus E (not to be confused with group E) is a constant. As mentioned in chapter 2, previous works on this material have shown that E is dependent on the material and that the E of the graded material is the mean of the two homogenous materials used to produce the component (refer Table 2-7). The modulus, therefore, is expected to be a function of the position at-least in the interface of the two halves. Hence, standard solutions stand challenged in their applicability in these material. Thus, the K solution applicable for the graded materials was first simulated by using Finite Element Modelling (FEM).

This, subsequently, needed the accurate estimation of modulus E along the width of the graded specimens. Indentation measurements were taken to achieve this, however, due to

high scatter this was found to be not reliable (covered in appendix E). Alternatively, displacement recorded during the fatigue tests of the ungraded samples was utilized to calculate the E modulus. Subsequently, it was assumed that the values thus obtained are also representative of the modulus values found in the corresponding microstructure in the graded specimen. This has been covered in the following sub-subsection.

Two tests were conducted for each group of each batch. The first test was done to single out any possible effect of graded microstructure and the second test was done with DIC analysis to examine the strain evolution in the specimens. The details of these tests are also covered in the following sub-subsection.

FEM Simulation

It is expected from the information in the previous chapter that a custom K solution would be actually applicable for the graded specimens used in this project. Hence, the specimen was first modelled using finite element modelling to find the K solution. This was done using ABAQUS software where the model was formulated as per the J integral method described in the chapter. The stress intensity K was then calculated as per equation,

$$K = \sqrt{J \times E / (1 - \nu^2)} \quad (3-2)$$

where E is the Young's Modulus at the crack tip and ν is the poisson's ratio. The modulus of the specimens was calculated as mentioned above, further details of which are covered below.

Displacement method for E modulus The displacement during three point bending is related to the stiffness and cracklength as given by Tada as follows:

$$\Delta_{total} = \Delta_{crack} + \Delta_{no-crack} \quad (3-3)$$

$$\Delta_{crack} = \frac{3.P.S^2(1 - \nu^2)}{2.E.B.W^2} V_2\left(\frac{a}{W}\right) \quad (3-4)$$

$$V_2\left(\frac{a}{W}\right) = \left(\frac{\frac{a}{W}}{1 - \frac{a}{W}}\right)^2 \left\{ 5.58 - 19.57 \left(\frac{a}{W}\right) + 36.82 \left(\frac{a}{W}\right)^2 - 34.94 \left(\frac{a}{W}\right)^3 + 12.77 \left(\frac{a}{W}\right)^4 \right\} \quad (3-5)$$

$$\Delta_{no-crack} = \frac{P.S^3}{4.E.B.W^3} \quad (3-6)$$

In the set of equations above, P is the load, S is the span length, ν is the poisson's ratio, E is the modulus at the crack tip, B is the thickness of the specimens, W is the width of the specimen and a is the cracklength. The displacement recorded in the fatigue tests is basically Δ_{total} . For a given value of load P , the modulus E can then easily be calculated.

Modelling of the graded specimens The model is based on observation from previous projects that the graded specimens contain half coarse grain and half fine grain material separated by an interface of 1 mm. It was assumed that the young's modulus is a constant value on the two halves with a linearly changing modulus in the interface. Hence, the specimen

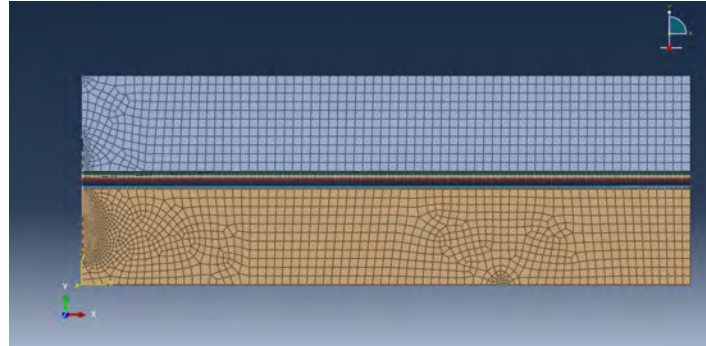


Figure 3-7: Mesh used in the FEM analysis of the graded specimen. This shows half the specimen as the mesh is symmetrical about the crack. The crack is at the left edge of the figure where mesh is shown to have more elements. The mid-width region is also seen to have several different colors representing the five layers of the interface as mentioned above.

is modelled as an elastic material made up of layers where the interface is modelled as 1 mm thick and is further divided into 5 layers of thickness of 0.2 mm to assign linearly changing Young's modulus (Figure 3-7).

The model was expected to give different K values for different crack lengths hence cracks of different lengths were also modelled by having tiny elements of 0.02 mm at the crack tip at different pre-defined positions. The analysis was then done to calculate the J integral at these positions. The J integral is calculated for a small boundary around the crack tip. It is necessary to ensure a small enough boundary for the calculation of the J integral to achieve accurate values. For this, the fifth contour or the area covered in the fifth adjacent element from the crack tip was used. This contour involved an area of approximately $0.2 \text{ mm} \times 0.1 \text{ mm}$. To check if the size of the mesh elements, the interface layers and the contour is small enough to facilitate accurate calculation, several sensitivity studies were also done on the same.

Actual Test

As mentioned above, two constant ΔK tests were conducted on each of the group (A and B) of the graded specimens. The procedure and guidelines for the notch, the pre-fatigue crack and the actual crack mentioned in the previous section were also followed here. The pre-fatigue crack in this case was of 2 mm length. The actual crack was again monitored with the help of the camera and the reference marks as before. However, the two tests conducted for each type of specimen were slightly different. The first test was conducted to primarily single out the effect of FGM material while the second test was conducted with a DIC analysis to see the strain evolution in such specimens. In this way the effect of FGM material was first investigated and then in the second test, DIC analysis was expected to give additional information about the strain evolution corresponding to any effect observed in the first test. The crack in the second test was monitored through only one face of the specimen while the other face had speckle pattern for the DIC. This speckle pattern was produced by using pressurized nozzle paint sprays to achieve fine patterns on the surface of the specimen.



Figure 3-8: Speckle pattern produced from paint sprays for DIC.






The calibration of crack length with DCPD was also carried as before. However, since the tests conducted were constant ΔK tests and the servo-hydraulic machine was operated under K control mode, the accuracy of the crack length as measured by the calibration constants was of high importance. Hence, the constants were changed every 0.25 mm during the tests to match the visual observation. The calibration constants were calculated based on the previous data points.

The DIC analysis was facilitated by the cameras and the ISTR4-4D software. The first image is recorded in the unloaded condition while the subsequent images were recorded after starting the fatigue test for every 0.5 mm crack length increments. When the crack length was mid way near the interface, the same were recorded for every 0.3 mm to facilitate recording of more images in the interface zone.

3-3-4 Summary of tests

The main goal of the above tests were to investigate fatigue crack propagation property of the graded material. Constant ΔK tests, as mentioned above, were chosen to achieve this. The measured property in these tests was the crack growth rate (da/dn) that was expected to change with gradient microstructure. For reference, the fatigue properties of the individual microstructures also needed to be established. Therefore, to achieve this, constant load amplitude tests were conducted in the ungraded specimens. Additionally, the da/dn v/s ΔK data from these tests served to provide suitable values of the latter for the tests in the graded specimen. On the other hand, for the tests in ungraded specimen the load levels needed to initiate a crack was unable in literature. Therefore, threshold tests (constant K_{max} tests) were also conducted to provide an estimate for the load levels. These tests were conducted for both the batches-AP (as-processed) and HIP+H/T as it was expected that the heat treatment would improve the property of the former. Additionally, H/T wrought material was also tested with constant load amplitude tests to serve as reference for the results of the ungraded and graded specimens. This is further summarized in the table below. For further brevity, the reader is referred to the chart shown in appendix A.

Table 3-4: Table summarizing all the tests performed for each batch in this project

Specimen group	Icon	Microstructure Type	Test	Total number of tests	Goal of the test
A		Graded-(B.D. along length)	Constant ΔK	2 (1 with DIC)	To check the effect of the graded microstructure in specimen A. DIC was used to examine strain accumulation
B		Graded-(B.D. along width)	Constant ΔK	2 (1 with DIC)	To check the effect of the graded microstructure on specimen B. DIC was used to examine strain accumulation
C		Coarse-Grain	Threshold test	1	To find the load levels corresponding to the threshold level in specimen type C
		B.D. along length	Constant ΔP	2	To establish fatigue crack growth curves for specimen type C.
D		Coarse-Grain	Threshold test	1	To find the load levels corresponding to the threshold level in specimen type D
		B.D. along width	Constant ΔP	2	To establish fatigue crack growth curves for specimen type D.
E		Fine-Grain	Threshold test	1	To find the load levels corresponding to the threshold level in specimen type E
			Constant ΔP	2	To establish fatigue crack growth curves for specimen type E.
Wrought			Constant ΔP	3	To establish fatigue crack growth curves for wrought material to serve as reference for above results.

Results- Microstructural Characterization

4-1 Microscopy

Both optical and electron microscopy were done on the specimens to verify with literature. Below are the micrographs from the SLM printed samples. The observations from the micrographs are divided into three subsections namely-coarse grain region, interface region and the fine grain region. Subsequently each subsection is further divided into sub-subsections of AP and HIP+H/T covering observations from the corresponding batches of specimens.

4-1-1 Coarse Grain region

In the following text, the main microstructural observations of the coarse grain side of the graded specimens are described.

AP-As Processed

In Figure 4-1 and Figure 4-2 showing the optical micrograph of AP-A and AP-B specimen the primary aspect that can be observed is the 'u' shaped features visible throughout the micrographs represent the melt pools formed as a result of the SLM processing. The melt pools are observed to be larger in size (with enlarged black regions) in specimen AP-B (Figure 4-2a) than in AP-A (Figure 4-1a). The melt pools can be found to be containing γ dendrites in the form of sharp features ranging across several melt pools. This is how this side of the specimen was predicted to be the coarse grain side. This is even more distinctly visible in the SEM images (Figure 4-3 and Figure 4-4). Dendrites with secondary arms are visible at higher magnification throughout the micrograph. These dendrites show a growth primarily along the building direction. However, in coherence with subsection 2-2-3 of chapter 2, secondary growth perpendicular to the primary direction can also be observed in the micrographs. In

addition to the above features, the above chapter also mentioned the presence of pores and voids in materials produced with SLM. This is not observed in this part of the specimens. Further, phases like carbides or laves phase are also not observed in these specimens which is attributed to their small size which stays unresolved under the small magnification of the microscopy used here. As mentioned in the next section, these phases are indeed present and are detected by the XRD analysis.

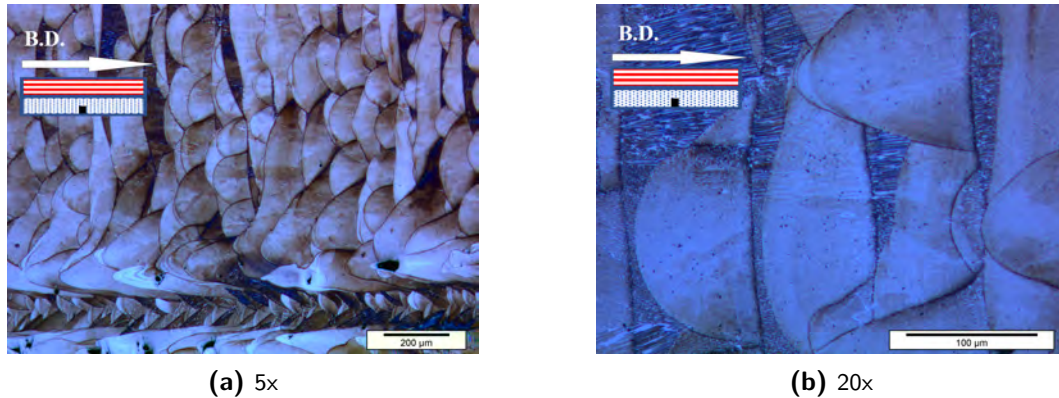


Figure 4-1: Coarse grain in AP-A specimens.

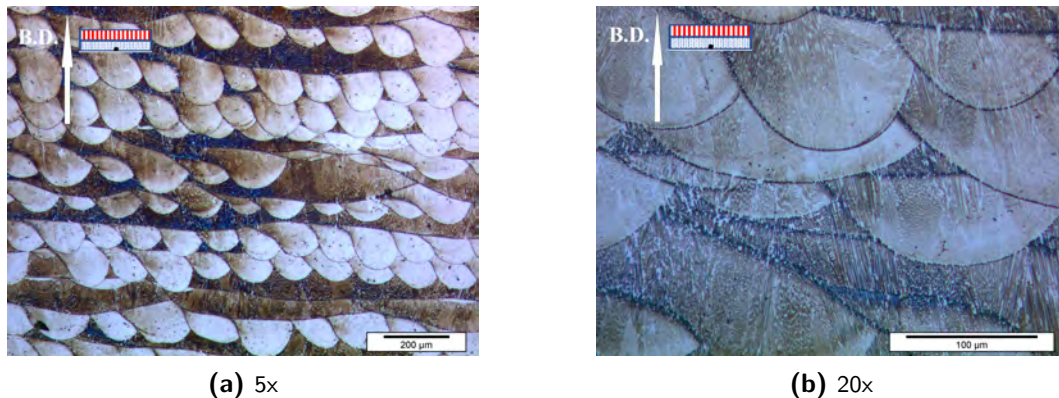


Figure 4-2: Coarse grain in AP-B specimens.

Corresponding results from ungraded samples The coarse grain of the graded specimen AP-A corresponds to the microstructure of ungraded specimen AP-C whereas the microstructure of coarse grain of graded specimen AP-B corresponds to the microstructure of ungraded specimen AP-D. Shown in Figure 4-5 and Figure 4-6 are the electron micrographs from the corresponding ungraded specimens. It can be observed that the microstructure from the ungraded specimens is largely similar as observed before. Features like melt pools and dendrites can be observed from the SEM images in the same corresponding orientations as before (Figure 4-5 and Figure 4-6). Additionally, the microstructure of AP-C, Figure 4-5, is observed to have many small pores whereas no such features are observed in the AP-D specimens. As mentioned above pores are expected to be present in this material. In previous projects, coarse grain microstructure produced with the same process parameters

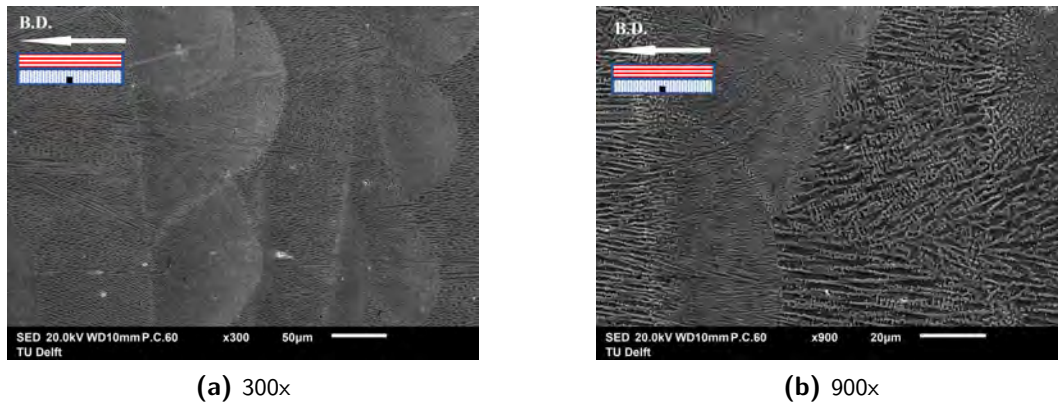


Figure 4-3: Electron micrograph of coarse grain in AP-A specimens. The dendrites can be seen spanning multiple melt-pools.

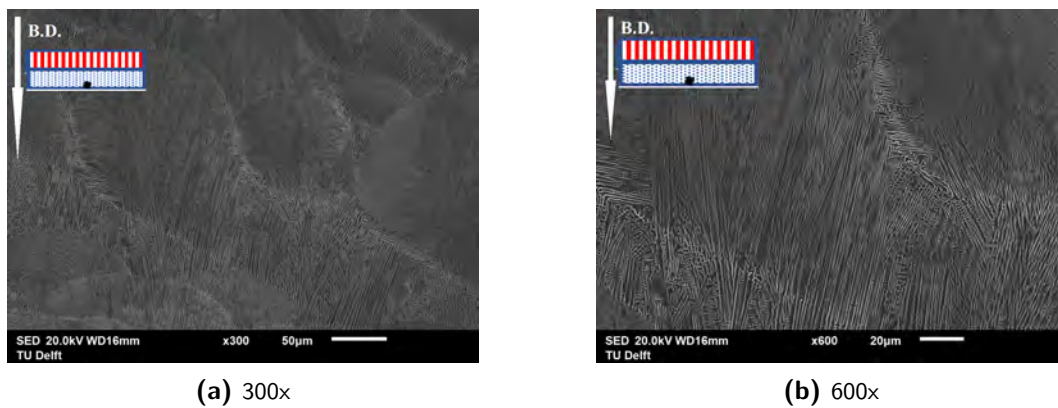


Figure 4-4: Electron micrograph of coarse grain in AP-B specimens. The dendrites can be seen spanning multiple melt-pools.

were reported to have considerable porosity (0.27%). However, it is interesting to note that AP-D specimens that had the same processing parameters with a different building direction doesn't contain visible pores. Hence, there seems to be an effect of building direction which is discussed in the next chapter. Further the absence of pores in the corresponding material in the AP-A specimens also suggests that there is also an effect of the processing of graded specimens that reduces the pores in the same. This is also discussed in the next chapter.

HIP+H/T

In the coarse grains of HIP+H/T specimens shown in Figure 4-7, melt-pools previously observed in the AP specimens are completely erased off. The grains are also observed to contain sharp morphologies due to the extensive twinning (refer Figure 4-8). The twins are also observed separately as sharp needle like features occurring inside grains. This could be attributed to the HIP treatment that involves high pressure leading to twinning at the grain boundaries. The effect of HIP also leads to closing of small pores and voids hence these entities are expectedly absent. Further, the dendrites observed before in the AP specimens have also disappeared as it is replaced by coarse grains. The grains can also be seen to be columnar

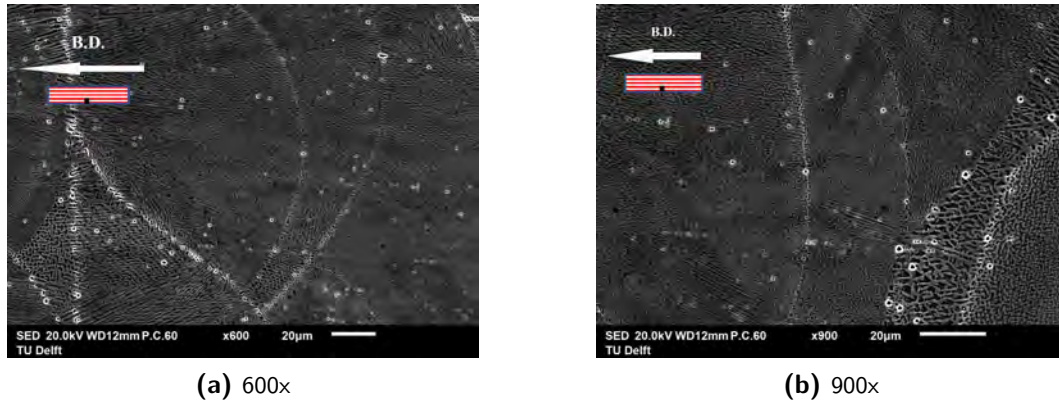


Figure 4-5: Electron micrograph of ungraded specimen AP-C.

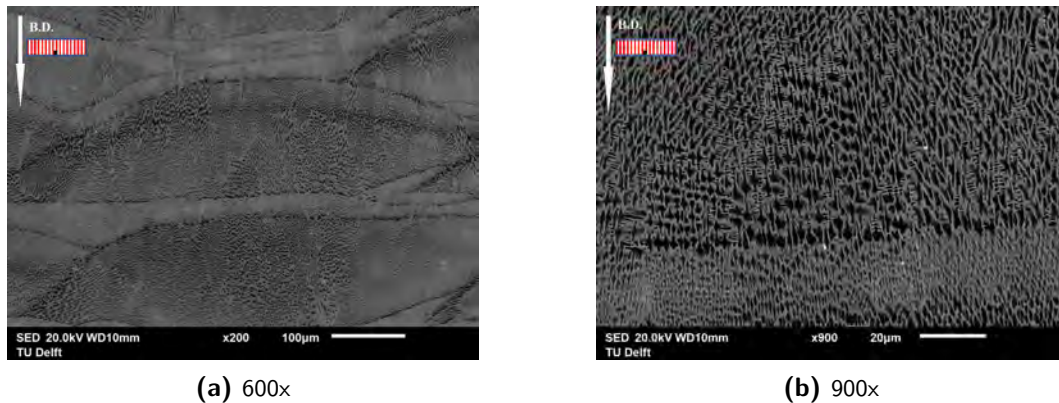


Figure 4-6: Electron micrograph of ungraded specimen AP-D.

in one direction in both the type of graded specimens. The longer direction is generally also the building direction suggesting that the preferential direction of growth observed in the AP specimens is maintained here. Anyhow smaller equiaxed grains can also be observed in both the specimens. This is in line with literature covered in chapter 2 section 2-3-3 where the microstructure of HIP+H/T was mentioned to undergo recrystallization leading to new grains. Another important observation in both the HIP+H/T specimens, A and B, are the white particles seen in fig. distinctly decorating the grain boundaries. EDS analysis on this particle showed peaks on particularly Nb and C suggesting that these carbides are NbC. This is in coherence with the observations found in literature specifically in the predecessor project by Popovich et. al where the same carbides were found in this material.

In summary, the expected effect of HIP+H/T mentioned in the literature is also replicated as per the current results.

Corresponding results from ungraded samples Shown in Figure 4-10 and Figure 4-11 are the micrographs of HIP+H/T-C and HIP+H/T-D specimens corresponding to the coarse grain microstructure of group A and B specimens respectively. The main observations from the graded specimens were carbides, twins and the columnar grains. As observed from the

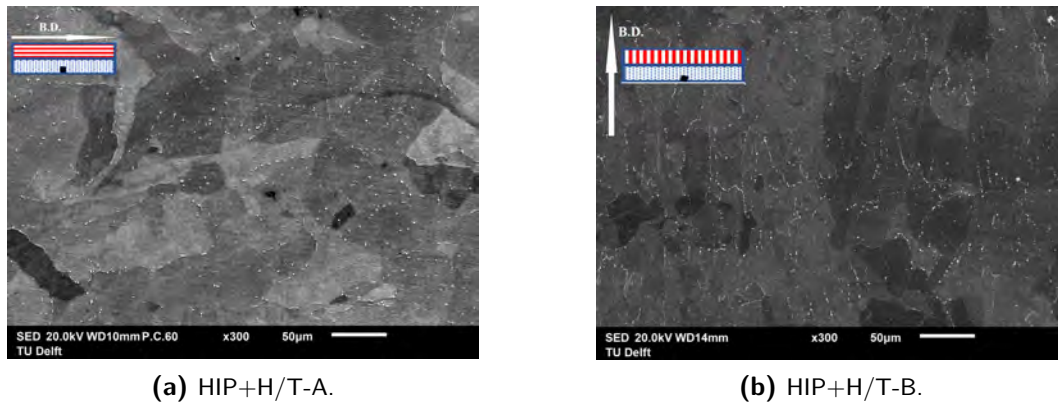


Figure 4-7: Electron micrograph of HIP+H/T graded specimens showing columnar shaped grains in both the specimens.

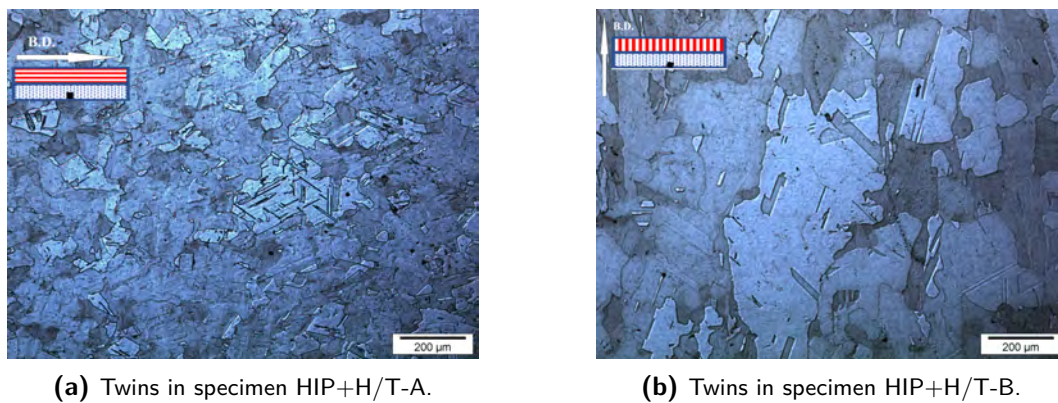


Figure 4-8: Optical micrograph of HIP+H/T graded specimen showing twins.

figures the same features are also present in these specimens. However, the amount of carbides is observed to be significantly less than that observed in the graded specimens.

4-1-2 Interface region

The interface region, as observed before in previous projects, is a small transition region formed because of the change of the processing parameters in the production of the graded specimens. The following observations are made for the current specimens.

AP-As Processed

The interface region is marked by the presence of pores at the interface region characteristic of Additive Manufacturing (AM) (Figure 4-12 and Figure 4-13). The pores are found to be of approximately as high as 50 μm in diameter. The melt-pools in the interface can be seen to undergo a change in their appearance in both the graded specimens. The interface in specimen AP-A (Figure 4-12 and Figure 4-13) is observed to have a distinct pattern making this region clearly distinguishable. On the other hand the interface in specimen AP-B is

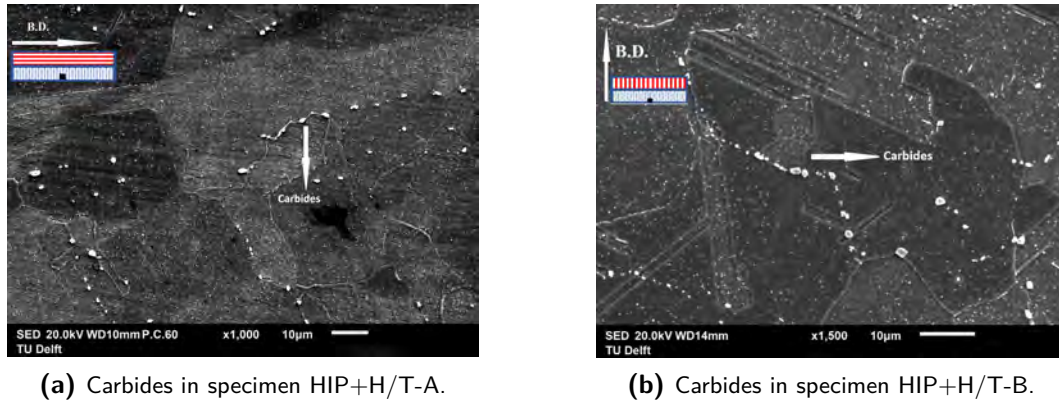


Figure 4-9: Electron micrograph of graded specimen HIP+H/T specimens showing carbides in the grain boundaries.

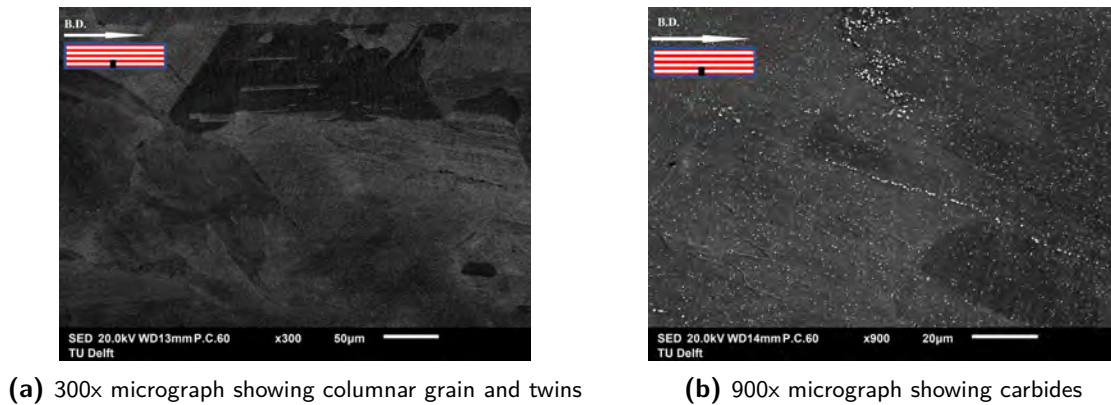
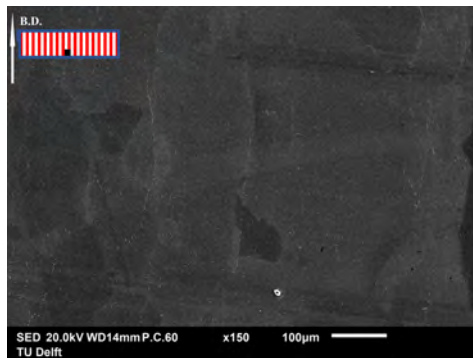


Figure 4-10: Electron micrograph of ungraded specimen HIP+H/T-C.

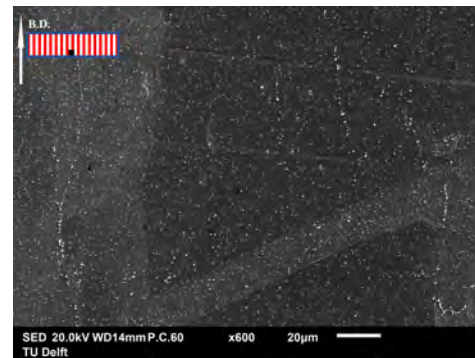
distinguished by the change in the sizes of the melt-pools. The side with enlarged melt-pools was inferred as belonging to the coarse grain side and vice versa. The high laser power used to produce the coarse grain microstructure is inferred to have resulted in enlarged melt-pools.

HIP+H/T

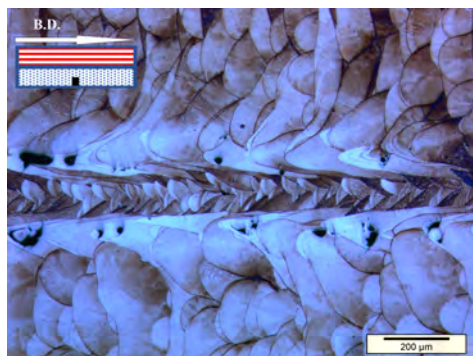
In the HIP+H/T specimens no special features is observed near the mid-width region where the interface is expected to be present. It is interesting to note that the interface was distinctly visible when observed with naked eye but was hard to distinguish in a microscope. However, since a difference between the two sides is still observed and the interface is assumed to have been faded because of the heat treatments. However, pores that were observed in the AP specimens in the interface are not found in this region. This is interpreted, as mentioned in literature, as the effect of the HIP in the heat treatment.



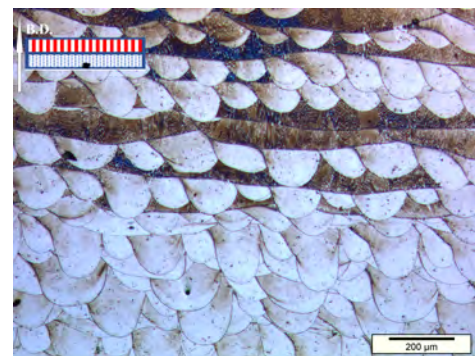
(a) 300x micrograph showing columnar grain



(b) 900x micrograph showing carbides and twins

Figure 4-11: Electron micrograph of ungraded specimen HIP+H/T-D.

(a) Melt pools in AP-A specimen.



(b) Melt pools in AP-B specimen.

Figure 4-12: Optical micrograph of graded specimen AP showing transition of melt pools across the interface.

4-1-3 Fine Grain region

AP-As processed

The fine grain side in the AP specimens is marked by melt-pools as before. The dendrites in this region are confined to only a single or atmost the adjacent meltpool unlike the coarse grain side where the dendrites spanned multiple melt-pools.

Corresponding results from ungraded samples The fine grain side of AP-A and AP-B corresponds to the microstructure of AP-E (Figure 4-16). As before no significant difference was observed in these specimens. Although, the grains are expected to be smaller than that in the graded specimens due to the effect of the reheating procedure during the processing of the specimens in the latter, this is not clearly visible here. Further since phases are not reported in the current microscopic resolution any difference of phases is not verified here.

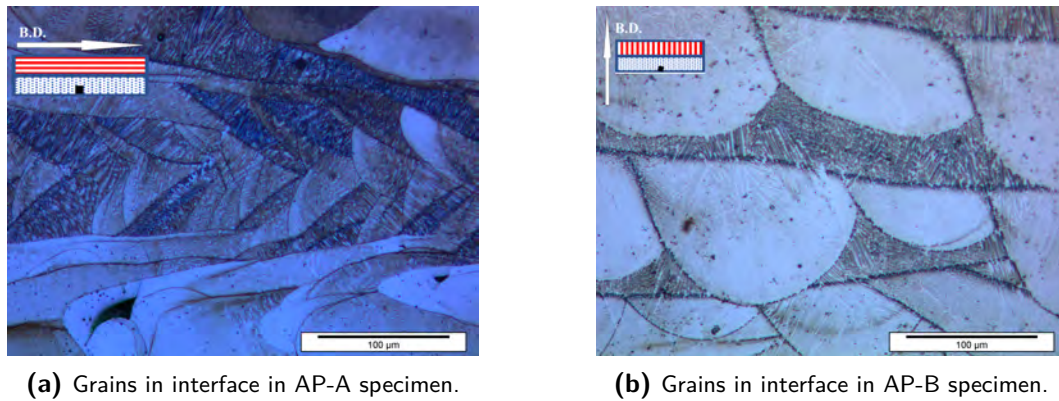


Figure 4-13: Optical micrograph of graded specimen AP showing grain evolution in the interface.

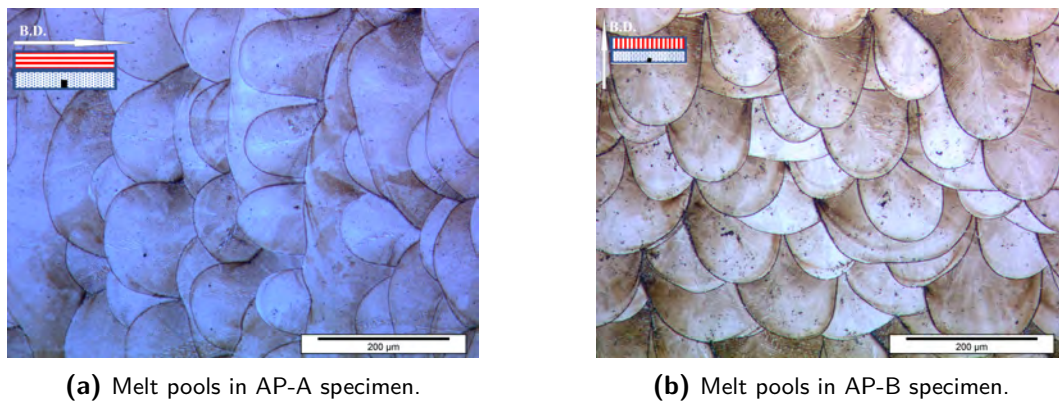


Figure 4-14: Optical micrograph of AP graded specimen showing melt-pools in the fine grain side.

HIP+H/T

The fine grain side of HIP+H/T specimens are marked by the same features as in the coarse grain side. As before the melt pools and dendrites observed in the AP specimens have disappeared and the microstructure is marked with mostly equiaxed grains (refer Figure 4-17 and Figure 4-18). Although, columnar grains are also sighted. The extent of equi-axed nature of the grains found in these specimens as compared to AP specimens is found to be high. The grains were still elongated in the building direction in the AP specimens whereas in the HIP+H/T specimens the grains are majorly equi-axed suggesting the effect of grain growth due to the heat treatment.

As before carbides and twins (refer Figure 4-19b and Figure 4-20b) are also observed in the fine grain side of the specimens. However, carbides observed in the grain boundaries is found to be less in quantity as compared to the coarse grain side in particular in the HIP+H/T-A specimen. This is not the case in HIP+H/T-B specimen where carbides on both the sides are sighted in similar quantities. This could be attributed to the different processing directions in group A and B specimen leading to difference in carbides evolution. It is interesting to note that no such difference is observed in the coarse grain side. Further it is also observed that the grains are similar in size in group A specimens where as it is clearly different in

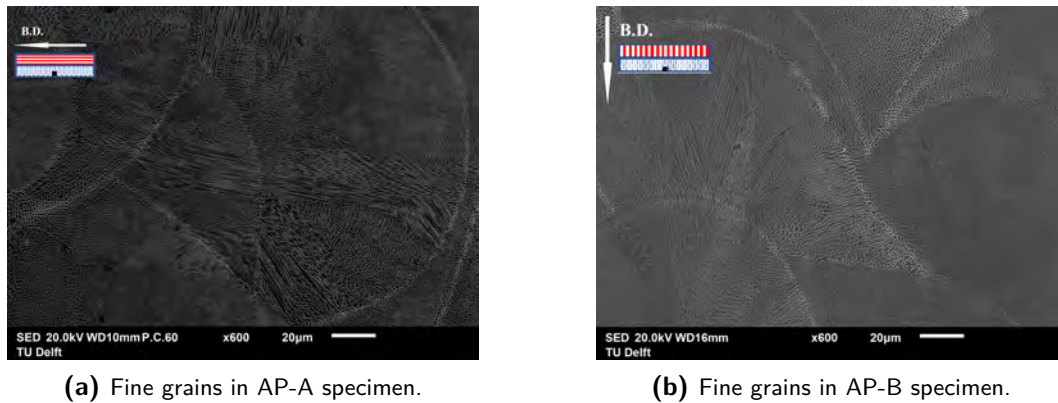


Figure 4-15: Electron micrograph of AP graded specimen showing fine grains. Dendrites can be seen only in a single melt-pool as compared to Figure 4-3 and Figure 4-4

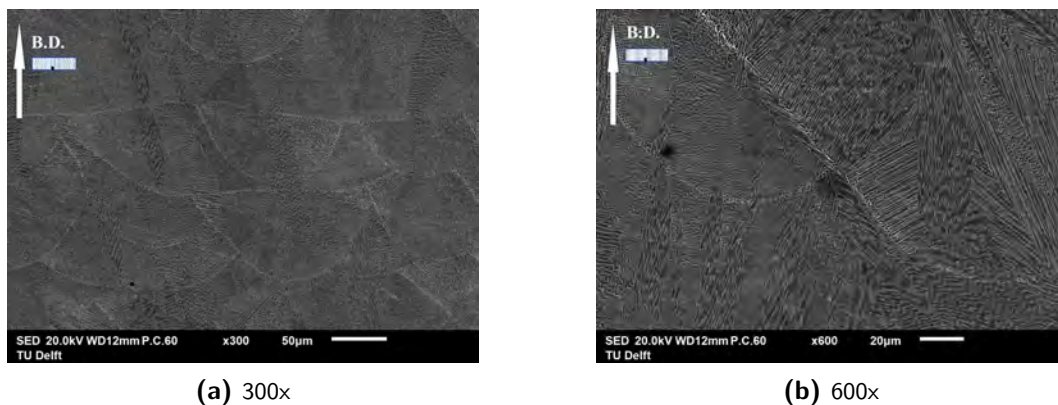
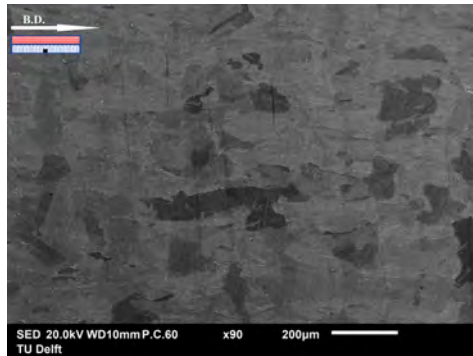


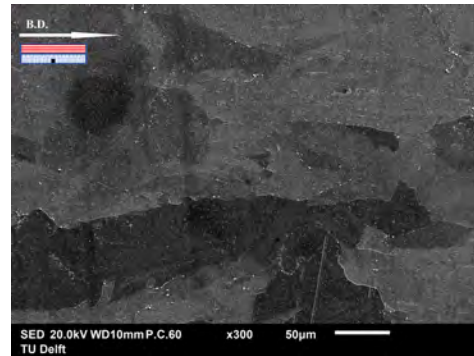
Figure 4-16: Electron micrograph of graded specimen AP-E. Dendrites can be observed to be in a single melt-pool as seen in Figure 4-5 and Figure 4-6

group B. This is observed by comparing Figure 4-8a and Figure 4-17a. Since the grains are similar in size the distinction between the coarse and fine grain side was made on the basis of sightings of columnar grains. The side with higher appearance of columnar grain was noted as the coarse grain side. This is not observed in group B specimen where the two sides had clearly different grain sizes (Figure 4-20). The above observation is attributed to the different processing orientation. The effect of building direction has also been observed previously in AP ungraded specimens where pores were observed in one orientation and not seen in the other. In this case the effect of building direction is interpreted to be resulting in higher reheating and therefore, more re-crystallization.

Corresponding results from ungraded samples Shown in Figure 4-21 is the fine grain microstructure of ungraded specimen HIP+H/T-E which corresponds to the fine grain side of the HIP+H/T graded specimens. Both equi-axed and columnar grains are observed in this specimen as before. In Figure 4-21b twins can also be observed but carbides are not seen in this specimen as before in HIP+H/T specimens. The grain boundaries were previously observed to be decorated by carbides but in this specimen they are observed to be empty. This could be attributed to the different laser power that led to the difference with the coarse

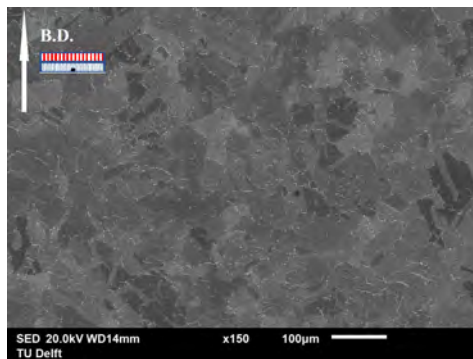


(a) Equi-axed fine grains in HIP+H/T-A specimen

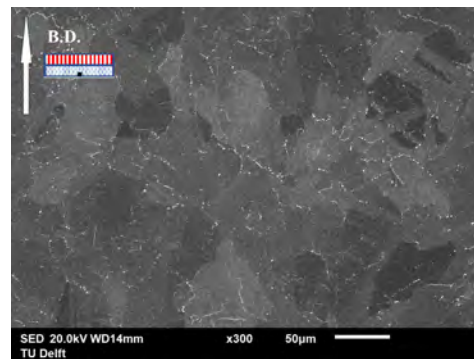


(b) Columnar fine grains in HIP+H/T-A specimen

Figure 4-17: Electron micrograph of graded specimen HIP+H/T-A showing both equiaxed and columnar grains.



(a) Equi-axed fine grains in HIP+H/T-B specimen



(b) Columnar fine grains in HIP+H/T-B specimen

Figure 4-18: Electron micrograph of graded specimen HIP+H/T-B showing both equiaxed and columnar grains.

grain microstructure. This is covered further in the next chapter.

4-2 Hardness

Vicker's Hardness measurements were taken in both ungraded and graded specimens. Thus the section is divided into two parts namely ungraded and graded specimens.

4-2-1 Ungraded Specimen

The results from ungraded specimens are summarized in the table below.

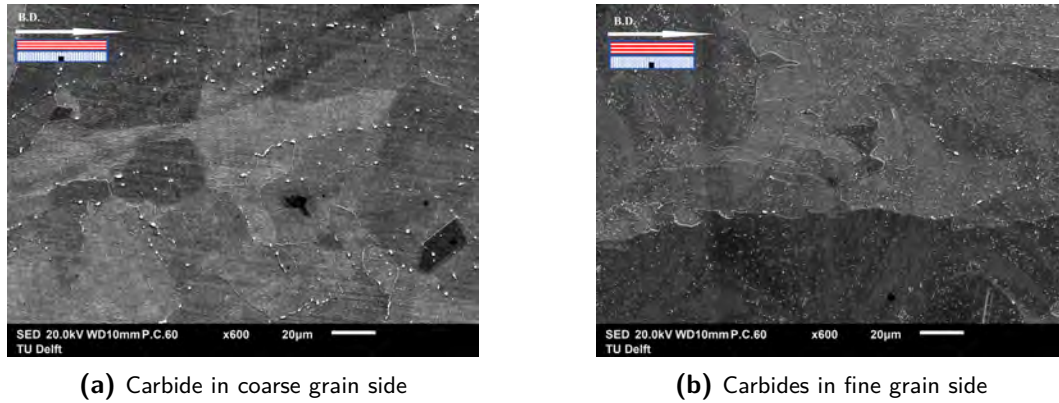


Figure 4-19: Electron micrograph of graded specimen HIP+H/T-A showing comparison of carbides in fine grain side and coarse grain side. Carbides on the grain boundaries can be clearly seen to be more in amount in coarse grain side.

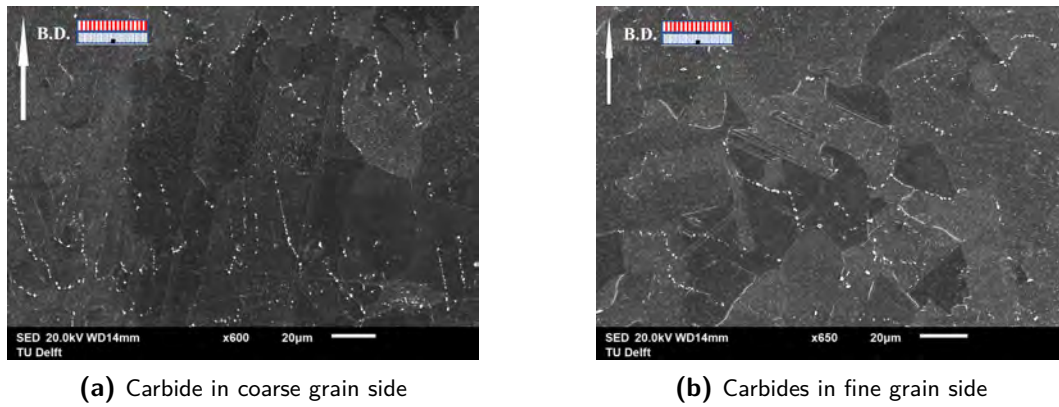


Figure 4-20: Electron micrograph of graded specimen HIP+H/T-B showing comparison of carbides in fine grain side and coarse grain side. Both the sides are observed to have the same amount of carbides unlike Figure 4-19.

Table 4-1: Table summarizing hardness values of ungraded specimens

Specimen	AP-C	AP-D	AP-E	HIP+H/T-C	HIP+H/T-D	HIP+H/T-E
Microstructure	Coarse Grain	Coarse Grain	Fine Grain	Coarse Grain	Coarse Grain	Fine Grain
Symbolic Icon						
HV ₁	303 ± 10	341 ± 9	373 ± 11	490 ± 8	501 ± 7	505 ± 10

From the results above, it can clearly be observed that the fine grain microstructure has expectedly the highest hardness values of all the ungraded specimen in both the batches. This could be attributed to the effect of the fine grains according to the hall-petch relation ($\sigma_y = \sigma_0 + kd^{-1/2}$) where the yield strength (σ_y) is linked inversely with the grain size d . Since hardness can also be considered as a measure of the yield strength as well, fine grain size should have a higher hardness.

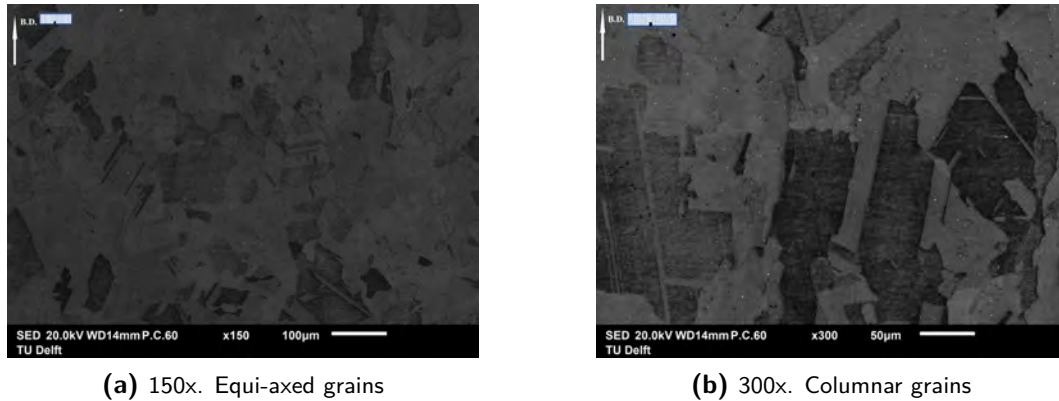


Figure 4-21: Electron micrograph of graded specimen HIP+H/T-E showing equi-axed and columnar fine grains.

Among the two coarse grain microstructures - C and D, the latter has a higher hardness in both the batches. Although, the values are very similar for the HIP+H/T batch, there is significant difference between the two in AP batch. This is probably due to the differently oriented grains which indicates that that group C has coarser grains than group D. This could be linked to the previous observation of pores being observed in group C and not in group D as the degree of porosity increases with the grain sizes as reported by previous report [78].

Finally, it is observed that the heat treatment improves the hardness significantly. The respective values of each group of specimens - C, D and E, increases by a factor of roughly 50-60% from batch AP to HIP+H/T. This is expectedly due to the emergence of the strengthening precipitates - γ' and γ'' . The reduction of pores in the HIP step also contributes to the high hardness values.

4-2-2 Graded Specimen

The graded specimens were measured for hardness values along the entire width. The hardness values are expected to decrease on moving from fine grain to coarse grain. In the figures below the hardness results from the graded specimen are shown as plots of hardness v/s distance from fine grain side edge. Figure 4-22 shows the results from specimen AP-A and AP-B and Figure 4-23 shows the same from the HIP+H/T counterparts.

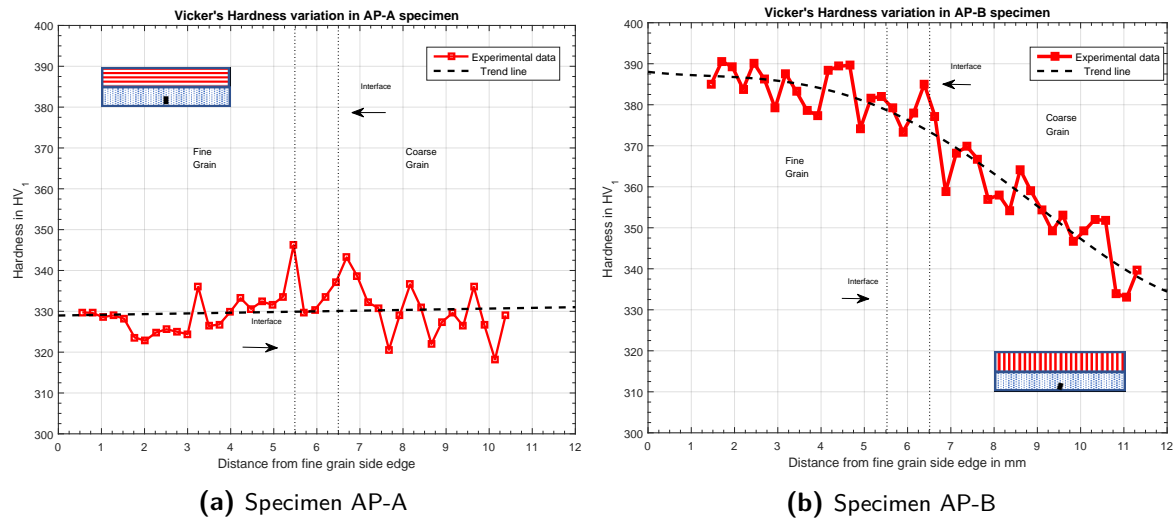


Figure 4-22: Vicker's Hardness in As-processed specimens.

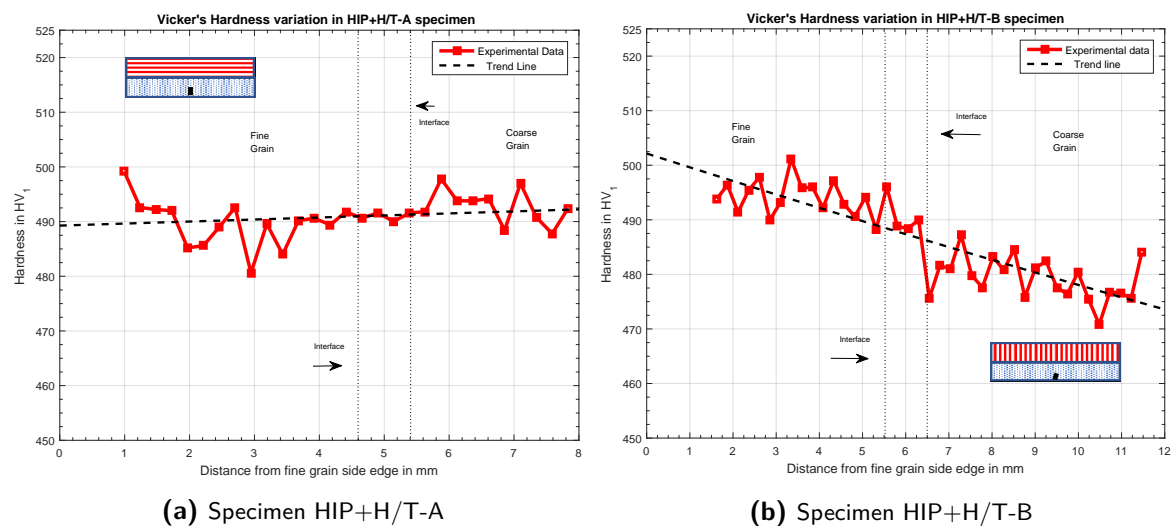


Figure 4-23: Vicker's Hardness in HIP+H/T specimens.

It is clear from the figures above that only group B in both the batch of specimens showed the expected trend of hardness. Figures 4-22b and 4-23b clearly show higher hardness values on the fine grain side which then gradually decreases towards the coarse grain side, in coherence with the trends observed in the ungraded specimens. On the other hand in group A in both the batches the values do not follow any significant trend through the width. This is suspected to be the effect of the different processing orientation that lead to the diminished difference between the two sides in group A specimens.

It can also be observed that the values of group B are also higher or at-least the same on the fine grain side as compared to the corresponding values from the ungraded specimen. However, this is not the case for group A specimens where the hardness value on the fine grain side seems to have achieved an average value intermediate between that of fine and

coarse grains found in ungraded specimen. This suggests that grain coarsening in the fine grain side in particular led to the diminished difference observed before.

4-3 X-ray diffraction

X-ray diffraction was done in the SLM specimens for phase identification and residual stress measurement. Therefore, this section is divided into the following subsections-Phase Identification and Residual Stress.

4-3-1 Phase Identification

Two specimen from each batch corresponding to coarse grain and fine grain microstructure was analyzed for the identification of the different phases present. Shown in Figure 4-24 is the summary of all the specimens. In Figure 4-25 the individual batches are also shown. In the subsequent text, the individual batches are described mentioning the evolution of the phases in the respective batches.

In the microscopy of as-processed specimens, only γ dendrites were observed. From literature mentioned in chapter 2, in addition to γ phase, these specimens in general also contain carbides and nitrides like NbC, TiC and TiN, laves phase and the δ phase. From Figure 4-25a it is observed that for these specimens phases like NbC, TiC and the laves phase are successfully detected. Both the fine grain and coarse grain microstructure are found to contain the above phases. As expected the γ phase, which were observed extensively as dendrites from microscopy, produces strong peaks as compared to the other phases. Further, TiC is only observed in the coarse grain microstructure whereas both NbC and TiC are observed in the fine grain. This could be attributed to the higher laser power leading to precipitation of TiC. δ phase mentioned above are not detected in the current specimens.

On the other hand, from microscopy it was observed that the HIP+H/T specimen contained γ phase in grains and carbides (NbC) in the grain boundaries. Additionally from literature, phases like γ' and γ'' are also expected to be present in the specimens as a result of the heat treatment. Both these phases are detected successfully in these specimens along with the γ phase and carbides as shown in Figure 4-25b. As before along with NbC, TiC is also observed in the coarse grain specimens whereas only NbC is observed in the fine grain specimen. This could be due to the same reason as above. This also suggests that emergence of carbides is dependent on the temperature levels achieved during the processing of the material and not that during heat treatment.

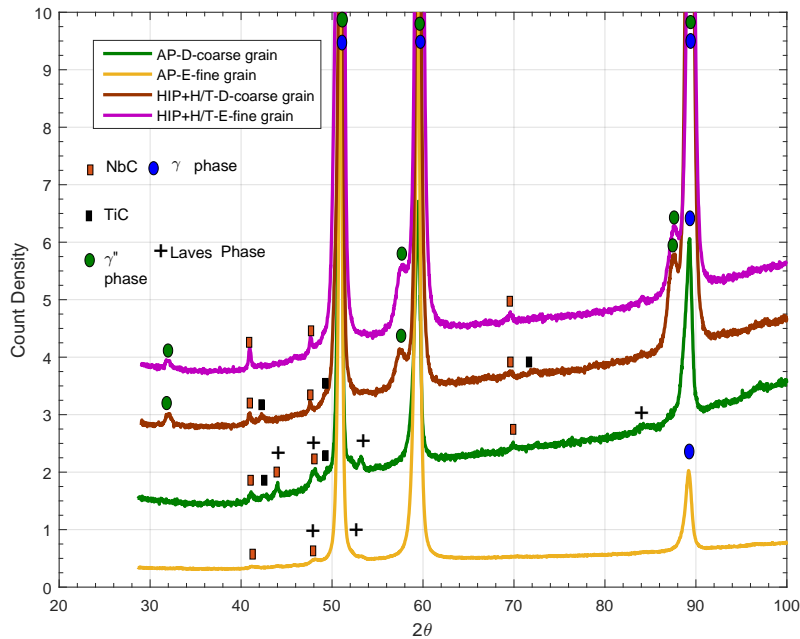


Figure 4-24: XRD peaks for different phases in all the specimens.

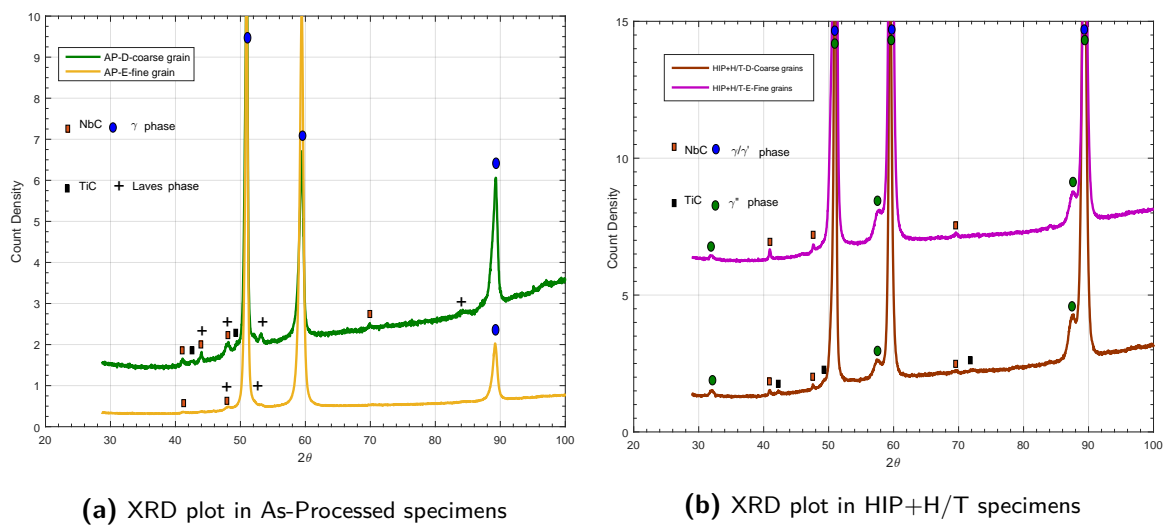


Figure 4-25: Plot showing XRD plots for both the batches

4-3-2 Residual Stress Measurement

Both ungraded and graded specimens were analyzed for residual stress. In the tables below the results are summarized separately. It should be noted that comparing various specimens for levels of residual stress and inferring relevant trends could lead to contradicting results as this measurement is highly dependent on the goodness of sample preparation in terms of

machining, grinding and polishing. Moreover for additively manufactured components where residual stresses are expected to vary with depth, machined out specimens would also result in different values of stresses for specimens of the same processing method but different position in the bulk. Therefore, only trends that are compliant with literature and produce no conflict with other trends are reported here. Further, in the $d v/s \sin^2(\psi)$ plots of these specimens the variation of the different data points were not linear, suggesting that there is a gradient in the stress levels. An example is covered in the appendix B. This could also mean that the stress also has a shear component. Nevertheless, the stresses in the current measurement are calculated assuming linear trend. It is for this reason that there is high error in some measurements.







Ungraded specimen

In Table 4-2 shown below the results from ungraded specimens are summarized. It can be observed that all the stresses detected are compressive in nature. This is attributed to the typical feature of step-wise laser based additive manufacturing that leads to compressive stresses in the interior and tensile on the surface. In the current specimens, the outer layer is interpreted to be machined leading to detection of only compressive stresses. In relation to difference in residual stress levels for both the orientation of coarse grains, it is observed that group C has lower stresses than group D in both the batches. This may be due to the processing orientation leading to better stress relaxation in C.

Further, in general, stresses are expected to be lower on the coarse grain specimens due to higher laser power leading to better stress relaxation. This is observed only for the AP specimens. In the HIP+H/T specimens the stresses are instead observed to be lower for the fine grain specimens- group E.

Comparing the AP and HIP+H/T counterparts of the specimens, it is observed that the stresses increase after the heat treatment. It has been observed so far that some precipitates dissolve and some appear after heat treatments. The increase in compressive stresses could be then attributed to the strain induced due to the appearance of the precipitates. Additionally, carbides that were observed in the grain boundaries in the previous section are known to impede grain growth. Therefore, increase in compressive stresses could also be attributed to this. However, this is not seen in the fine grain specimens.

Table 4-2: Table showing XRD results in ungraded specimens. *-The measurement of specimen AP-C was not successful before fatigue testing hence the measurements refer to post fatigue measurements,

Specimen	Microstructure	Symbolic Icon	Stress along B.D. (in MPa)	Stress perpendicular to B.D. (in MPa)
AP-C	Coarse Grain		-100 ± 23 *	-151 ± 30 *
AP-D	Coarse Grain		-368 ± 98	-259 ± 60
AP-E	Fine Grain		-480 ± 66	-377 ± 44
HIP+H/T-C	Coarse Grain		-239 ± 72	-355 ± 66
HIP+H/T-D	Coarse Grain		-552 ± 170	-503 ± 67
HIP+H/T-E	Fine Grain		-186 ± 36	-371 ± 49

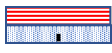
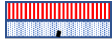

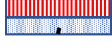
Graded specimen

Below are the results for the graded specimen in Table 4-3. As before, all the stresses found in the specimens are compressive in nature. The first relevant trend that is observed is that in the A specimens in both the batches the stresses are relatively similar on the coarse and fine grain sides as compared to the B specimens. The stresses are found to be within 30% of the coarse grain values in the AP-A specimens whereas the values in the AP-B specimens are found to differ by at least 50%. Similarly, they are found to be within 5% in the HIP+H/T-A specimens whereas it differs by at least 26% in the HIP+H/T-B specimens. This is inferred as the effect of different processing orientation leading to better reheating and subsequently better stress relaxation in group A than the other. This is in line with the observation in ungraded specimens where group C (corresponding to coarse grain of group A) had lower stresses than group D (corresponding to coarse grain of group B). The above observation was also inferred in the same way. This is specially relevant as it reaffirms the observation seen in microscopy and hardness as well. It was observed in microscopy that both the sides of group A had similar grain sizes whereas it was different in group B. In hardness it was observed that there is no variation in group A specimens whereas the general trend was observed in group B. Therefore, the effect of reheating leading to grain coarsening and stress relaxation is specially observed in group A specimens only due to its processing orientation.

With regard to the levels of residual stresses on the coarse and fine grain side for a particular specimen, it was expected that the coarse grain side should have lower stress levels due to higher laser power. This is not generally observed for all the specimens here.

The effect of heat treatment is observed here as seen in ungraded specimens. The stress values are higher in the HIP+H/T specimens than in the AP counterparts. This is inferred as before by the concept of straining of microstructure due to the emergence of precipitates. The fact that this is observed for both the graded and ungraded specimens verifies the trend of increasing residual stresses after the heat treatment.

Table 4-3: Table showing XRD of graded specimens. ^-The result was based on only two data points hence a linear trend shows no error.

Specimen	Symbolic Icon	Side	Stress along B.D. (in MPa)	Stress perpendicular to B.D.(in MPa)
AP-A		Coarse Grain	-381 ± 68	-353 ± 90
		Fine Grain	-304 ± 11	-234 ± 27
AP-B		Coarse Grain	-125 ± 28	-297 ± 13
		Fine Grain	-193 ± 45	-146 ± 38
HIP+H/T-A		Coarse Grain	-596 ± 32	-418 ± 56
		Fine Grain	-621 ± 127	-397 ± 92
HIP+H/T-B		Coarse Grain	-438 [^]	-382 ± 195
		Fine Grain	-299 [^]	-479 ± 24

4-4 Electron back-scatter diffraction (EBSD)

Shown below in Figure 4-26, Figure 4-27 and Figure 4-28 are the EBSD maps of the as processed specimens AP-C (coarse grain along length), AP-D (coarse grain along width), and AP-E (fine grain). From the figures it can be observed that the coarse grains specimens

(AP-C and AP-D) show significant $\langle 100 \rangle$ texture along the building direction similar to that reported in literature whereas in the fine grain specimen the texture is found to be absent. For comparison, the EBSD maps from the H/T wrought material is also included which also shows that the texture is not found in the conventional wrought material.

An important observation from previous sections is the difference between the differently built coarse grain specimens (AP-C and AP-D) which is also clearly observed in the difference between EBSD maps of AP-C (Figure 4-26) and AP-D (Figure 4-27) specimens. The grains are observed to be more elongated and to have stronger texture in the former than the latter which indicates that the microstructure experienced higher temperatures levels resulting from reheating during processing leading to more grain growth as reported in the previous sections.

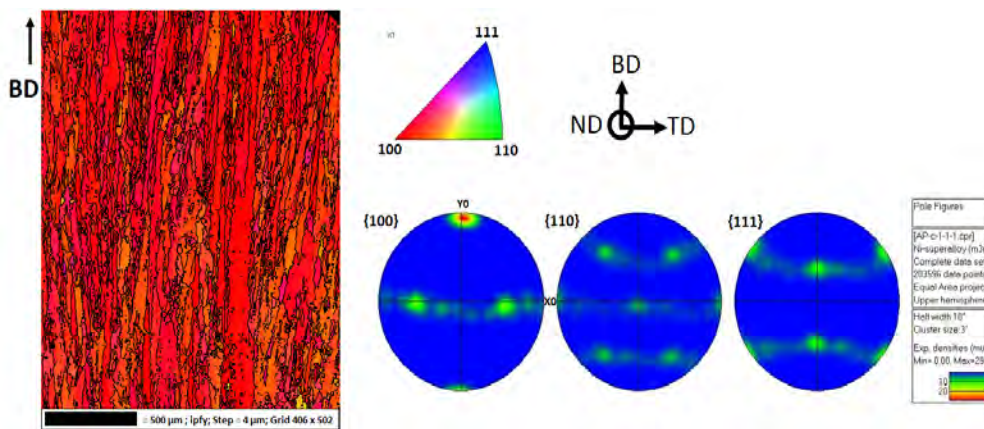


Figure 4-26: EBSD Inverse Pole Figure (IPF) coloured maps and corresponding pole figure of specimen AP-C (as processed coarse grain parallel to length)

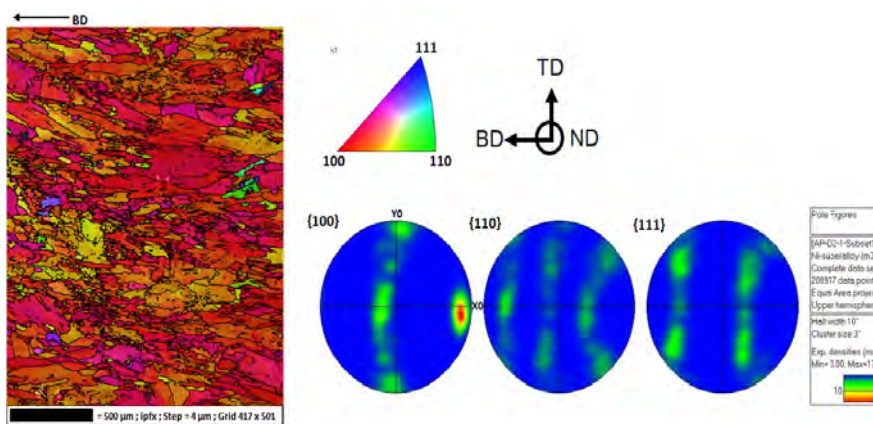


Figure 4-27: EBSD Inverse Pole Figure (IPF) coloured maps and corresponding pole figure of specimen AP-D (as processed coarse grain parallel to width)

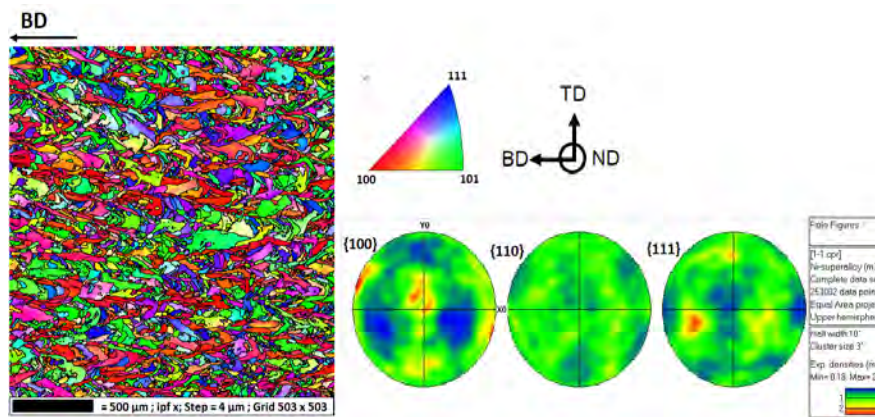


Figure 4-28: EBSD Inverse Pole Figure (IPF) coloured maps and corresponding pole figure of specimen AP-E (as-processed fine grain specimen).

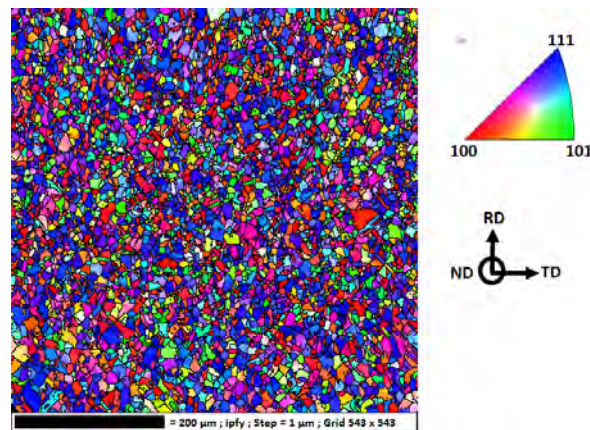


Figure 4-29: EBSD inverse pole figure (IPF) colored map of H/T wrought IN718

The average grain sizes for as-processed specimens, measured using EBSD, are mentioned in the table below. From the table, it can be seen that the grain size values also confirm the above remark that the grains in group C are coarser than group D.

Table 4-4: Table showing average grain sizes in as-processed specimens as measured from EBSD analysis.

Specimen	Symbolic Icon	Expected Grain size/orientation	Average grain Size
AP-C		Coarse grain along length	142 μm
AP-D		Coarse grain along width	93 μm
AP-E		Fine grain	71 μm
Wrought	-	-	10 μm

4-5 Summary

In this chapter the results from the microscopy, hardness and XRD results were discussed. The main observations are summarized below.

4-5-1 Microscopy

- The as-processed specimens are found to exhibit ‘u’ shaped features called melt pools in both coarse and fine grain sides. The melt pools are formed as result of the printing process.
- The matrix in the above specimens is marked by dendrites on both sides. The dendrites are observed to be oriented in the building direction in both the specimens. These dendrites are interpreted as the γ phase from literature. Further, the dendrites are observed to be spanning multiple melt-pools in the coarse grain side whereas they are largely found to be present in a single melt pool in the fine grain side.
- In comparison to literature, no pores are reported in the as-processed graded specimens. In contrast, pores are observed in the ungraded coarse grain AP-C specimens as seen in Figure 4-5. However, no such features are observed in the other ungraded specimens- AP-D and AP-E.
- The interface is marked by a distinct pattern in the AP-A specimen whereas it is marked by different sizes of the melt pools in AP-B specimen as seen in Figure 4-12. The region is also marked with pores in the AP-A specimen.
- The HIP+H/T specimens are marked by twins and carbides. Melt pool and dendrites observed previously disappear and are replaced with both columnar and equiaxed grains on the coarse and fine grain side respectively. The longer dendrites in the coarse grain side lead to the formation of the columnar grains whereas smaller dendrites on the fine grain side result in equiaxed grains. This is attributed to the effect of heat treatment leading to grain growth. However, the equiaxed grains are also sighted in the coarse grain side which is attributed to partial re-crystallization, an effect of the heat treatment as well, leading to new grains.
- The grain sizes are clearly different for only the AP-B graded specimens on both the sides. This is not very apparent in the AP-A specimens where the coarse grains are observed to be similar in size as seen in Figure 4-8a and Figure 4-17a. This is interpreted as the effect of the processing orientation that leads to better reheating and higher grain re-crystallization.
- The carbides in the graded specimens are mainly observed on the grain boundaries. From EDS analysis this is found to be NbC. In comparison to this, there is significantly less carbides in the corresponding ungraded specimens.
- Pores found in AP specimens are not observed in HIP+H/T specimens. This is interpreted as the effect of HIP step in the heat treatment that resulted in closing of the small pores.

4-5-2 Hardness

- The fine grain specimens are found to have higher hardness values (373 HV_1 in AP specimens and 505 HV_1 in HIP+H/T specimens) in both the batches according to the general trend.
- Specimens built along the length-group C had lower hardness (303 HV_1 in AP batch and 490 HV_1 in HIP+H/T batch) than specimens along the width-group D (341 HV_1 in AP batch and 501 HV_1 in HIP+H/T batch). This was due to the processing orientation leading to coarser grains in the former. The effect of orientation is due to the better reheating of the microstructure leading to grain coarsening.
- After heat treatment, the hardness increases by about 50-60% as compared to AP specimens.
- In graded specimens, the hardness variation as per ungraded specimen is only observed in group specimens. Group A has more or less constant hardness throughout. This was reasoned, as above, due to better reheating leading to diminished difference between the coarse grain and fine grain.

4-5-3 X-ray diffraction (XRD)

- In the AP specimens the phases that are detected are γ phase, carbides-NbC and TiC and laves phase. In the HIP+H/T specimens they are γ phase, γ'' phase, carbides-NbC and TiC. Expectedly it is seen that the laves phase is dissolved and the precipitate γ'' phase appears after heat treatment.
- Both NbC and TiC are observed in coarse grain specimens whereas only NbC is observed in fine grain specimens.
- The residual stresses were observed to be compressive in nature.
- Specimens built along the length-group C had lower stresses than specimens built along the width-group D. This was reasoned to be an effect of the processing orientation leading to stress relaxation in the former.
- The above phenomena was also observed in the graded specimens as group A had similar values of stresses on the coarse and fine grain side suggesting better stress relaxation due to more reheating as a result of orientation.
- Heat treatment leads to an increase of residual stresses in all the specimens. This was reasoned to be an effect of straining due to the emergence of precipitates and the pinning effect of carbides on grain boundaries during grain growth.

4-5-4 Electron back-scatter diffraction (EBSD)

- In the as-processed specimens, significant $\langle 100 \rangle$ texture along the building direction is found in the coarse grain specimens (group C and D) whereas it is absent in the fine grain specimens (group E). The EBSD maps also confirmed the evolution of different grain sizes according to different laser power used in the 3D-printing process.

- Specimens where the building direction was along the length (group C), exhibited stronger texture than specimens built along the width (group D). The former also showed higher average grain sizes than the latter which confirmed the previous observations that the grain were coarser in group C as compared to group D. This was attributed, as above, to be an effect of processing orientation leading to better reheating and more grain growth.

Results-Fatigue Behavior







5-1 FEM Simulation

This section refers to the Finite Element Modelling (FEM) simulation performed for the graded specimen. As mentioned in chapter 3, stress intensity factor K was calculated for different crack lengths. Subsequently this needed the young's modulus variation in the specimens. Hence, the results are divided into the subsections-Young's modulus from displacement and the actual results from the model.

5-1-1 Young's Modulus from displacement

The table below summarizes the results from the ungraded specimens.

Table 5-1: Table summarizing E modulus of ungraded specimens

Specimen	AP-C	AP-D	AP-E	HIP+H/T-C	HIP+H/T-D	HIP+H/T-E
Microstructure	Coarse Grain \perp to crack	Coarse Grain \parallel to crack	Fine Grain	Coarse Grain \perp to crack	Coarse Grain \parallel to crack	Fine Grain
Symbolic Icon						
E modulus in GPa	139 ± 36	136 ± 10	186 ± 15	134 ± 25	140 ± 27	173 ± 28

The values in the table above are just representative of the Young's modulus in these specimens and are only to be used in further calculations. The method used above to calculate Young's modulus was not a standard method and hence may contain many systematic errors. However, since the values in the AP batch are very close to that measured through standard methods reported in literature [13], it is assumed that the trends are nevertheless representative of the real scenario. These values are also assumed to be representative of the corresponding microstructures in the graded specimens. The value corresponding to specimen C is assumed to be representative of the coarse grain side of specimen A similarly specimen

D is linked to that of specimen B. The fine grain side in both the graded specimens is linked to specimen E. Further it is also assumed that the modulus is constant in a given side such that trends like that observed in the hardness profiles, where the hardness seemed to have a gradient all through-out, is not applicable here. Lastly the interface is assumed to have a linear gradation of modulus to match both the sides.

5-1-2 Results of the model

The values obtained above are used along with the J integral values obtained from the FEM to calculate the stress intensity K at different crack lengths. Shown in the figure below is the plot of K v/s crack ratio a/W. The actual values of the J integral and K are covered in appendix.

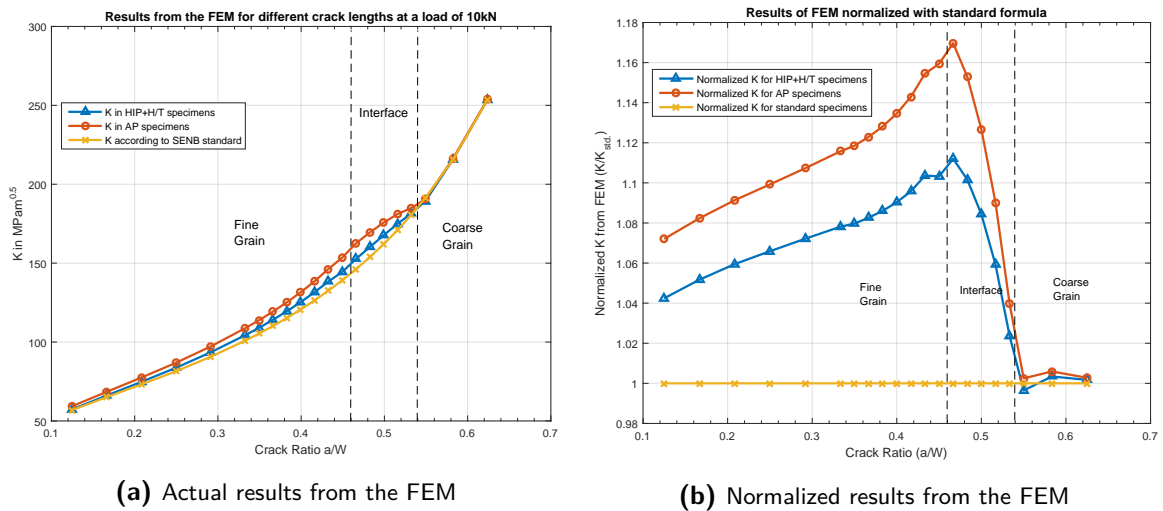


Figure 5-1: Results of the FEM showing variation of K in graded specimen of width 12mm for a constant load of 10 kN.

From the figure it can be observed that the standard stress intensity formula for SENB specimens produces errors of as high as 15% near the interface. Hence, this reaffirms the need to have customized solution based on this plot. The region after the interface is almost same as the standard solution so no other equation is necessary here. Therefore, the final equation suitable for the graded specimens is a set of equations separated by the condition of the cracklength at the end of the interface.

The equations for the pre-interface region are obtained by using suitable fits on the data shown in the Figure 5-2. It was assumed that this fit has a form same as the standard solution which is $K_{SENB} = \frac{P.S}{B.W^{3/2}} f(a/W)$. Further it was assumed that the dimensional part of the equation, $\frac{P.S}{B.W^{3/2}}$, remains the same, and only the non-dimensional part, $f(a/W)$, needs to be changed. Therefore, the data from the plot is divided by the dimensional part to get only the variation in the latter. The value so obtained is the new $f(a/W)$ and it is this data that needs to be fit and expressed explicitly.

The standard solution for $f(a/W)$ is as follows.

$$f(a/W) = 3 \left(\frac{a}{w} \right)^{1/2} \frac{\left[1.99 - \frac{a}{W} \left(1 - \left(\frac{a}{W} \right) \right) \left\{ 2.15 - 3.93 \left(\frac{a}{W} \right) + 2.7 \left(\frac{a}{W} \right)^2 \right\} \right]}{2 \left(1 + 2 \left(\frac{a}{W} \right) \right) \left(1 - \left(\frac{a}{W} \right) \right)^{3/2}} \quad (5-1)$$

From the equation it is seen that it is of the form $\frac{p(x)}{q(x)}$ where $p(x)$ is a four degree polynomial and $q(x)$ is a two degree polynomial ignoring the non-integral exponents. Therefore, the new non-dimensional part $f_{new}(a/W)$ is also checked for such a form. The results from the fit are shown in the figure below.

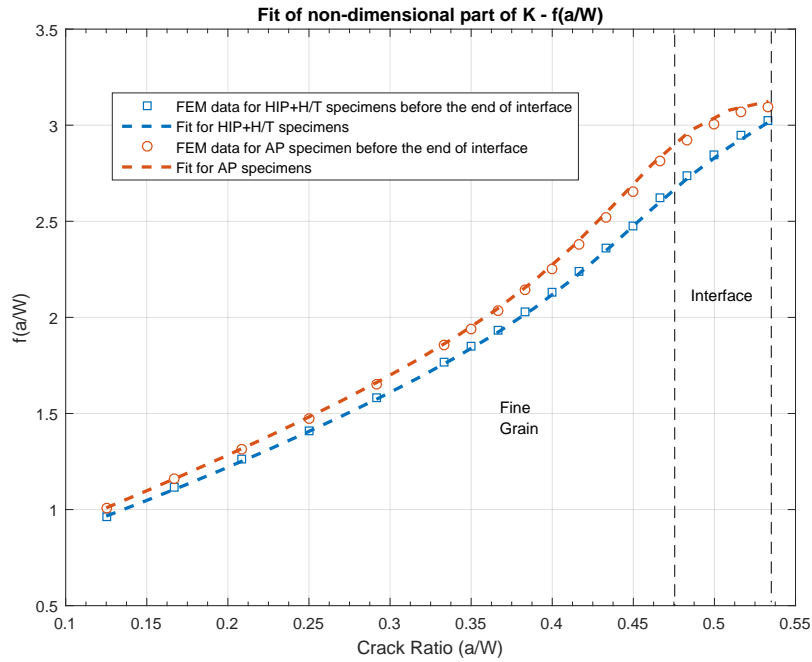


Figure 5-2: Fit of the $f(a/W)$ obtained after reducing the FEM results to just the non-dimensional part.

From the figure it is seen that the fit works accurately and the form of $f_{new}(a/W)$ is indeed what it was assumed. The $f_{new}(a/W)$ and the final K solution is summarized in the equations below.

$$f_{new} \left(\frac{a}{W} \right)_{AP} = \frac{1.275 \left(\frac{a}{W} \right)^4 + 1.878 \left(\frac{a}{W} \right)^3 - 2.113 \left(\frac{a}{W} \right)^2 + 0.1888 \left(\frac{a}{W} \right) + 0.1447}{x^2 - 0.971 \left(\frac{a}{W} \right) + 0.2438} \quad (5-2)$$

$$f_{new} \left(\frac{a}{W} \right)_{HHT} = \frac{2.617 \left(\frac{a}{W} \right)^4 + 0.1831 \left(\frac{a}{W} \right)^3 - 1.217 \left(\frac{a}{W} \right)^2 + 0.01914 \left(\frac{a}{W} \right) + 0.1384}{x^2 - 0.9355 \left(\frac{a}{W} \right) + 0.2284} \quad (5-3)$$

$$K_{AP} = \begin{cases} \frac{P.S}{B.W^{3/2}} f_{new} \left(\frac{a}{W} \right)_{AP}, & \text{if } \frac{a}{W} \leq 0.533 \\ \frac{P.S}{B.W^{3/2}} f \left(\frac{a}{W} \right), & \text{otherwise} \end{cases}$$

$$K_{HIP+H/T} = \begin{cases} \frac{P.S}{B.W^{3/2}} f_{new} \left(\frac{a}{W} \right)_{HIP+H/T}, & \text{if } \frac{a}{W} \leq 0.533 \\ \frac{P.S}{B.W^{3/2}} f \left(\frac{a}{W} \right), & \text{otherwise} \end{cases}$$

5-2 Experimental

The results from the different fatigue tests are summarized in different sections- Ungraded and Graded specimen.







5-2-1 Fatigue Characterization of Ungraded specimens

The fatigue tests on the ungraded specimens were done in order to establish the fatigue behavior of individual microstructures which was achieved through constant K_{max} and constant ΔP tests.

Constant K_{max} test

The primary goal of the constant K_{max} test was to estimate a first hand value of load levels needed for initiating a crack in the subsequent constant load amplitude tests therefore only one test was conducted. The peak load values are reported in the table below as that needed for a cracklength of 2 mm. Additionally, the threshold values are also reported. The following table summarizes the values of threshold ΔK along with the load levels.

Table 5-2: Table showing threshold values of the specimens. Load values corresponding to a cracklength at 2 mm are also shown.

Specimen	Microstructure	Symbolic Icon	ΔK_{th} in $\text{MPa}\sqrt{m}$	R (stress ratio)	Load P_{max} at 2mm in N
AP-C	Coarse Grain		7.0 ± 0.3	0.7	689.6
AP-D	Coarse Grain		6.0 ± 0.2	0.7	591.1
AP-E	Fine Grain		7.2 ± 0.3	0.7	709.3
HIP+H/T-C	Coarse Grain		8.8 ± 0.2	0.7	866.9
HIP+H/T-D	Coarse Grain		10.2 ± 0.2	0.6	1004.8
HIP+H/T-E	Fine Grain		7.7 ± 0.3	0.7	758.5

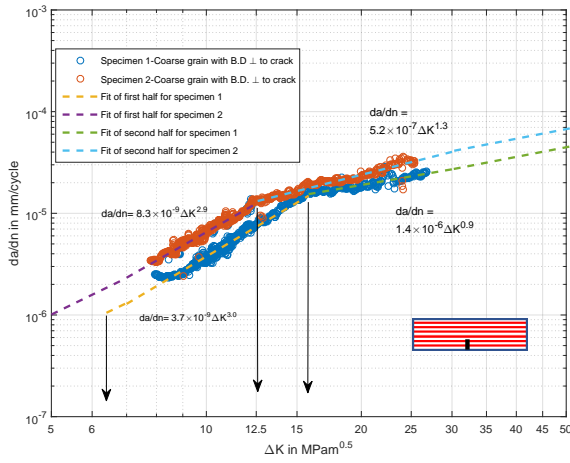
It should be noted that the above threshold ΔK_{th} results are based on only one specimen and hence the values may not necessarily represent the actual values however, the trends are assumed to more or less remain the same and are briefly discussed. From the table above it can be observed that for AP batch the fine grain specimen has the highest threshold value. This is in contrast to the general trend of fine grain microstructure of a material having lower threshold than their coarse grain counterpart. In that case the current trend could be related

to the levels of residual stresses. This is however, not observed in the HIP+H/T specimens where the values are found to be following the general trend. This indicates that the heat treatment in the current project erases effects of residual stresses. However, since this trend is based on just one test further interpretations are covered in the next subsection.

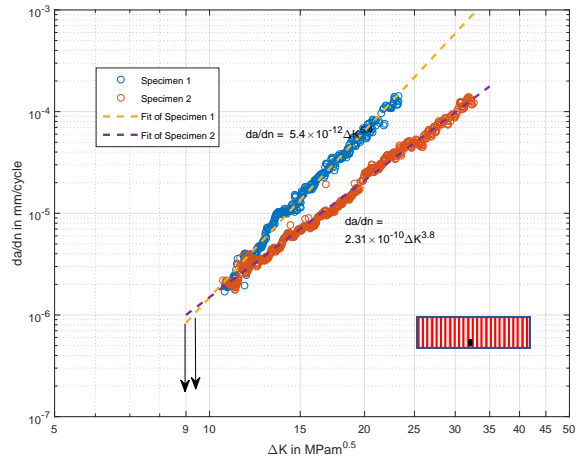
Constant load amplitude tests

These tests were conducted to establish the crack propagation behavior of the different microstructures. The raw data recorded from the MTS machine consisted of peak and valley data points of variables like the displacement of the cross head, the cycle number, the load level and the DCPD signal in each cycle. This data was first reduced through an algorithm to get uniform number of data points throughout the crack-length which can be used to calculate the da/dn and ΔK data points. This reduction methodology is mentioned in detail in appendix E.

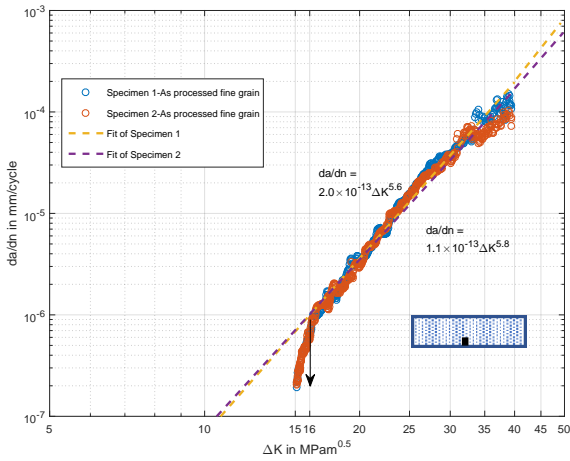
The reduced data points, consisting of only ΔK and the corresponding da/dn values, are used to construct the fatigue crack growth curves. These curves are then fit linearly in the paris regime to obtain both paris constant and the paris exponent. Two replicate tests were conducted for each type of specimen (refer Table 3-4 for summary of tests) based on which an average value of the constants is calculated. The curves are also extrapolated (if needed) to $da/dn = 10^{-6}mm/cycle$ to give an ‘operational’ value of ΔK_{th} . The operational ΔK_{th} is expected to serve as an additional information for trends observed in the different microstructures at near threshold ΔK levels. It should be noted that according to the standard ASTM-E647 the threshold is defined at a da/dn of $10^{-7}mm/cycle$ or lower hence the ΔK_{th} values used in this project are only representative of the threshold trends and not the actual values. The rationale behind the extrapolation is that below $da/dn = 10^{-6}mm/cycle$ the curve is generally not linear and a linear fit overestimates the da/dn values for a given ΔK . Shown in the figures 5-3 and 5-5 below are the raw curves of each group of specimen along with the fit and the summary of all the specimens in both batches respectively. In Figure 5-4 the results of the H/T wrought material is also shown and is also plotted for comparison in the summary of both the batches. Table 5-3 summarizes the paris constants of all the specimens. In the following text, the orientation of coarse grains in specimen C and D are mentioned in terms of the crack which was along the width. Additionally, symbolic icons mentioned in Table 3-3 are also used to denote the group of specimens.



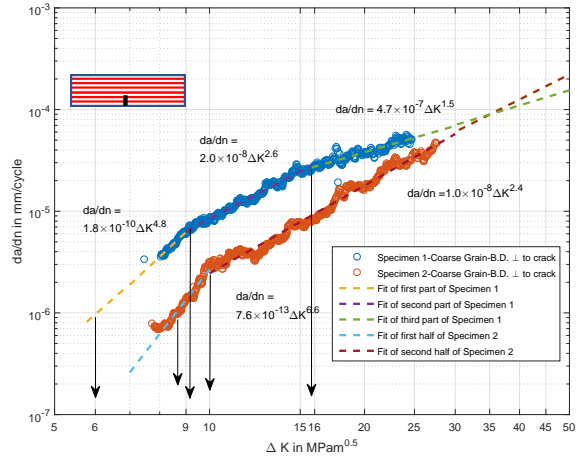
(a) Specimen AP-C - Coarse Grain ⊥ to crack



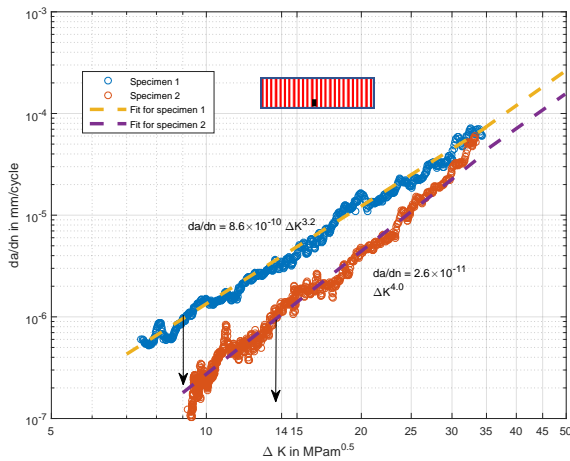
(b) Specimen AP-D - Coarse Grain || to crack



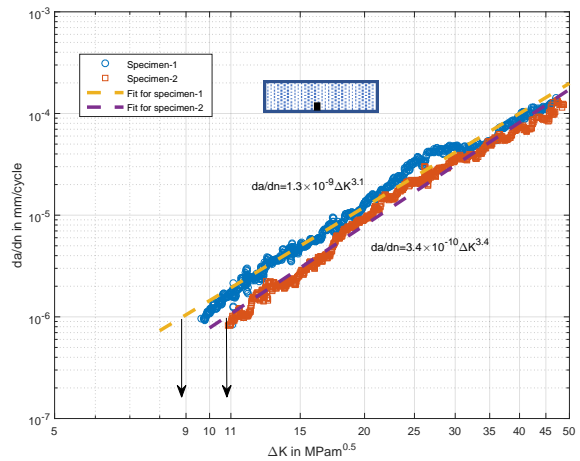
(c) Specimen AP-E - Fine Grain



(d) Specimen HIP+H/T-C - Coarse Grain ⊥ to crack



(e) Specimen HIP+H/T-D - Coarse Grain || to crack



(f) Specimen HIP+H/T-E - Fine Grain

Figure 5-3: Fatigue curves of all the ungraded specimens showing the effect of grain size, grain orientation and heat treatment.

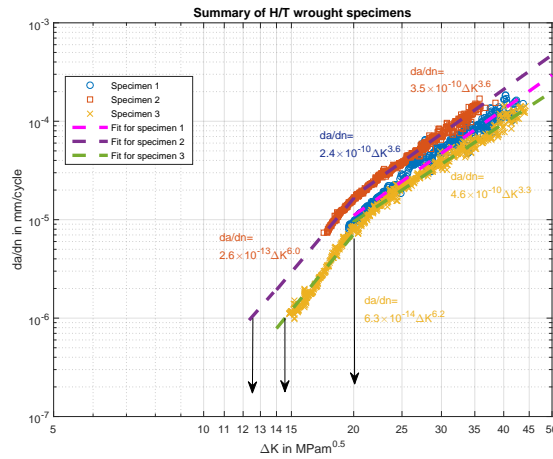
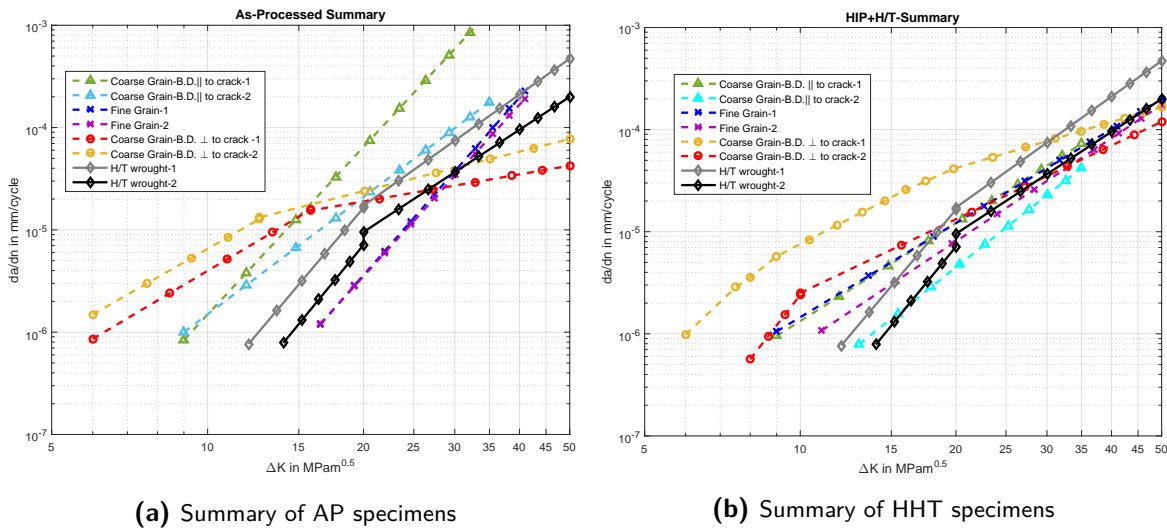


Figure 5-4: Fatigue curve of H/T wrought specimens









(a) Summary of AP specimens

(b) Summary of HHT specimens

Figure 5-5: Summary of fatigue curves of all the ungraded specimens.

In the log-log plots, the arrows at the beginning of the curves indicate the operational value of ΔK_{th} at $da/dn = 10^{-6} mm/cycle$ as mentioned above. Additionally the arrows indicate positions where linear behavior of the curves change. The operational values are summarized in the table. The plots also contain the linear fit constants of curves which is also summarized in the table below. Additionally, in the last column, the table also consists of da/dn values at a ΔK level of $16.5 MPa\sqrt{m}$ for comparing the overall fatigue performance among the specimens.

Table 5-3: Table showing the Paris constants of all the ungraded specimens

Specimen	Microstructure	Symbolic icon	ΔK_{th} (in $MPa\sqrt{m}$)	Paris Exponent m	Paris pre-exponential factor C	da/dn at 16.5 $MPa\sqrt{m}$ in mm/cycle
AP-C	Coarse Grain		6.0 ± 0.5	$m_1 = 3.0 \pm 0.1$ $m_2 = 1.1 \pm 0.2$	$C_1 = 6.0 \times 10^{-9} \pm 2.3 \times 10^{-9}$ $C_2 = 9.4 \times 10^{-7} \pm 4.3 \times 10^{-7}$	1.8×10^{-5}
AP-D	Coarse Grain		9.2 ± 0.2	4.6 ± 0.8	$1.2 \times 10^{-10} \pm 1.1 \times 10^{-10}$	1.5×10^{-5}
AP-E	Fine Grain		16.5 ± 0.0	5.7 ± 0.1	$1.6 \times 10^{-13} \pm 0.5 \times 10^{-13}$	1.0×10^{-6}
HIP+H/T-C	Coarse Grain		7.3 ± 1.2	$m_1 = 5.7 \pm 0.9$ $m_2 = 2.5 \pm 0.1$	$C_1 = 9.0 \times 10^{-11} \pm 9.0 \times 10^{-11}$ $C_2 = 1.5 \times 10^{-8} \pm 0.5 \times 10^{-8}$	5.0×10^{-6}
HIP+H/T-D	Coarse Grain		11.3 ± 2.3	3.6 ± 0.4	$4.4 \times 10^{-10} \pm 4.2 \times 10^{-10}$	4.0×10^{-6}
HIP+H/T-E	Fine Grain		10.0 ± 1.0	3.2 ± 0.2	$8.1 \times 10^{-10} \pm 4.6 \times 10^{-10}$	5.0×10^{-6}
H/T wrought	-	-	13.5 ± 1.0	$m_1 = 6.1 \pm 0.1$ $m_2 = 3.5 \pm 0.2$	$C_1 = 1.6 \times 10^{-13} \pm 0.8 \times 10^{-13}$ $C_2 = 3.5 \times 10^{-10} \pm 1.1 \times 10^{-10}$	3.2×10^{-6}

From Figure 5-3 it is observed that there is clearly a difference in fatigue behavior of the different microstructures in both the batches. This difference is more pronounced in the AP specimens (Figure 5-3a, Figure 5-3b, Figure 5-3c and Table 5-3) as both the Paris exponent m and the ΔK_{th} are observed to be different. From Figure 5-5a and the table above, it is seen that the threshold trend is the same as observed in the previous subsection. The fine grain microstructure of specimen AP-E has a higher threshold value than the coarse grain microstructures of AP-C and AP-D. This confirms the previous observation. As mentioned before, this is opposite to the general trend and could be attributed to the levels of residual stresses. In the previous chapter, it was reported that the residual stresses in the specimens were compressive and increased from group C to E in the as-processed batch (Table 4-2). Therefore, it can be imagined that group E which has the highest amount of residual stresses, will lead to higher ΔK_{th} as the effective ΔK is now lower than measured. On the other hand in the HIP+H/T specimens (Figure 5-3d, Figure 5-3d, Figure 5-3d), this difference is relatively diminished specially between group D and group E. Although, the threshold is reported higher for group D (Figure 5-3), it should be noted that the values of both the groups are within the scatter of each other. Whereas group C has clearly lower threshold value than the other two. Although, both group C and D are expected to be coarse grains (with different orientation mentioned before), the trend observed here indicate that only the former clearly has coarser grains in comparison to fine grain microstructure of group E. This is also inline with the observations from the previous chapter where group C was reported to have different properties than group D due to better reheating in the former. The hardness and residual stresses were lower in the former indicating coarser grain. Therefore, this shows that the difference in threshold values depending on the grain sizes follows the same trend as observed in the AP specimens. This could also be explained in terms of residual stresses as before with the exception of HIP+H/T-E where the residual stresses were found to be the least. On the other hand, the similarity between group D and group E then could be attributed to the effect of heat treatment leading to grain growth in both the specimens leading to less difference in grain sizes and thus fatigue behavior. Additionally this similarity is also reflected in the Paris constants m and C (see Table 5-3) and the da/dn values of these specimens. It could be argued that the significantly lower residual stresses in group E as compared to group D should have resulted in lower ΔK_{th} . But as it appears, the effect of coarse grains leading to higher ΔK_{th} is more than that of residual stresses in this particular case. Further on the

trends are covered in the next chapter.

Another distinguishing observation from the figures is the behaviour of group C in both the batches. The curves are seen to be piecewise linear unlike the single linear curves observed in groups D and E. The slope in the beginning of the curves is significantly higher as can be inferred from the figure and the table. From Figure 5-4 it is seen that the piecewise linear curve is also observed in the H/T wrought specimens. This behaviour has been reported in literature and is attributed to different mechanisms of crack growth. However, specimen HIP+H/T-E, which resembles H/T wrought material in terms grain size and appearance of precipitates, doesn't have this behavior. On the other hand group C, where this is seen, has been reported so far to have relatively coarser grains. Therefore, the effect of grain size in this trend could not be confirmed. Further, this behavior is observed in both the batches (Figure 5-3a and Figure 5-3a) which highlights the fact that the effect might not be due to the strengthening phases. Hence, further microscopy of the crack path is needed to pinpoint the crack behavior in this specimens which is covered in the next chapter.

In addition to the effect of heat treatment mentioned above, changes in the individual specimens are also observed. The threshold value is generally seen to improve after heat treatment. This is also visible in the da/dn values reported in the last column of the table above. Although, an exception is observed for group E, the increase in these values is expected based on literature [101]. The heat treated material is devoid of the brittle laves phase and contains the precipitates γ'/γ'' phases which leads to higher resistance of dislocation glide and thus higher ΔK to propagate the crack. Further group E also had an exception of decrease of residual stresses upon heat treatment as seen in Table 4-2 therefore, it could be the case that the increase in group E is more than compensated by this decrease in these specimens. It should be noted that the decrease in residual stresses could not be explained in the current analysis. However, this doesn't explain the similarity between group D and group E especially when the residual stresses are observed to be significantly different.

Additionally, in comparison to the H/T wrought material, HIP+H/T fine grain specimens are expected to be similar in behavior. However, as mentioned above and seen from Figure 5-5b the similarity in the curves is only reflected at higher ΔK . The piecewise linear trend leads to higher slopes at lower ΔK leading to deviation from the latter specimens. As mentioned above, this piecewise linear trend is reported to be possible, the fact that this is not seen in the similar HIP+H/T specimens is interesting. This is further covered in the next chapter. With respect to the overall fatigue performance, only one group of printed material can be ascertained to be behaving better than the wrought material. This observation is made based on the ΔK_{th} . It should be noted that the threshold values of the wrought specimens are similar to that observed in literature as well (refer page 27). Similarly on the basis of da/dn value at $\Delta K = 16.5 \text{ MPa}\sqrt{\text{m}}$ shown in the last column of Table 5-3 the behavior can also be compared. Based on the values, lower the da/dn , better the performance of the concerned specimen. It is interesting to note that the group that performs better than wrought specimens is AP-E that is fine grain material in the as-processed condition. On the other hand all HIP+H/T specimens perform worse than the wrought specimen in the lower ΔK range.

5-2-2 Fatigue Characterization of Graded specimens

The graded specimens were tested with constant ΔK tests to observe the effect of FGM on the fatigue crack growth. The crack growth rate is expected to change as the crack grew from one side to the other. Since these tests were carried under a constant ΔK , any change in crack growth rate is expected to be due to the change of microstructure. It is also expected that the crack may change its path on encountering textured material while growing from the fine grain side to the coarse grain side at least in the AP specimens. This will be checked with the help of DIC in these tests. In the figures below Figure 5-6 and Figure 5-7, the results of both the batches are summarized in da/dn v/s crack-ratio (a/W) plots.

In the figures below the dotted lines refer to the corresponding crack growth rate in the ungraded specimens at the given ΔK . In the fine grain side the line corresponds to the crack growth observed in the group E specimen, and on the coarse grain side the lines correspond to both group C and group D for comparison with group A and B respectively. Further it should be noted that two tests were conducted for each group and batch. The reader is referred to Table 3-4 for the details of the tests.

AP-As Processed

In Figure 5-6 the results from as processed specimens are summarized. From the figure it can be observed that the crack growth rate in group A doesn't change significantly from fine grain to coarse grain side. The da/dn for the pink curve is observed to be between $4-5 \times 10^{-5}$ mm/cycle on both sides. Although, the crack growth rate is almost the same on both sides, it is higher than the corresponding crack growth rates from the ungraded specimens. The da/dn in fine grain ungraded specimen was 6×10^{-6} mm/cycle and that in the coarse grain ungraded specimen was 3×10^{-5} mm/cycle. This suggests, as previously observed, that the processing of group A specimens lead to extensive reheating of the specimens resulting in grain coarsening on both sides. The grains in this specimen are then expected to be coarser than the ungraded coarse grain specimen AP-C leading to even higher crack growth rates. It should be noted that in the previous subsection, the higher crack growth in coarser grain was linked to lower compressive residual stresses. Therefore, if the stresses are lower in the graded specimens than the corresponding ungraded specimens, the effect of grain coarsening can be confirmed. From Table 4-3, it is seen that although, this can be confirmed for the fine grain side, it could not be confirmed for the coarse grains side.

Further, it is observed that the crack growth rate in the interface first decreases then increases towards the coarse grain. The increase in crack growth can be attributed to microstructural features in the interface region. From Figure 4-12, it was observed that the interface region is marked with pores in AP-A specimen. Thus it can be attributed to the linking of cracks from all the pores that leads to faster crack growth. It could also be attributed to the change in grain sizes in the interface. But the difference in grain sizes is observed above to be diminished on both the sides, therefore, it is unlikely that the change in grain sizes could be a contributing factor. On the other hand the decrease in da/dn as the crack enters the interface could not be reasoned in the present study. Further discussion is covered in the next chapter. The scenario in AP-B specimens is completely different as compared to AP-A. The da/dn in the beginning of the specimen was too slow at $\Delta K = 22.5 MPa\sqrt{m}$ therefore, they were tested

at $\Delta K=25MPa\sqrt{m}$. It is observed in these specimens that the da/dn increases throughout the width unlike that in AP-A specimen where it remained constant. This was also observed in the previous chapter where the gradient in properties was only observed in group B specimens. The increase in da/dn is then attributed to the gradient in grain sizes (and therefore a decrease in compressive residual stresses) all throughout the width and not just in the interface. It is also observed that unlike in AP-A specimen where the da/dn was higher than the corresponding ungraded crack growth rates, the da/dn in this specimen is lower than that in the corresponding ungraded specimens. This difference in behavior could not be reasoned with the help of compressive stresses as they found to be lower in comparison to the ungraded specimen. A possible explanation could be the toughening effect of the small amount of grain coarsening that results in lower da/dn .

The behaviour in the interface is the same as mentioned above. The da/dn is seen to increase monotonically in the interface resulting from the gradient in grain sizes. Further repeat tests on similar specimens confirm the trends for both the groups of specimens. The reader is referred to appendix G for the complete plots.

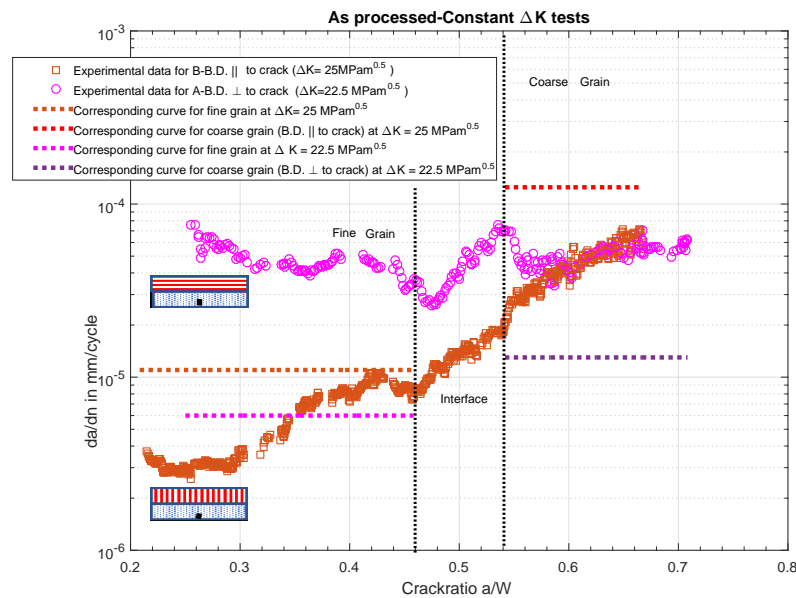


Figure 5-6: Fatigue crack growth rate da/dn under constant ΔK as a function of crack ratio in as-processed-A and B specimens. Symbolic icons near the curves show the corresponding group of specimen.

HIP+H/T

In Figure 5-7 the results from HIP+H/T specimens are summarized. The behaviour of the HIP+H/T specimens is observed to be the same for both the groups unlike that in AP specimens where it was different for both groups. The da/dn is observed to remain constant on the fine grain side which increases in the interface to match that in the coarse grain side. The da/dn for group A is observed to be around $3 - 4 \times 10^{-5}$ mm/cycle for fine grain side whereas it is $4 - 6 \times 10^{-5}$ mm/cycle in the coarse grain side. The same for group B is observed to be around 3×10^{-5} mm/cycle for fine grain side and around $3 - 4 \times 10^{-5}$ mm/cycle for the

coarse grain side. The da/dn is also found to be higher than the corresponding crack growth found in ungraded specimen. For fine grain ungraded specimen, it was 1.3×10^{-5} mm/cycle and 3×10^{-5} and 7×10^{-6} mm/cycle for group C (compare to $4 - 6 \times 10^{-5}$ mm/cycle in A) and group D (compared with 3×10^{-5} mm/cycle in B) coarse grain specimen respectively. This is attributed to the grain coarsening experienced under heat treatment. It should be noted that this is unlike the grain coarsening as a result of processing reported previously. The heat treatment leads to grain coarsening on both the specimens thereby removing differences in grain size and orientation. It is, therefore, for this reason that both the groups behave alike. However, the higher crack growth rate on both sides and both groups because of grain coarsening as compared to the da/dn in corresponding ungraded specimens could not be linked to the residual stresses as before. Similarly the behavior in the interface leading from gradually changing grain size also could not be explained in terms of residual stresses. As before, repeat tests showed similar trends and are covered in appendix G.

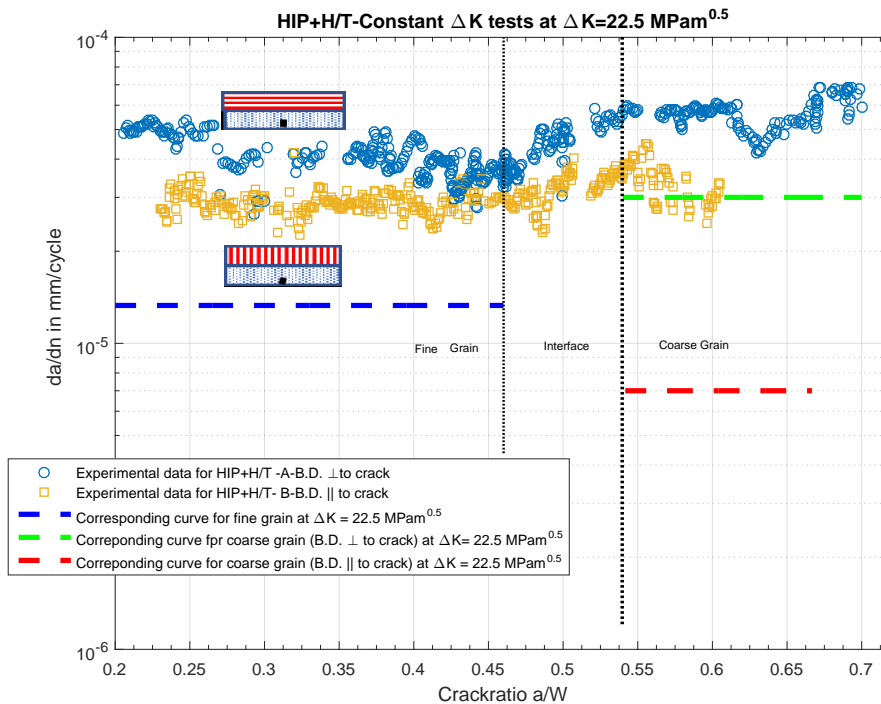










Figure 5-7: Fatigue crack growth rate da/dn under constant ΔK as a function of crack ratio in HIP+H/T-A and B specimens. Symbolic icons near the curves show the corresponding specimen.

The results above are also summarized in Table 5-4 .

Table 5-4: Table showing the crack growth rates in graded specimens at constant ΔK with comparison to the corresponding ungraded microstructures.

Specimen	Symbolic Icon	Side	Crack growth rate (da/dn) (in mm/cycle)	Corresponding ungraded specimen	Symbolic icon	Corresponding crack growth rate (da/dn) (in mm/cycle)
AP-A		Coarse Grain	$4-5 \times 10^{-5}$	AP-C		3×10^{-5}
		Fine Grain	$4-5 \times 10^{-5}$			AP-E
AP-B		Coarse Grain	$3-5 \times 10^{-5}$	AP-D		1.2×10^{-4}
		Fine Grain	$3 \times 10^{-6}-10^{-5}$			AP-E
HIP+H/T-A		Coarse Grain	$4-6 \times 10^{-5}$	HIP+H/T-C		3×10^{-5}
		Fine Grain	$3-4 \times 10^{-5}$			HIP+H/T-E
HIP+H/T-B		Coarse Grain	$3-4 \times 10^{-5}$	HIP+H/T-D		7×10^{-6}
		Fine Grain	3×10^{-5}			HIP+H/T-E

5-3 Digital Image Correlation

In Table 3-4 it was mentioned that one specimen from each group of graded group was tested with DIC in this project. The main goal of the DIC was to pin point strain localization as the crack grows through the interface. Additionally DIC would also show crack deflections. As seen from the plots in the previous section, the crack growth in the interface region increases gradually in all the specimens. Although, a small decrease in da/dn was observed in AP-A, the overall trend was reported to increase. Interpretations from the above results suggest that phenomena like deflections could not have taken place as it would have led to an overall decrease and not an increase in da/dn . This is also confirmed from the figures below.

It is important to note at this point that DIC is an extremely sensitive procedure where the analysis is highly dependent on the quality of the images recorded. In the current set-up, test conditions like available atmospheric light and reflections from the surrounding affected the image quality. Therefore, the analysis didn't produce theoretically consistent results. From the figures below, it is observed that strain is localized in regions far away from the crack. This is not consistent with theory and is attributed to errors in the analysis arising out of bad quality images. Anyhow the images are reported for completeness sake.

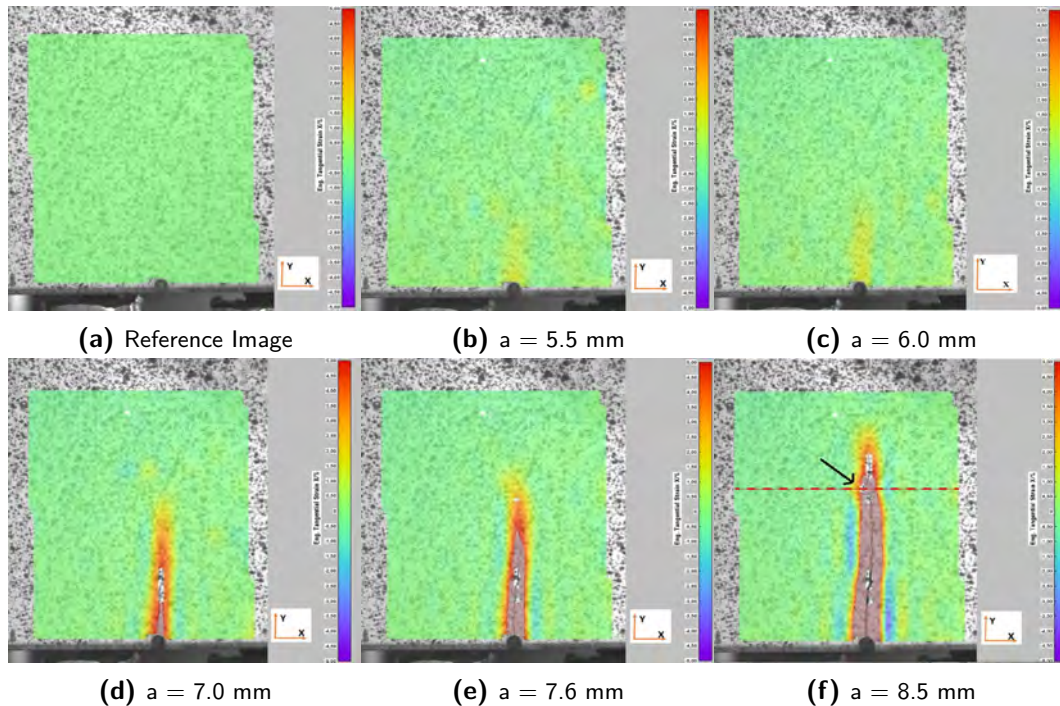


Figure 5-8: DIC image in AP-B specimen. The color scale ranges from a strain of -5% to 5% in the X direction. The red dashed line in (f) represents the interface and the arrow shows a curvature in the crack path in the interface region.

As reported above, the test in AP-B specimen resulted in high scatter in the da/dn curves which was attributed to asymmetrical crack growth. In the images above (Figure 5-8a, 5-8b and 5-8c), the crack length estimated from the other face of the specimen was at the mentioned crack lengths but if estimated from the image it appears to be less. Similarly in Figures 5-8d and 5-8e, the crack lengths are also found to be less than that reported from the other face. Anyhow, it is interesting to note in Figure 5-8f, the curving of the crack at the position marked by the arrow. This was found at a crack length of 6 mm which is in the interface region. This could be interpreted as a possible effect of the interface, however, as the crack was asymmetrical when it crossed the interface, it can not be attributed individually to be a consequence of the former.

Similarly, the results from the HIP+H/T specimens (Figure 5-9 and 5-10) also produce inherent errors. The images in group A show, as before, a region of high compression in the region away from the crack where theoretically no stress is experienced. Similarly in group B there is a region of compression just outside the strained part around the crack. This is invalid according to theory and is also attributed to errors from the procedure. Nevertheless, no special features like crack curving are observed here, as seen above. The crack in these specimens was more or less symmetric on both sides.

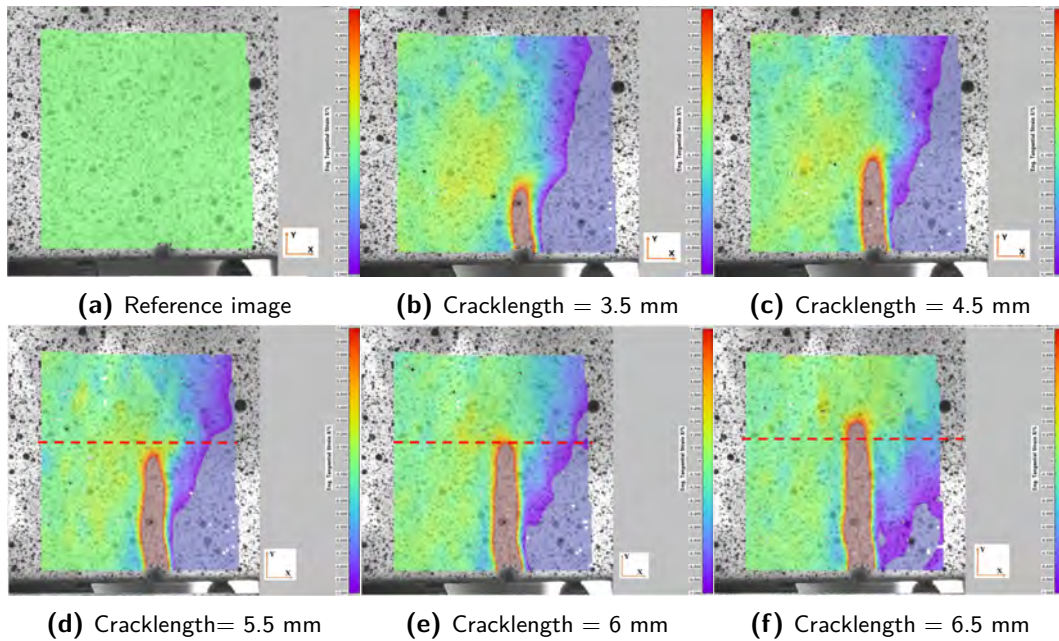


Figure 5-9: DIC images for HIP+H/T-A. The color scale ranges from a strain of -1% to 1% in the X direction. The bluish region on the right side of the cracks comes from errors in the DIC procedure. The red dashed lines in (d), (e) and (f) represent the interface region.

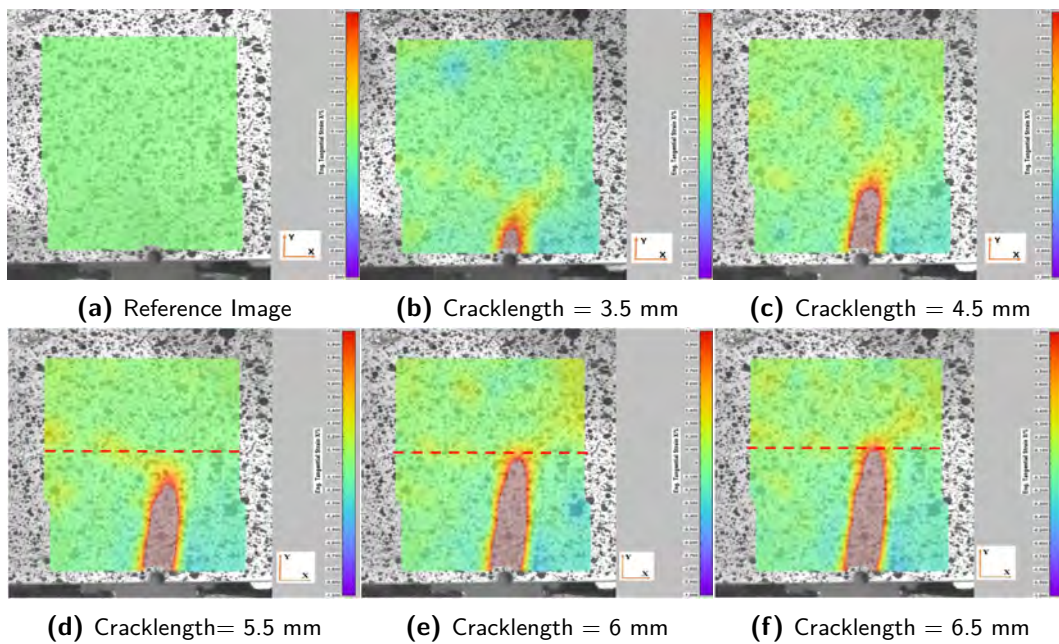
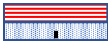






Figure 5-10: DIC images for HIP+H/T-B. The color scale ranges from a strain of -1% to 1% in the X direction. The red dashed lines represent the interface in (d), (e) and (f).

5-4 Summary

The results mentioned in this chapter can be seen in the following overview table and are also summarized below.

Table 5-5: Table summarizing the fatigue parameters used to assess both graded and ungraded specimens.

Group	Symbolic Icon	Primary Parameter used	Value in AP	Value in HIP+H/T
Group-A		Crack Growth rate (da/dn) (in mm/cycle)	Coarse grain : $4-5 \times 10^{-5}$ Fine Grain : $4-5 \times 10^{-5}$	Coarse Grain : $4-6 \times 10^{-5}$ Fine Grain : $3-4 \times 10^{-5}$
Group-B		Crack Growth rate (da/dn) (in mm/cycle)	Coarse Grain : $3-5 \times 10^{-5}$ Fine Grain : $3 \times 10^{-6}-10^{-5}$	Coarse Grain : $3-4 \times 10^{-5}$ Fine Grain : 3×10^{-5}
Group-C		ΔK_{th} (in $\text{MPa}\sqrt{m}$)	6.0 ± 0.5	7.3 ± 1.2
Group-D		ΔK_{th} (in $\text{MPa}\sqrt{m}$)	9.2 ± 0.2	11.3 ± 2.3
Group-E		ΔK_{th} (in $\text{MPa}\sqrt{m}$)	16.5 ± 0.0	13.5 ± 1.0

5-4-1 Ungraded specimens

- The following trend was found for ΔK_{th} in the 3D-printed, as-processed (AP) specimens: AP-C (coarse grain perpendicular to crack) < AP-D (coarse grain parallel to crack) < AP-E (fine grain). Similar trend was observed in post heat treated (HIP+H/T) specimens although, the difference is significantly diminished therefore Hence, in both AP and heat treated samples the coarse grain microstructure showed lower threshold than the fine grain microstructure. This is opposite of the general trend and is explained by the effect of compressive residual stresses that lead to low effective ΔK .
- Group with coarse grains perpendicular to crack (AP-C) showed a piecewise linear fatigue in both AP and heat treated condition. The trend is similar to the curve observed in conventional H/T-wrought specimens. This trend was however not observed in the other groups (D and E), which should be further investigated via microscopic analysis, as there is currently no literature/study available to explain this behavior in 3D-printed materials
- The threshold and the da/dn values increase following heat treatment which is attributed to the disappearance of Laves phase and pores as well as precipitation of the strengthening phases γ'/γ'' . Opposed to that, the fine grain specimen, which already had a very high ΔK_{th} in the AP condition due to large compressive stresses, had rather lower ΔK_{th} in the heat treated condition due to lower compressive stresses.

5-4-2 Graded specimens

- The standard formula for K produces an error of as high as 15% near the interface. New equations were formulated using FEM and Young's modulus data calculated from deflection in bending tests.
- The crack growth rate in AP-A (graded microstructure built along length) group remains more or less the same throughout the width. This is attributed, as before, to the

processing orientation leading to better reheating and less difference the free sides of the graded microstructure. The growth in da/dn in the interface could be linked to pores and distinctly different microstructure in the interface region.

- AP-B (graded microstructure built along width) had a continuously accelerating crack growth. This was inline with previous trends observed for this group and is attributed to continuously changing grain size in the interface region.
- The crack growth rate in AP-A (graded microstructure built along length) is found to be more than the corresponding ungraded microstructure (refer Table 5-4 in page 85). This is explained by stress relaxation as a result of reheating during processing thereby leading to lower compressive stresses. This was also confirmed from residual stress measurements in the fine grain side.
- The crack growth in AP-B (graded microstructure built along width) is found to be less than the corresponding ungraded microstructure (refer Table 5-4 in page 85). This was explained by the grain coarsening experienced during processing that lead to toughening of the microstructure.
- The behavior in the HIP+H/T specimens in both the groups is observed to be the same. The crack growth rate is found to increase slightly from the fine grain side to the coarse grain side as seen in the corresponding ungraded specimens. The similarity was attributed to the heat treatment leading to grain coarsening in both the groups while the increase in crack growth rate in the interface is attributed to the effect of the increasing grain size
- The crack growth in HIP+H/T specimens is found to be more than the corresponding ungraded specimens. This is also attributed to the grain coarsening as above.

Based on the above it can be concluded that fatigue behavior of 3D-printed Inconel 718 is affected by the grain size, grain orientation, residual stress and precipitates. Further discussion regarding the relation between microstructural features and fatigue behavior will be given in chapter 6.

Relation between microstructural features and fatigue behavior

The results from the previous chapters are further discussed here to develop answers to the research questions mentioned in chapter 2 in page 35 which is also mentioned below.

1. How does the individual microstructure and mechanical properties develop during 3D-printing of Inconel 718
2. What is the effect of post process heat treatment on individual microstructure and mechanical properties
3. How does the fatigue parameters obtained for ungraded Inconel 718 depend on the various microstructural features like grain size, grain orientation, residual stresses, etc.
4. What is the difference between fatigue properties of 3D-printed and conventional wrought Inconel 718
5. Based on the results of this study and literature can the developed herein relations be used to tailor fatigue behaviour in 3D-printed functionally graded materials

In the following, the above mentioned research questions are addressed in detail in separate sections.

6-1 Research Question 1 : Evolution of microstructural features and mechanical properties

In Chapter 4, the results showed that microstructure of the 3D printed material had significant difference in terms of the laser power used and the resulting grain size. Furthermore, the effect of building direction was also seen in terms of different hardness and grain sizes in microstructures processed with same laser power. Therefore to answer the first research question, the following discussion is included.

6-1-1 Evolution of microstructure with respect to grain sizes

The evolution of different grain sizes was seen in all the sections chapter 4. In microscopy, the grain size was clearly observed to be different for specimens processed with different laser powers. In the specimens processed with 250 W laser power, the dendrites was restricted to only a single melt pool thereby resulting in fine grains whereas in specimen processed with 950 W laser power they spanned several melt pools resulting coarse grains. The effect of laser power was covered in chapter 2 where longer melt pools were mentioned to result from higher power. Hence, 950W laser power resulted in larger melt pools and growth of the grains. This was also confirmed in the EBSD analysis which showed elongated grains (and higher average grain sizes, 142 μm in group C and 93 μm in group D) in specimens processed with 950 W and smaller grains (71 μm) in the other (group E). The EBSD analysis showed that the coarser grain specimens had significant $\langle 100 \rangle$ texture which was absent in the fine grain specimens (refer Figures 4-26,4-27 and 4-28 in page 68). This was also covered in the previous project by Popovich et. al [13, 78]. In addition to that, one of the as-processed coarse grain specimens (AP-C) also contained several pores which was not observed in the fine grain specimen. Porosity was also reported to be higher in the coarse grain in the previous project [13]. This was attributed to volume shrinkage during the processing. In the HIP+H/T specimens, the difference in grain sizes, although diminished, was still observed. The coarse grain specimens were marked mainly columnar grains directed along the building direction whereas the fine grains are marked by equi-axed grains. The change of dendrites to columnar and equi-axed grains was attributed to the effect of heat treatment (discussed below). Grain growth in the heat treatment resulted in the large dendrites of the coarse grain side to transform to columnar grains whereas the smaller ones transformed to more equi-axed grains. The appearance of equi-axed grains in the coarse grains can be attributed to recrystallization. It was reported in the previous project that recrystallization occurs in the HIP step of the heat treatment due to the high temperature levels leading to new grains. Therefore, this also explains diminished difference between coarse and fine grains.

The difference in hardness was also observed between the coarse and fine grain specimens. According to the theory of Hall-Petch, fine grain microstructure results in higher hardness due to the strengthening effect of the grain boundaries. This is also observed here where the hardness was higher in the fine grain specimens for both the batches. The difference in hardness was again observed to be diminished in the HIP+H/T specimens. This could be linked with the above discussion. Grain growth and recrystallization lead to less difference in grain sizes and therefore, less difference in hardness values as well.

The difference in the specimens having different grain sizes was also observed in the XRD measurements. Carbides detected in the coarse grain specimens consisted of both NbC and TiC, whereas only NbC is observed in the fine grain specimens. This was seen in both the batches suggesting that the carbides formed during the processing and grew further in the heat treatment. The temperature range of formation of MC type carbides is in the range of the 1100-1200°C which is already achieved during the processing. The HIP step of heat treatment also has a temperature of 1180°C which also contributes to further growth. The formation of NbC has been reported as a natural consequence of the eutectic reactions of the Ni-Nb-C ternary system during solidification whereas the formation of TiC needs higher temperature levels which was probably achieved during higher laser power [3]. Therefore, the coarse grain contains both NbC and TiC and only the former in the fine grain specimen. The residual stresses in the coarse grain specimens were expected to be lower than the fine

grain specimens however, this was not confirmed in the current project. This is observed in the as-processed specimens but not in the HIP+H/T specimens. The compressive residual stresses in the as-processed specimens could be attributed to the repetitive heating leading to compressive stresses near the core of the and tensile stresses at the edge of the specimens. This was also reported by other works [102, 103].

6-1-2 Evolution of microstructure with respect to different grain orientation and FGM

The effect of grain orientation was seen along with the effect of the grading and therefore, it is discussed together. The effect of grain orientation refers to the differences in results observed in group C, where grains are oriented parallel to length and group D, where grains are oriented parallel to width. The effect of grain orientation alone is observed in all the measurements covered in chapter 4. In microscopy, specimens of group C had significantly higher porosity than group D where no such features were observed. In hardness measurements, group C is observed to have lower values than group D. Similarly in XRD measurements group C has lower stress values than group D. Although, the measurements for group C in the as-processed batch was done post-fatigue, the trend observed is consistent with the other observations. Similarly, in the EBSD analysis group C showed stronger texture and higher average grain sizes than group D (refer Table 4-4 in page 69). This was explained to be a result of better reheating during processing leading to better stress relaxation and higher grain growth.

The effect of grain orientation was also seen in graded material. The two groups of graded specimen, A and B had different grain orientations corresponding to group C and D respectively. In microscopy the difference between both the groups were observed in the HIP+H/T batch where the difference in grain sizes was only seen in group B while it was largely the same for A specimens. In hardness measurements, the variation was only observed in group B similarly in XRD group A had relatively less difference in stress values on both sides than group B. This was explained using the same interpretation as mentioned in the paragraph above. This is consistent with the previous observation as group C corresponds to the coarse grain side of group A in terms of the grain sizes and had the same building direction. Therefore, the specific orientation that leads to better reheating in group C before also resulted in a similar effect in group A. This effect of better reheating arising out of the particular building direction needs to be confirmed with temperature profiles calculated using Finite Element Modelling (FEM). However, analytically it can be imagined that when the building direction is along the length of a cuboid specimen, the newly solidified layer experiences less time cooling down than when the building direction is along the width. In such a scenario it can be expected that the former experiences higher temperature levels.

The effect of FGM alone is also seen in the specimens in microscopic observations. In the as-processed specimens the pores that were observed in group C are not observed in the corresponding coarse grain side of group A. Instead the pores are observed in the interface. This further confirms the interpretation of reheating experienced in group A specimens. The pores that were scattered all over in group C accumulated in the interface in the group A by the repetitive heating. The small pores are interpreted to have diffused through the newly solidified material to reach the interface and blocked by the fine grain side of the material that has considerably lower temperature levels leading to less diffusion. Further in the HIP+H/T

specimens the effect of FGM is observed in the difference in appearance of carbides. They were observed in the graded specimens but were seen in very low quantities in the corresponding ungraded specimens when viewed under similar resolution. This is interpreted as a difference of the size of the phases as carbides were detected in the XRD analysis of the HIP+H/T ungraded specimens indicating that they are indeed present in these specimens. Therefore, it can be reasoned that they were not observed as distinctly spread everywhere in the ungraded specimens because of their small sizes. While the carbides were larger in size in the graded specimens due to the processing that led to reheating, as before, resulting in their growth.

6-2 Research Question 2 : Effect of post process heat treatments on microstructure

The effect of heat treatment has been already covered in the previous project [13] and in Chapter 2. The results in the current project reaffirm the previous observations and interpretations. The grains were observed to transform from dendrites to columnar and equi-axed grains. This was explained by grain growth and partial recrystallization which are reported to occur at the temperature ranges achieved in the HIP and heat treatment steps ([104, 13]). However, carbides that grow at the grain boundaries as a result of the heat treatment impede their growth and recrystallization. This is the reason that there is still difference in the grain sizes on both sides of the graded specimens even after the heat treatment. Further the HIP+H/T specimen had significantly higher hardness than AP specimens. This was attributed to the precipitation of the metastable strengthening phases γ'/γ'' with the heat treatment that lead to toughening of the microstructure through various mechanisms (mentioned in Chapter 2). These phases were also detected in the XRD analysis.

The effect of heat treatment was also observed in the residual stress measurements. The stresses were seen to be more compressive in the heat treated specimens. This was explained previously by the increase in strains in the microstructure resulting from the precipitation of the strengthening phases (γ'/γ'' phases) and the carbides. As the HIP step is expected to serve as a stress relief step it is reasonable to expect a stress decrease after heat treatment. Therefore, this opposite trend is explained by the appearance of the aforementioned precipitates in the following aging step which resulted in higher compressive stresses. In that case, the strengthening phases strain the inside of grains due to their misfit within the grains whereas carbides are expected to have resulted in pinning of the grain boundaries thereby resulting in compressive forces during grain coarsening. The increase in compressive stresses is also reported in other works [105, 106] however the reasons mentioned in the current study were not covered in these works.

6-3 Research Question 3 : Effect of microstructural features on fatigue

The results summarized in Chapter 5 showed that specimens which had different microstructures also had different fatigue parameters. Microstructural features (grain size and grain

orientation) discussed above were also found to affect the fatigue behavior. In addition to that, gaps corresponding to the discussion in the previous chapter are also addressed here.

6-3-1 Effect of grain size and grain orientation on fatigue

The effect of grain size was reported in both batches. This effect is seen in the specimens along with grain orientation as it is generally observed that with a particular orientation (group C with grains oriented along length) the grains are more coarse than the other orientation (group D with grains oriented along width). Moreover group D (coarse grain) and group E (fine grain) are seen to have similar fatigue behavior. Therefore, both the effect of grain size and orientation are discussed together. The trend of fatigue behavior in different grain sizes was observed to be opposite to the general trend. This general trend is based on various micromechanical models involving different phenomena. One such model describes the effect of grain size to manifest in terms of the level of roughness induced crack closure [107]. It is a known fact that at near threshold stress intensities, the crack grows through slip bands and therefore, leads to a zig-zag crack growth. This leads to higher roughness, higher crack closure and therefore, lower ΔK_{eff} at the crack tip in coarse grains as compared to the fine grains. Therefore, a higher ΔK_{th} is needed to propagate the cracks in the coarse grain microstructure. This is also confirmed for Ni-based super alloys [108]. In the current project the opposite trend was observed which was linked to the presence of compressive residual stresses. The linking of such heat induced stresses could result in many problems. Specially this is not confirmed in the current analysis that the stresses are mainly compressive throughout the thickness of the tested specimens. However, assuming that it is true, the effect of compressive stresses can be expected to result in decreasing the ΔK_{eff} at the crack tip. These stresses were observed to be higher in the fine grain material. On the other hand, as mentioned before, roughness induced crack closure, which also reduces the ΔK_{eff} , is higher in coarse grain. Therefore, it is a matter of which effect is higher in the materials in the current project. As seen from the results in AP batch, the effect of residual stresses are dominating in these specimens leading to such a trend. Whereas, in the HIP+H/T batch, both phenomena are observed to occur as trends found between group C and D are explained by the former and that found between group D and E are explained by the latter. However, as mentioned in the previous section, the results about residual stresses need to be confirmed with more analyses (for example, through thickness measurements of residual stress). Additionally, the behavior of specimen AP-C could be linked to presence of pores which needs to be confirmed with further microscopy. Shown below are the images of the crack path in AP-C (Figure 6-1).

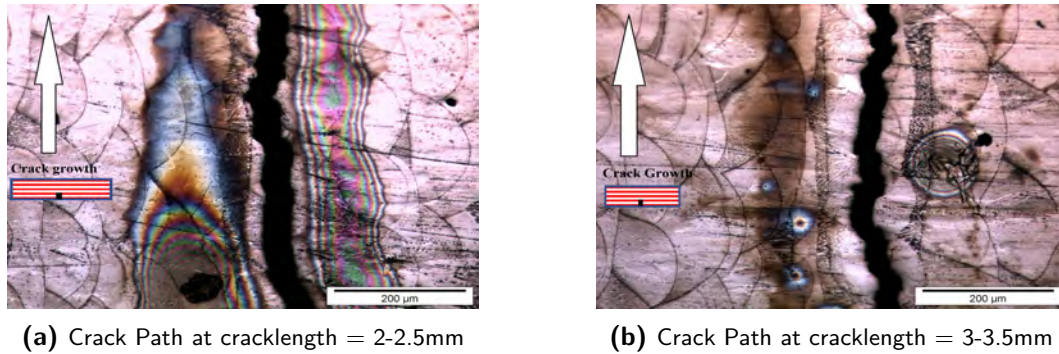


Figure 6-1: Etched crack path in specimen AP-C. Pores can be found in b).

From the images it can be seen that, although, pores are visible around the crack path, it is difficult to conclude if pores helped in the propagation of crack. This could be further verified using fractographic analyses.

The effect of grain orientation was seen in the difference in fatigue behavior between groups C (grains perpendicular to crack) and D (grains parallel to crack). Although, this is not solely arising out of the difference in grain orientation as from the discussion above and the results mentioned earlier in Chapter 4, the aforementioned groups are found to have different grain sizes as well. Therefore, the different behavior in group C as compared to group D can't be attributed to any one of the factors. Even more interesting is the similarity of fatigue curves found in group C and H/T wrought material. Although, the latter is discussed later, the piecewise linear fatigue curve raises many new questions. Various works have shown that at low ΔK values in this and other Ni based superalloys the fracture surface shows flat facets indicating a stage I like cracking mechanism [108]. In other words, the cracking occurs by shearing along the slip direction. Whereas at high ΔK , the mechanism transforms to a plastic blunting mechanism leading to the formation of striation. This was also covered in Chapter 2 where different mechanisms were reported to occur which are not locally additive and depending on the ΔK level changes from one dominating mechanism to other. The piece-wise linear trend was attributed to a change in the mechanisms. These mechanisms give rise to specific crack path features which are already reported in literature. To confirm this, further microscopy is done on the crack path to relate to these features. The images are as shown below.

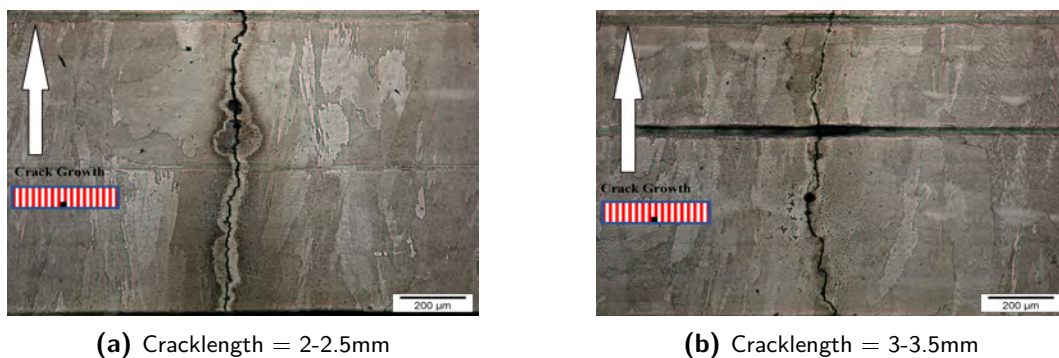


Figure 6-2: Etched crack path in specimen AP-D.

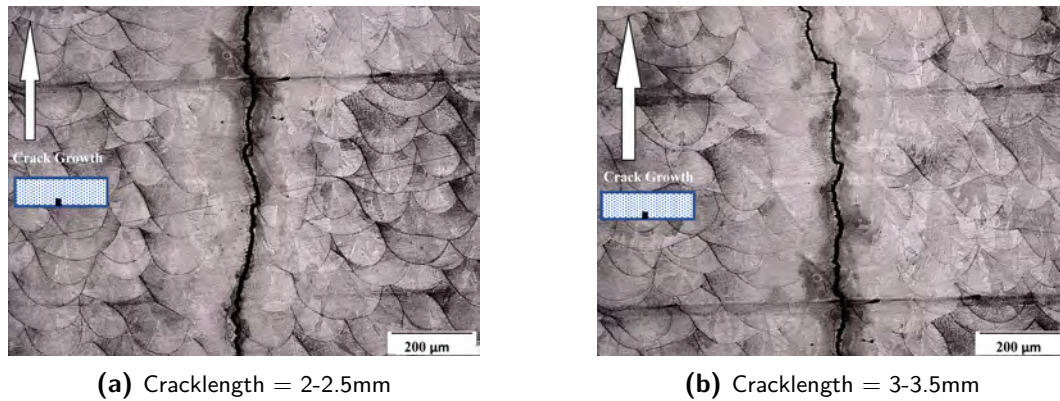


Figure 6-3: Etched crack path in specimen AP-E.

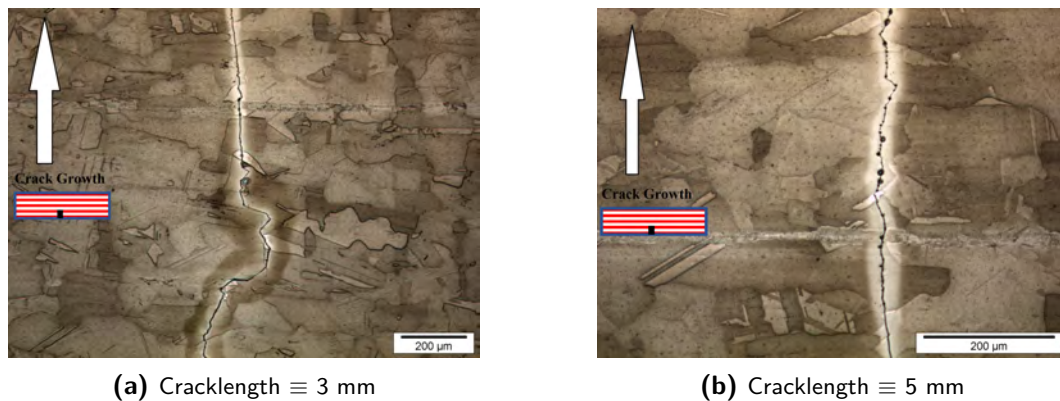
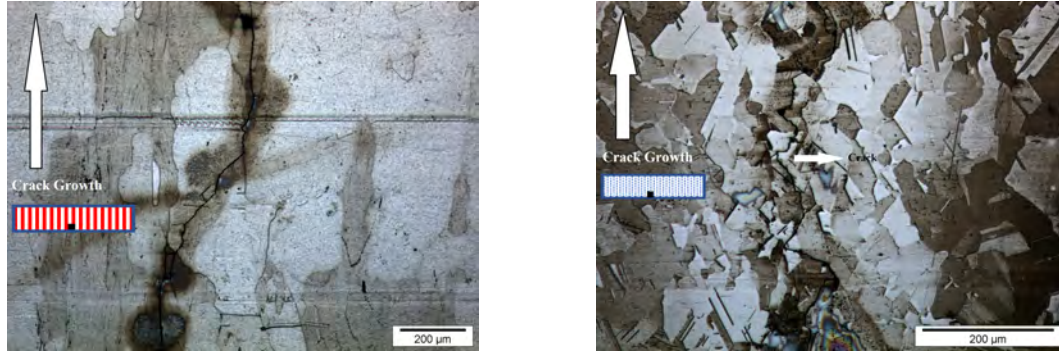


Figure 6-4: Etched crack path in specimen HIP+H/T-C.

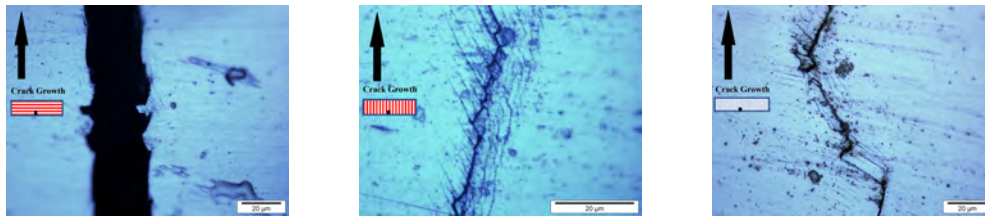
From Figure 6-4, it is observed that the crack is tortuous and changes to a more straight path at a certain cracklength. Further such features are not observed in the other figures. In Figure 6-4, it is tempting to relate the former to an intergranular type of crack growth and the latter to a plastic blunting mechanism at first instance. This point of change is found to be at the same corresponding crack length as that seen from the fatigue curves. Also in Figure 6-5, the crack is seen to be crossing the grains in a transgranular manner. Therefore, it was suspected that the crack growth is completely transgranular in D and E (fine grain) specimens whereas it starts with an intergranular type in C and changes to a transgranular type growth later. This is very unlikely as in literature the fatigue mechanism for IN718 is reported to have a transgranular crack growth over the entire Paris range of ΔK at room temperature (section 2-4). Moreover, this trend is not observed in the as-processed batch (refer Figure 6-1, Figure 6-2, Figure 6-3). Further, slip planes denoting a plastic blunting mechanism are reported in all the groups in the as-processed batch (refer Figure 6-6). Therefore, it is not confirmed if the different mechanisms particularly that mentioned above are responsible for the different behavior in group C.

It is noteworthy that in many other works the fatigue curves of the H/T-wrought material is found to be single linear curves [64, 67]. One such work reports a mix of the two mechanisms above thereby resulting in a single linear curve [67]. This could be the case in group D and group E because of which a single curve is observed. It could be argued that the different



(a) Cracklength \equiv 5 mm in HIP+H/T-D specimen (b) Cracklength \equiv 5 mm in HIP+H/T-E specimen

Figure 6-5: Etched crack path in HIP+H/T specimen. Sightings of the crack crossing grains.



(a) AP-C- cracklength = 4 mm (b) AP-D- cracklength = 5.5 mm (c) AP-E- cracklength = 5 mm

Figure 6-6: Unetched crack path in AP specimen showing slip planes.

behavior in group C arises out of the significantly coarser grains as compared to group D and E but this is in conflict with H/T wrought material where fine grains were found as seen from Figure 4-29 and Table 4-4. Therefore the exact factor that decides which behavior (single linear or piece-wise linear) will occur remains unclear at this point.

In final words, it is very likely that the origin of piecewise linear curves is arising out of different mechanisms. That the different mechanisms resulting in this behavior of group C are same as the mechanisms resulting in a similar type of behavior in H/T wrought materials also needs to be confirmed. Analyses like fractography and EBSD of the crack path are expected to provide further directions.

6-3-2 Effect of Heat treatment

The effect of heat treatment on the fatigue behavior was relatively straightforward as compared to the previous subsection. The precipitation of strengthening phases after heat treatment lead to blocking of dislocation pile ups thereby increasing the resistance of the microstructure to crack propagation [101]. It is tempting to relate the better fatigue behavior to the coarsening of grains upon heat treatment. However, this would not explain the opposite trend observed among the groups. Similarly, the effect of pores was not linked with the fatigue behavior in the AP specimens because of their small size. However, the disappearance of pores and other detrimental phases like laves and δ phase also removes the weak links from the microstructure.

6-4 Research Question 4 : Comparison of 3D printed and wrought Inconel 718

The discussion of the effect of 3D printing is useful to assess the performance of the material used in the current study on a practical bench mark. Therefore, a comparison is made between HIP+H/T specimens which is expected to be practically relevant and H/T wrought specimens which are currently use in real life applications. From results obtained before, it was seen that only at high ΔK values these specimens behave similarly. However, at the low ΔK level where it is expected to be more practically relevant, none of the specimens are better than the latter. It is surprising that the specimen that outperformed wrought material was as-processed fine grain material AP-E. Being as-processed it was expected that processing related shortcomings would affect the fatigue performance. However, as reported above, the exceptional behavior was attributed to high residual stresses in the microstructure. It would be risky to conclude that AP-E microstructure is of practical importance as the evolution of residual stresses is still needs to be investigated further at this point. Therefore, it may be the case that the high compressive residual stresses in AP-E were specially dependent on the dimension of specimens used in the current study. This needs to be confirmed with more replicate tests and residual stress analysis. On the other hand improvements in the HIP+H/T specimens needs better understanding of the factors that decide the fatigue behavior in the wrought specimens. For example, the discussion above on the effect of grain orientation shows that there are many gaps that needs to be investigated.

6-5 Research Question 5 : Effect of FGM on fatigue crack propagation

The effect of FGM in the results has been seen to produce interesting results. The test conducted to investigate this was a constant ΔK test which required accurate estimation of ΔK in the changing microstructure. A FEM model was utilized to calculate the new formulas for the specimens. This in turn required accurate estimation of young's modulus. Hence, it can be imagined that the test procedure was an extremely sensitive method where small errors in accuracy could result in big deflections in the final curves reported in this study. However, in many curves it is seen that at the beginning of the curves (i.e. at small crack ratios) where the microstructure is relatively homogeneous, the crack growth was more or less constant. This indicates that the level of ΔK was maintained at a constant level implying success of the procedure. Additionally the curves also included DIC which interfered in the accurate measurement of crack lengths whose effect was seen in the specimens in terms of higher scatter (refer figures in appendix G). The scatter implies that the procedure was not anymore a constant ΔK test. Therefore, this raises the question on the reliability of tests where DIC was used. Anyhow, most curves are reported to be fairly linear in the beginning as before. Therefore, it is assumed that the tests were successful in all of the tests but one.

The expected effect of graded microstructure was a decrease in crack growth as the grain size increased. However, as indicated by the results in this study, the crack growth rate increases as the size of grains increase in the same trend as observed in the ungraded specimens. In

most specimens, however, even the increase in the crack growth rate remained within a narrow band of values indicating very less difference in da/dn which meant that the coarsening of grains on both the sides diminished the difference. Further, in the as-processed specimens the effect of building direction was seen in the difference in the change in crack growth rates across the width of the specimens. Specimens where the grains were oriented along the width (AP-B), the crack growth was seen to undergo higher change as compared to specimens where the grains were along the length (AP-A) having more or less the same crack growth indicating more homogeneous microstructure in the latter as mentioned in research question 1. Moreover the crack growth in most specimens was higher than the corresponding da/dn at the same ΔK seen in the ungraded specimens. This increase of da/dn , as compared to the ungraded specimens which was also explained using the concept of grain coarsening raises further questions. Taking the ungraded specimens as reference where coarser grains had higher da/dn for a given ΔK , the increase of da/dn with grain coarsening in the graded specimens makes sense. But the trends in the former were explained in terms of lower compressive residual stresses in the coarse grains and when the same is used here, it doesn't explain the trend as the residual stresses are not observed to strictly decrease in these specimens as compared to the former. It is intuitive to expect that the residual stresses should decrease in the graded specimens due to the reheating experienced during the processing, but the results don't confirm the same trend. It is possible that the residual stress measurements may not be completely accurate as it is subject to the goodness of specimen preparation. Similarly, the decreased da/dn in AP-B (graded specimen built along the width) specimens as compared to their corresponding ungraded specimens is even more surprising. If the concept of grain coarsening is applied here, it doesn't match the previous results where coarse grains are linked with higher da/dn . Additionally, the compressive residual stresses in these specimens were also lower than the corresponding ungraded specimens. It is possible that the small amount of grain coarsening could have led to a toughening effect leading to a lower da/dn . As mentioned above, grain coarsening leads to higher roughness induced crack closure leading to less ΔK_{eff} and thus lower da/dn . Certainly, this indicates that a very sensitive balance between the general strengthening effect of coarser grains and the weakening effect of lower compressive residual stresses is at play in these specimens.

In addition to the above results, effects of the interface and the post process heat treatments were also covered in the summary presented in the previous chapter. The crack growth in the interface in all of the graded specimens increased which was attributed to the gradient microstructure while the effect of post process heat treatments was seen to diminish the effect of building direction mentioned above.

An important expectation from graded microstructure used in the current study was the effect of texture in the specimens. This was specially expected for as-processed batch where the coarse grain side was designed to have texture. Any effect should have been seen in the interface region. Although, in both the as-processed specimens there is an increase of da/dn in the interface, it cannot be individually linked to the effect of texture because of presence of other features like pores and voids. Similarly, the crack curving in specimen AP-B at the interface also could not be linked to an effect of texture as the crack was found to be asymmetrical which could have resulted in this behavior. The texture in the specimens was expected to have $\langle 100 \rangle$ direction parallel to building direction as reported in the literature (subsection 2-2-3). If the primary slip bands in the specimens are aligned in the maximum shear direction (45° to the crack), the crack growth rate is expected to be higher. Therefore, favorable texture leads to higher da/dn . Similarly, if the texture is such that the primary slip directions are not

activated, the da/dn will be slower. This is an important direction that needs to be explored with FGM of differently oriented grains.

In concluding remarks, the results above provides evidence that the FGM leads to distinguishable modification in da/dn across the width of the specimens. Important relations between the microstructural features like the grain size, grain orientation, residual stresses, etc. and their effect on the crack growth behavior were also covered here. This provides further directions to be explored to better explain the behavior in this specimens and to design better FGM material.

Chapter 7

Conclusions

The main conclusions from this study are summarized in the following sections in terms of the research questions (RQ) defined in chapter 2:

7-1 RQ 1 : How does the individual microstructure and mechanical properties develop during 3D- printing of Inconel 718

1. Microstructural features observed in as-processed material as well as hardness and Young's modulus were found to be dependent on 3D- printing process and in good agreement with the literature. Namely, coarse grain materials showed grains elongated along building direction with preferred $\langle 100 \rangle$ texture, while fine grain material showed equiaxed grain structure. Both hardness and Young's modulus were smaller for coarse grain (300 HV and 140 GPa) as compared to fine grained (370 HV and 185 GPa).
2. Group C (coarse grained material parallel to length) and Group D (coarse grained material parallel to width) showed different microstructural and mechanical behavior. Group D showed smaller grain size (93 μm) with corresponding higher hardness (340 HV), lower porosity and higher levels of residual stresses, while Group C showed grain coarsening (140 μm), attributed to better reheating during 3D-processing.
3. The residual stresses in the current specimens were found to be compressive in nature. This was reasoned to be an effect of the processing method leading to thermal gradients subsequently resulting in compressive stress in the inside and tensile on the outside.

7-2 RQ 2 : What is the effect of post process heat treatment on individual microstructure and mechanical properties

Post process heat treatment in terms of Hot Isostatic Pressing (HIP) + H/T was found to result in grain recrystallization (partial) and coarsening with distinct twins and carbides.

Hardness was found to be increased by 50-60%, while porosity and preferred texture were almost entirely eliminated. The substantial increase in compressive residual stresses following heat treatment was attributed to the straining of the grains resulting from the formation of precipitates like carbides (at the grain boundaries resulting in pinning of grains) and γ'/γ'' (in the grains resulting in misfit strains).

7-3 RQ 3 : How do the fatigue parameters obtained for ungraded Inconel 718 depend on the various microstructural features like grain size, orientation, residual stresses, etc.

1. The fatigue curve of group C (coarse grain material parallel to length) was found to follow piece-wise linear trend similar to the wrought material examined herein. This was attributed to different mechanisms at play. At lower ΔK the crack growth is estimated to follow a crystallographic growth while at higher ΔK it is estimated to follow a plastic blunting mechanism. This is not seen in group D (coarse grain material parallel to width) and group E (fine grain), which is attributed to the presence of a mix of both mechanisms. The exact reason behind the different trends should be further investigated.
2. The crack propagation behavior (ΔK_{th} and da/dn) for coarse materials was found to be worse than the fine grain material, opposite to the general trend. This was explained with the help of compressive residual stresses leading to less ΔK_{eff} in the fine grain specimens.
3. Heat Treatment (HIP+H/T) on the specimens erases differences between the fine and coarse grain materials (groups E and D). This was attributed to the grain growth in group E. It should however be noted, that the difference between two coarse grained groups exhibiting different grain orientation still remained clear. The fatigue behavior is also seen to improve for each group following the heat treatment, which is likely attributed to the appearance of strengthening phases.

7-4 RQ 4 : What is the difference between fatigue properties of 3D-printed and conventional wrought Inconel 718

With respect to the wrought material (with grain size of 10 μm), the 3D-printed material with fine grains (70 μm) showed higher ΔK_{th} and lower da/dn values. The better performance was attributed to high compressive residual stresses. The fatigue behavior for coarse grained materials was on the same level as the wrought material, only following HIP+H/T specimens, at high ΔK levels.

7-5 RQ 5 : Based on the results of this study and literature can the developed herein relations be used to tailor fatigue behavior in 3D-printed functionally graded materials

This RQ is directly related to the main objective of this study, which was to

Investigate if the functionally graded microstructure can be used to affect the fatigue behavior of 3D-printed Inconel 718

It was seen in the discussions that the graded material (FGM) has a significant effect on the fatigue crack propagation. The fatigue crack growth rate (da/dn) is seen to be increased according to different microstructure similar to trends observed in the ungraded specimens, indicating that the heterogeneous microstructure of the material is reflected in the fatigue crack growth rate. Thus 3D-printing process can be used to design microstructural gradient and alter fatigue behavior of complete 3D structures. Summarized below are the effects of different parameters on the fatigue behavior of the FGM:

- **Building direction and grain orientation** were found to have significant effect. For as-processed specimens, the crack growth rate is seen to be affected by the building direction as well, similar to that observed in the results of microstructural characterization. The da/dn was found to continuously change in group B (building direction along the width) specimens contrary to only a change in the interface in group A (building direction along the length). This reaffirms that the heterogeneity in graded material is only conserved when the building direction is along the width.
- **Interface region** also gives a significant effect. The interface region is also found to have a distinguishable effect in both the groups of as-processed specimens having different building direction. The da/dn is found to increase with the changing microstructure in this region as per trends in the ungraded specimen. Additionally, in group A (building direction along the length), where the microstructure was reported to be almost homogeneous, the increase in da/dn was linked to the effect of pores. This indicates that with a suitable design that still maintains the heterogeneity in the microstructure, an interface can be produced that results in the opposite trend.
- **Grain sizes and Residual stresses** : In the as-processed group B (building direction along the width) specimens, the fatigue crack growth rate (da/dn) was lower than the corresponding da/dn in ungraded specimens. This was unlike the other specimen (group A with building direction along the length) where the da/dn was more than their corresponding ungraded microstructure. It was estimated that the reheating of specimens experienced while processing leads to both the coarsening of grains and the reduction of residual stresses. The former was then explained with the effect of coarser grains that leads to a toughening of the microstructure (and thus lower da/dn) which dominates over the effect of lower compressive residual stresses. While in the latter, the effect of lower compressive stresses seemed to have dominated. A sensitive balance of the effect of grain size related strengthening and residual stress related effects are estimated to determine the final behavior. This indicates that residual stresses also play a major role in graded specimens like in ungraded specimens which subsequently

suggests that further study on the evolution of residual stresses in relation to grain sizes are needed for the complete understanding.

- Finally, post process heat treatment is also found to give a very profound effect. In the HIP+H/T specimens, the fatigue crack growth rate was found to be higher than the corresponding da/dn in ungraded specimens. Additionally, the difference between the two differently built graded material also diminished after the heat treatment. Therefore the post process heat treatment should be further optimized to meet the needs of functionally graded material (thus not erasing the intended microstructural grading/build up).

Future Recommendation

The current study raised many new questions and many new directions have been mentioned in the discussions. To answer the questions raised by this study, the following steps are suggested for further research:

1. Residual stress study in the specimens - In the current project, residual stresses are seen to be a major factor in fatigue behavior. To better explain, the evolution of residual stresses needs to be understood better. The study should be so designed that the residual stresses are linked with product geometry so that the relation between stresses and position in the bulk is established.
2. Temperature profile simulation - In the current project, differences in grain size and residual stresses depending on the grain orientation is surprising. To further explain this, Finite Element Modelling (FEM) simulation of temperature profile inside the bulk can be performed. This could also be linked to the above study to better explain residual stress evolution with temperature.
3. Fractography and EBSD - In the current project, the results from fatigue crack growth tests could not be conclusively related to mechanisms seen in literature. This needs to be linked with the help of fractography. Further, it was suspected that the reason of piece-wise linear trend in the fatigue curves could be arising out of intergranular crack growth in the beginning. Although, unlikely, this could be verified with the help of EBSD in the crack path. Moreover, EBSD from HIP+H/T specimens would also verify the texture evolution and the trends of grain sizes mentioned above.

Further, new directions are also hypothesized as per the experience gained from this project. They are as follows:

1. Tests at Lower ΔK - The same tests could be performed on the same specimens at lower ΔK as it is more practically relevant. Moreover, the differences in da/dn at low ΔK is found to be more than that at higher ΔK . Therefore, it is expected that crack deceleration is more likely to happen at lower ΔK .

2. Tests on H/T material - The heat treated specimens in this project were HIP+H/T. In literature (chapter 2) it has been established that with a prior HIP step, the microstructure is found to be significantly different than the H/T specimens. For example, δ phases are found to be present at the grain boundaries instead of carbides. Therefore, it is interesting to investigate this material under the same tests.
3. Interface at different angles - In the discussion it was reported that the crack growth may slow down depending on the active slip planes. The active slip directions depended on the orientation of the crack with respect to the grain orientation. Therefore, it can be imagined that crack growth could have slowed down at the interface if the active slip directions in this region had higher critical stresses than the fine grain side. Subsequently, it could be hypothesized that instead of the interface being perpendicular to the crack, it could be oriented at a suitable angle to affect the crack growth.
4. Specimens with different grain orientations instead of grain size - In this project it is seen that there is significant difference between the grain orientations itself. Therefore, investigating specimens with two layers of the differently oriented grain could also be useful. Further, this could be linked with the above recommendation as both the grain orientations are found to be highly textured material.
5. Specimens with multiple interfaces - It was seen that the da/dn increased at the interface as the crack grew from the fine grain side to the coarse grain side. Therefore including another interface using the opposite combination may result in a decrease in the da/dn . For example, after the fine grain side the SLM parameters can be altered twice to get one interface having fine-coarse transition, then coarse-fine and again fine-coarse transition. This may help in two ways; one, it may reduce the effect of residual stresses as more reheating is involved here therefore the effect of grain size would help in better modification of da/dn ; second, if it doesn't reduce the effect of the residual stresses and stays the same, then in the opposite interface the trend in da/dn could be expected to be opposite to that observed in the current project.

Appendix A

Chart showing the methodology

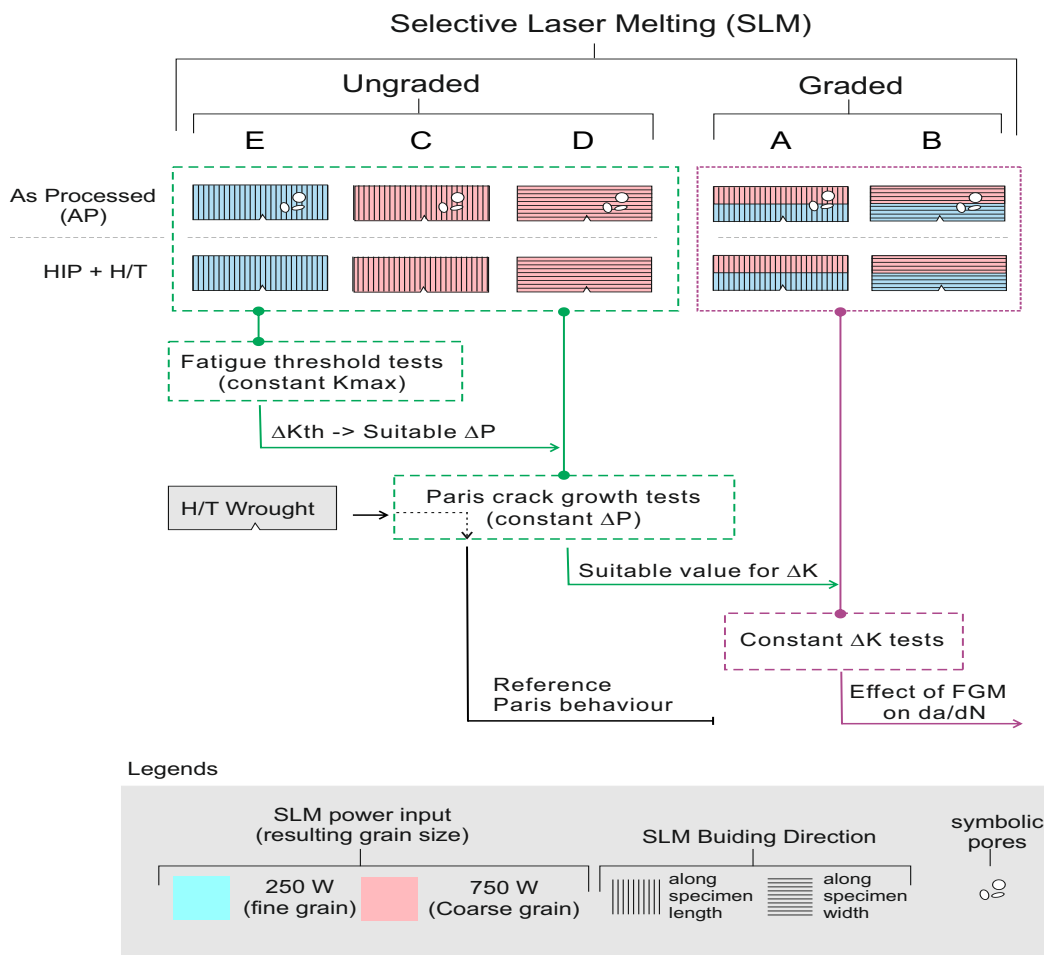


Figure A-1: Flowchart of the methodology adopted in this project

Appendix B

XRD setup and example of data analysis

The set up of the specimens in the XRD is shown below.

Instrument: Bruker D8 Discover with Eulerian cradle in parallel beam geometry.

Incident beam side: polycapillary optics divergence 0.25° ;

beam size: 4h 4b mm.

Diffracted beam side: parallel sollerslit divergence 0.35° ;

graphite monochromator.

CoK α radiation, 45 kV 25 mA.

Stress measurement: reflection 311 around $111^\circ 2\theta$.

Sin 2ψ range 0 - 0.6 in steps of 0.2.

Time per step 7s.

Data evaluation: Bruker software Diffrac.EVA vs 5.0. and Panalytical X-Pert stress.

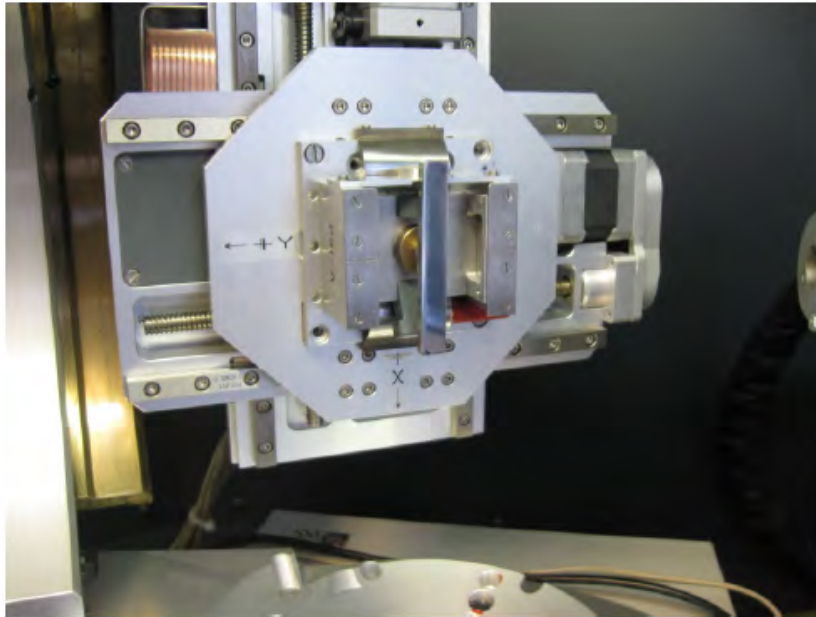
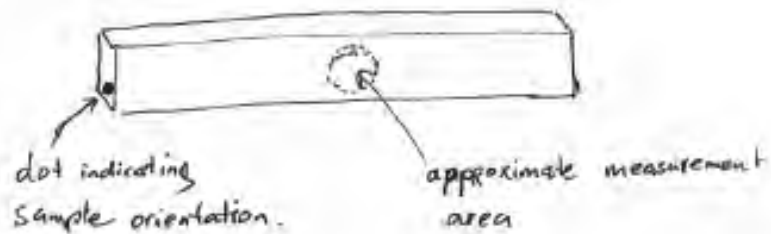


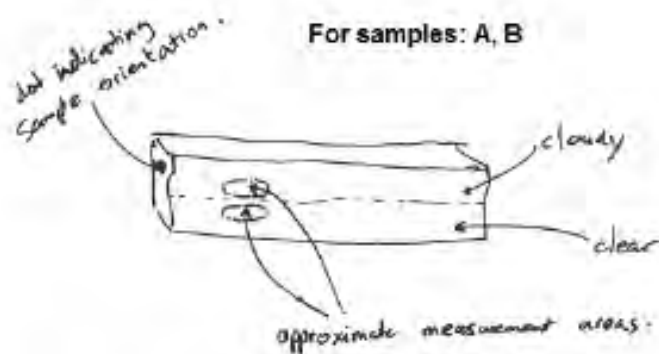
Figure B-1: Arrangement of the specimen in the machine

Schematic of stress directions and sample orientation

For samples: C, D, E



For samples: A, B



Building direction:

A, C: along length

B, D: along width

E: n.a.

Note: "Cloudy" and "clear" in the schematic refer to the 950W and 250W zones in the graded samples respectively. The terminology was chosen as per their appearance after etching and was done to avoid confusion in reporting.

Figure B-2: Schematic describing measurement positions in the specimens

An example of the raw data analysis is shown.

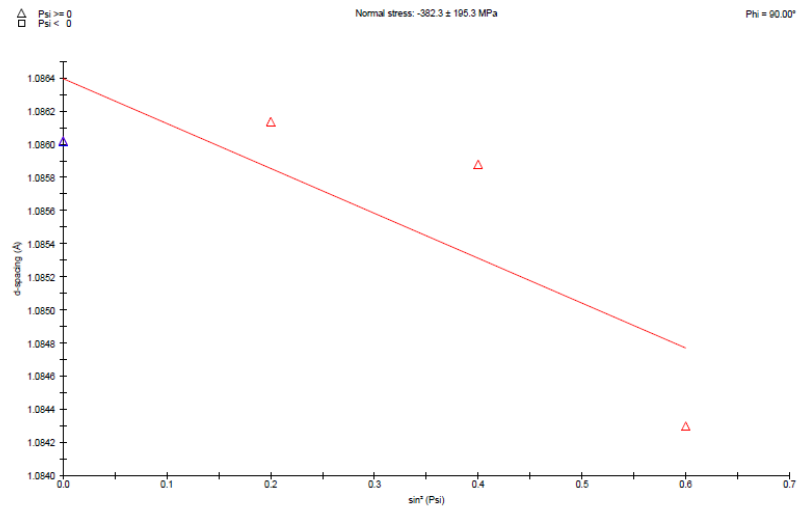
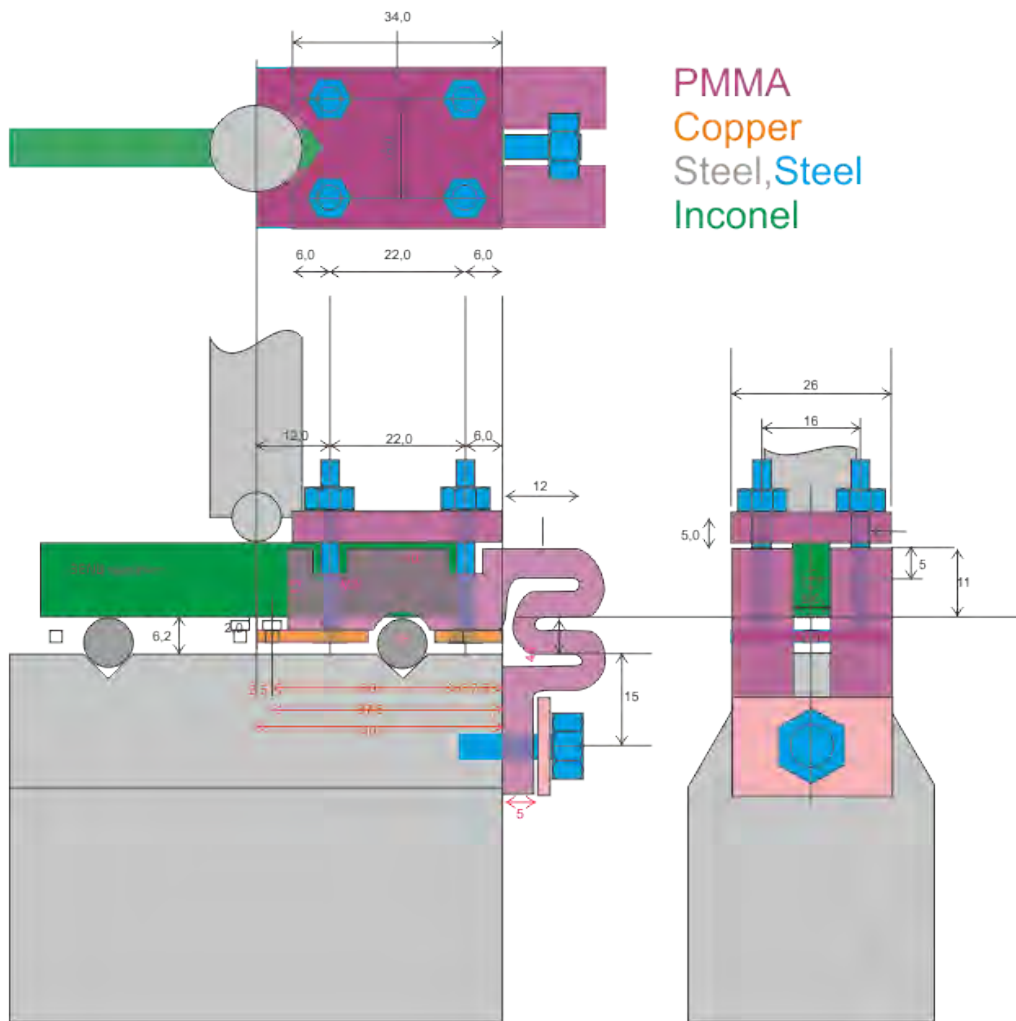


Figure B-3: d v/s $\sin^2(\psi)$ example showing curvy variation. This was attributed to either a presence of shear stress or a stress gradient along the depth.

Appendix C

Clamp drawing, setup summary

C-1 Clamp



In the figure below, the preparation of the specimens is shown.

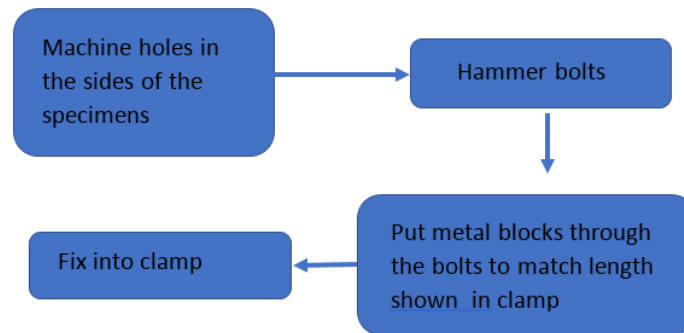


Figure C-2: Chart showing the preparation of chart after machining to final dimensions and notching.

C-2 Set-up

The set-up is shown in the chart below.

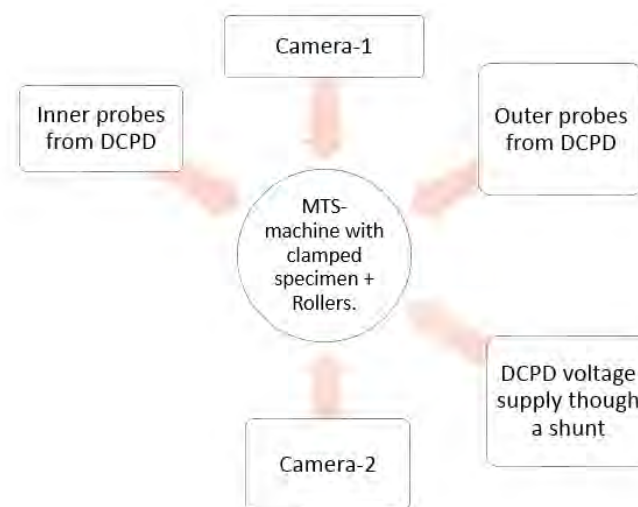


Figure C-3: Chart showing the setup

Additional note:

1. The specimens were insulated from platform by using small layers of GLARE at the contact points of specimen and the rollers.
2. The voltage from the DCPD was too high to be measured by it. Therefore it was stepped down by using a shunt in parallel. The block and red wires shown in the Figure 3-2 are from the shunt.

Appendix D

Young's modulus results from indentation method

The results are summarized below.

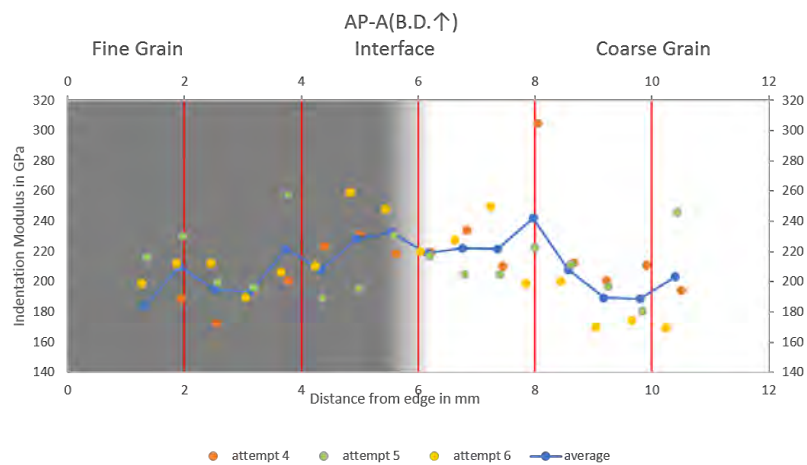


Figure D-1: Indentation test results for specimen AP-A

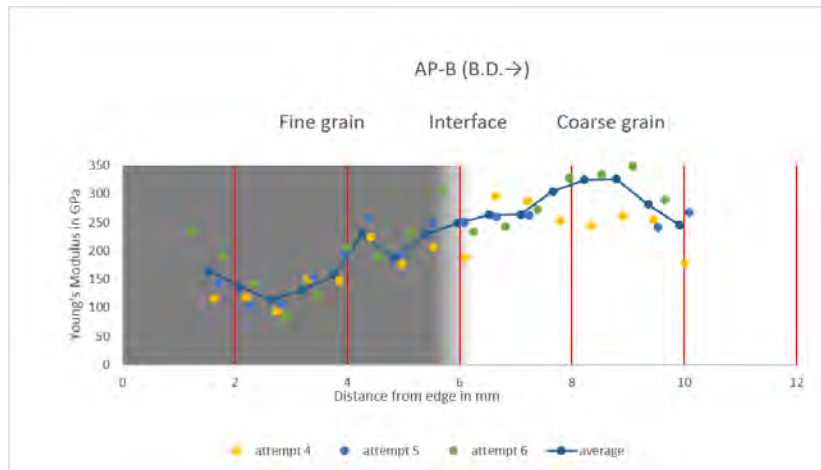


Figure D-2: Indentation test results for specimen AP-B

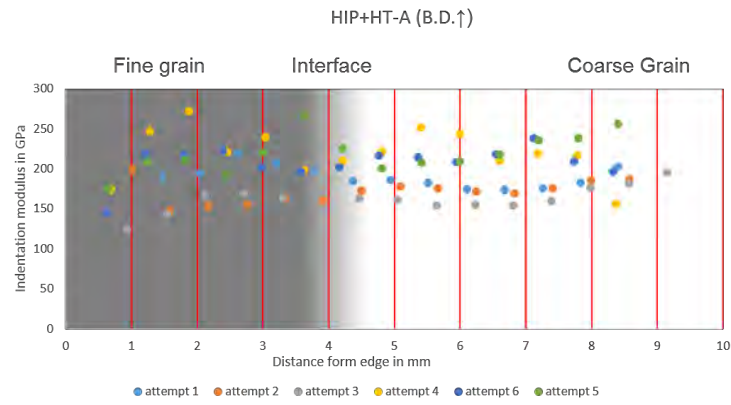


Figure D-3: Indentation test results for specimen HIP+H/T-A

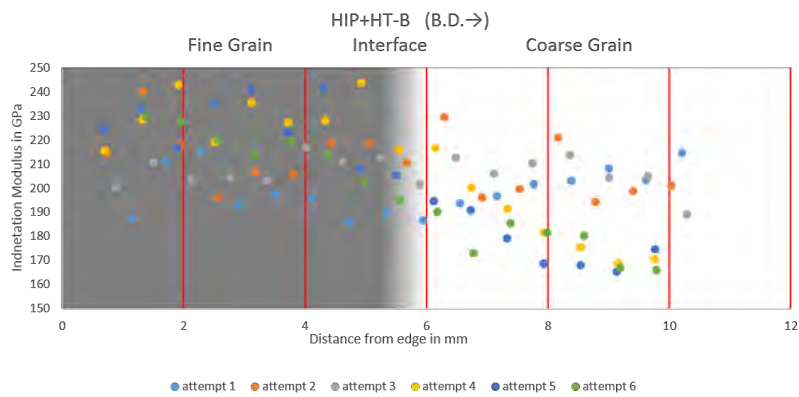


Figure D-4: Indentation test results for specimen HIP+H/T-B

Appendix E

Algorithm for reduction of MTS data

The MTS data was reduced in steps to obtain the ΔK and da/dn data points. The MTS data is as shown below.

Table E-1: Sample of raw MTS data

Force	Segment	Cracklength
-658.995	134884	2.711012
-66.6717	134885	2.708845
-658.053	134886	2.718237
-65.7673	134887	2.71896
-657.493	134888	2.717515
-66.6259	134889	2.71896

As seen above, the data is for every peak and valley.

E-1 Step 1

The first step is to reduce the data per cycle.

```
1 function [a,n,delP]=reducean(cracklength,cycles,force,skipvariable)%Input
   variables in order: peak valley cracklength
2 %peak valey segment(not cycle) number,peak-valley force values,a skip
3 %variable to skip data points in case of too many data points
4 [maxdata,~]=size(cracklength); %to find out the size of the input
   variables
5 %Initialize all variables to be used
6 a=zeros(100000,1);
7 tempa=zeros(100000,1);
8 tempn=zeros(100000,1);
```

```

9  n=zeros(100000,1);
10 delP=zeros(10000,1);
11 tempdelP=zeros(100000,1);
12 i=1;
13 j=1;
14
15
16
17     while j<maxdata %move along the input variables till last
18     tempdelP(i)=abs(force(j)-force(j+1)); %calculate delta P
19     tempn(i)=floor(cycles(j+1)/2); %calualte cycle number
20     tempa(i)=(cracklength(j)+cracklength(j+1))/2; %calculate average
        crack length in that cycle
21     j=j+2; %increment j by 2 as in the input file two data points will be
        transformed to one
22     i=i+1;%increment i by 1 as this is the output variable
23     end
24
25 k=1;
26 w=1;
27 [newmax,~]=size(tempdelP);%calculate size of newly formed delta P
        variable
28 while k<newmax %procedure to skip datapoints
29     delP(w)=tempdelP(k); %save temporary variable values to final output
        variables
30     n(w)=tempn(k);
31     a(w)=tempa(k);
32     k=k+skipvariable; %skip data points here
33     w=w+1;
34 end
35 delP=delP(delP~=0); %since the variables were initialized by zeros, this
        removes the remaining zeros
36 n=n(n~=0);
37 a=a(a~=0);

```

Final data after this step.

Table E-2: Sample data after step 1

Δ Force N	Cycles	Cracklength
508.38	564443	4.67
505.30	564493	4.68
511.02	564543	4.67
507.75	564593	4.68
506.60	564643	4.68
507.75	564693	4.67

E-2 Step 2

The second step is to reduce the data in such a manner so that there is equal number of data points per increment of cracklength. This is done as in the beginning due to low crack growth there are higher number of data points that leads to higher scatter in da/dn .

```

1 function [newa, newn, newdelp]=reducean_part2(a,n,delp,ablock,nr)
2 %input variables: a:reduced cracklength (ouput from reducean.m)
3                 %n: reduced cycles
4                 %delp:reduced delta P
5                 %ablock: crack increment where reduction procedure is
6                 %carried out
7                 %nr: no of reduced points in each ablock
8 [maxdata,~]=size(n);
9 newa=zeros(10000,1);
10 newn=zeros(10000,1);
11 newdelp=zeros(10000,1);
12 aa=zeros(10000,1);
13 nn=zeros(10000,1);
14
15 t=1;%new file traverse variable
16 i=1;%main file traverse variable
17 while i<maxdata %Starts main position traverse through the array
18     k=i+1;
19     for k=i+1:maxdata %starts searching for the next block size hence
20         from i+1 position
21         for j=1:k-i+1 %Takes everything from the position of main
22             control i to position of block search k (a total of k-i+1
23             elements)
24             aa(j)=a(j+i-1); %into temporary arrays of aa and nn. The main
25             position is traversed with i and j as i+j-1
26             nn(j)=n(j+i-1);
27
28         end
29         %quadratic fit procedure starts
30         c1=0.5*(nn(1)+nn(k-i+1)); %a constant made of the first and last
31         data points in the 'cycles' array
32         c2=0.5*(nn(1)-nn(k-i+1)); %another constant made of the first and
33         last data points in the 'cycles' array
34         nn_scaled=(nn-c1)/c2; %a scaled n variable
35         sx=0; %sum of linear terms
36         sx2=0; %sum of quadratic terms
37         sx3=0; % sum of cubic terms
38         sx4=0; % sum of quadruple terms
39         sy=0; % same as above
40         syx=0;
41         syx2=0;
42         for w=1:k-i+1 %finds sum for the block till now
43             sx=sx+nn_scaled(w);
44             sx2=sx2+(nn_scaled(w))^2;
45             sx3=sx3+(nn_scaled(w))^3;
46             sx4=sx4+(nn_scaled(w))^4;

```

```

41     sy=sy+aa(w);
42     syx=syx+aa(w)*nn_scaled(w);
43     syx2=syx2+aa(w)*(nn_scaled(w))^2;
44     end
45     %least square terms in following lines
46     term1=(sx2*sx4-sx3^2);
47     term2=(sx*sx4-sx2*sx3);
48     term3=(sx*sx3-sx2^2);
49     denom=7*term1-sx*term2+sx2*term3;
50     numer2=sy*term1-syx*term2+syx2*term3;
51     bb(1)=numer2/denom; %first parameter
52
53     term4=syx*sx4-syx2*sx3;
54     term5=sy*sx4-syx2*sx2;
55     term6=sy*sx3-syx*sx2;
56     numer3=7*term4-sx*term5+sx2*term6;
57     bb(2)=numer3/denom; %second parameter
58
59     term7=sx2*syx2-sx3*syx;
60     term8=sx*syx2-sx3*sy;
61     term9=sx*syx-sx2*sy;
62     numer4=7*term7-sx*term8+sx2*term9;
63     bb(3)=numer4/denom; %third parameter
64     %quadratic fit procedure ends
65     %quadratic fit with the three parameters and scaled n variable
66     ai_fit=bb(1)+bb(2)*nn_scaled(1)+bb(3)*nn_scaled(1)^2; %cracklength a
        according to fit at the begining of the block
67     af_fit=bb(1)+bb(2)*nn_scaled(k-i+1)+bb(3)*nn_scaled(k-i+1)^2; %crack
        length at the end of block
68     deltaa=af_fit-ai_fit; %crack growth according to fit
69     if(deltaa<=ablock)%checking if crack growth is under the size
        mentioned
70         continue %if crack growth is still under size continue with next
            iteration of k (block position, refer to line 10)
71     else
72         break %if crack growth is more then break the iteration and come
            out of the loop.
73     end
74     end %end of block position search
75     %at this instance block size has been determined by the if statement
        as
76     %it stops at that k where crack growth exceeded that block size
77     blocksize=k-i; % i is still at that position in the main traverse and
        k has moved according to the condition
78     if blocksize>=nr
79         rf=round(blocksize/nr); % for every rf number of data points
            there will be one data point. nr is the number of data points
            per block
80     else
81         rf=blocksize;
82     end
83     %start of reduction procedure
84     block_pos=1; %block position set again

```

```

85     b=i; %b is a variable for travelling through the block again
86     while b<k-1 %Travelling through the block. k-1 is the last position
      of the block in the main file
87         suma=0; %sum for average of a
88         sumn=0; %sum for average of n
89         sumdelp=0;
90         no_of_elements=0; %a variable to actual calculate no of elements
      actually averaged into one element
91         for f=0:rf-1 % takes every rf number of elements
92             if(block_pos<blocksize) %checks if the local block postion is
      under the block size
93                 suma=suma+a(b+f); %then takes into the sum of a. The position
      of the block elemenets on the main file is i=b+f
94                 sumn=sumn+n(b+f); %then takes into the sum of n.
95                 sumdelp=sumdelp+delp(b+f);
96                 block_pos=block_pos+1; %incrementing block position
97                 no_of_elements=no_of_elements+1; %caluculates the no of
      elements actually averaged to one element. In most cases
      it should be equal to rf
98                 %but in the end of a block this is not rf.
99                 else
100                     break %breaks the loop when block position exceeds
      blocksize
101                 end
102             end %end of summation
103             newa(t)=suma/no_of_elements; %new data point is the average of
      the rf elements.
104             newn(t)=round(sumn/no_of_elements); %same as above
105             newdelp(t)=sumdelp/no_of_elements;
106             t=t+1; %increment new file position
107             b=b+rf; %block position has to skip to the next rf elements
108         end %end of block
109         i=i+blocksize; %increment main file position to start of next block
110     end %end of main position
111     newa=newa(newa~=0); %update newfile to exclude zeros as bydefault this
      file was initialized with zeros.
112     newn=newn(newn~=0); %same as above.
113     newdelp=newdelp(newdelp~=0);

```

Final data after this step.

Table E-3: Sample data after step 2 reduction

Δ Force N	Cycles	Cracklength
607.10	1126	2.99
636.41	3426	2.99
636.70	5726	3.00
636.62	8026	3.01
636.52	10326	3.02
636.53	12626	3.02

E-3 Step 3

The third step and the final step is to use the previously reduced data to achieve the final da/dn v/s ΔK data.

```

1  function [dadn,delK]=dadnmaker(cracklength,n,delp,W,B)
2  %input variables: cracklength: cracklength after reducean_part2
3                    %n: cycles after reducean_part2
4                    %delp: delta P as above
5                    %W:actual width of the specimen
6                    %B:thickness of the specimen
7  %The procedure is taken from ASTM-E647 please refer to it. This exact
8  %algorithm is present in the standard as well.
9  [maxdata,~]=size(n);
10
11  dadn=zeros(maxdata,1);
12  delK=zeros(maxdata,1);
13  bb=zeros(3,1);
14  aa=zeros(10,1);
15  nn=zeros(10,1);
16  i=1;
17  j=1;
18  k=0;
19
20  for i=1:maxdata-6
21      l=0;
22      k=k+1;
23      k1=k+6;
24      for lindex=k:k1
25          l=l+1;
26          aa(l)=cracklength(lindex);
27          nn(l)=n(lindex);
28      end
29      c1=0.5*(nn(1)+nn(7));
30      c2=0.5*(nn(7)-nn(1));
31      nn_scaled=(nn-c1)/c2;
32      sx=0;
33      sx2=0;
34      sx3=0;
35      sx4=0;
36      sy=0;
37      syx=0;
38      syx2=0;
39      for w=1:7
40          sx=sx+nn_scaled(w);
41          sx2=sx2+(nn_scaled(w))^2;
42          sx3=sx3+(nn_scaled(w))^3;
43          sx4=sx4+(nn_scaled(w))^4;
44          sy=sy+aa(w);
45          syx=syx+aa(w)*nn_scaled(w);
46          syx2=syx2+aa(w)*(nn_scaled(w))^2;
47      end
48      term1=(sx2*sx4-sx3^2);

```

```

49     term2=(sx*sx4-sx2*sx3);
50     term3=(sx*sx3-sx2^2);
51     denom=7*term1-sx*term2+sx2*term3;
52     numer2=sy*term1-syx*term2+syx2*term3;
53     bb(1)=numer2/denom;
54
55     term4=syx*sx4-syx2*sx3;
56     term5=sy*sx4-syx2*sx2;
57     term6=sy*sx3-syx*sx2;
58     numer3=7*term4-sx*term5+sx2*term6;
59     bb(2)=numer3/denom;
60
61     term7=sx2*syx2-sx3*syx;
62     term8=sx*syx2-sx3*sy;
63     term9=sx*syx-sx2*sy;
64     numer4=7*term7-sx*term8+sx2*term9;
65     bb(3)=numer4/denom;
66     dadn(i)=bb(2)/c2+2*bb(3)*nn_scaled(4)/c2;
67     aa_fit=bb(1)+bb(2)*nn_scaled(4)+bb(3)*nn_scaled(4)^2;
68     crack_ratio=aa_fit/W;
69     f_aW=geometric(crack_ratio);
70     delK(i)=delP(i)*48*f_aW/(B*W^1.5*sqrt(1000));
71 end
72 dadn=dadn(dadn~=0);
73 delK=delK(delK~=0);

```

Table E-4: Sample data after final step

da/dn	ΔK
4.29e-06	9.12029223708689
4.37e-06	9.14054981792035
4.44e-06	9.16088960708057
4.44e-06	9.17903680305518
4.40e-06	9.19601403510931
4.28e-06	9.21523417956377

Appendix F

Precision and accuracy

Like most scientific studies, the measurements in this project also involved both systematic and random errors. The source of these errors were mainly in the crack length acquisition by the DCPD. The systematic errors arose from the calibration of the DCPD however separating the random component from this measurement is not straightforward. The randomness of the measurements comes from multiple steps. The method of making reference marks at regular intervals on the specimen is the first source of error. This reference marks were made with a height-meter which was basically a vertical ruler. It is possible that the marks could be underestimated or overestimated leading to errors in crack length. This is a random error. The second source of error is the visual estimation from these reference marks as these could also be underestimated or overestimated. This is also an random error. The third source of error is the precision of the DCPD. This is calculated from the scatter in the DCPD signal at a constant crack length and is considered as a systematic error.

The first two error are generally not separable and are calculated together. The error is calculated by measuring the reported crack lengths after tests. Although this still involves some error in visual estimation, this is assumed to be significantly less as compared to previous errors. This measurement is treated as the absolute value. This is shown in the table below.

Table F-1: Average Error in crack-length measurement indifferent groups

Specimen	Grain Orientation	Average Error
As Processed-C	Coarse Grain- Perpendicular to crack	0.06 mm
As Processed-D	Coarse Grain-Parallel to crack	0.07 mm
As Processed-E	Fine Grain	0.11 mm
HIP+H/T-C	Coarse Grain- Perpendicular to crack	0.08 mm
HIP+H/T-D	Coarse Grain-Parallel to crack	0.05 mm
HIP+H/T-E	Fine Grain	0.11 mm

The precision of the DCPD is calculated to be within 0.12%.

Fatigue plots of graded specimens

G-1 As processed

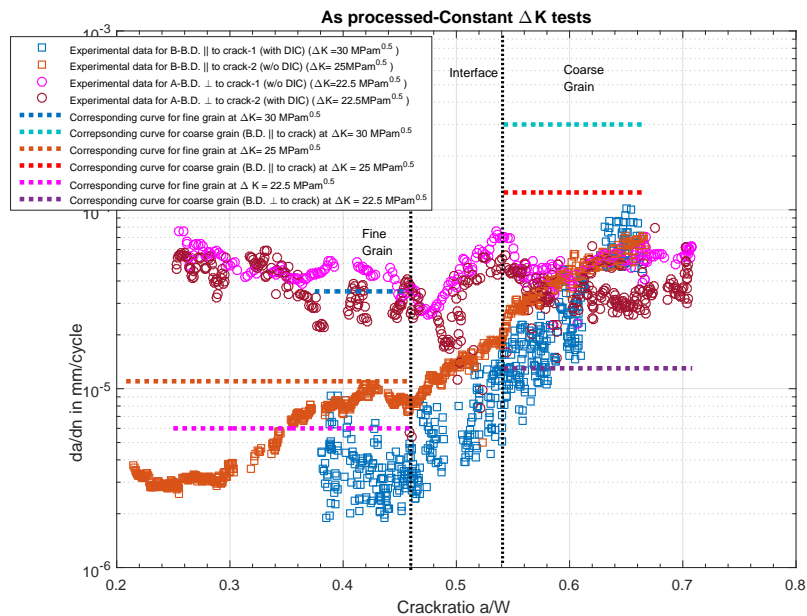


Figure G-1: Fatigue crack growth rate da/dn under constant ΔK as a function of crack ratio in as-processed-A and B specimens.

G-2 HIP+H/T

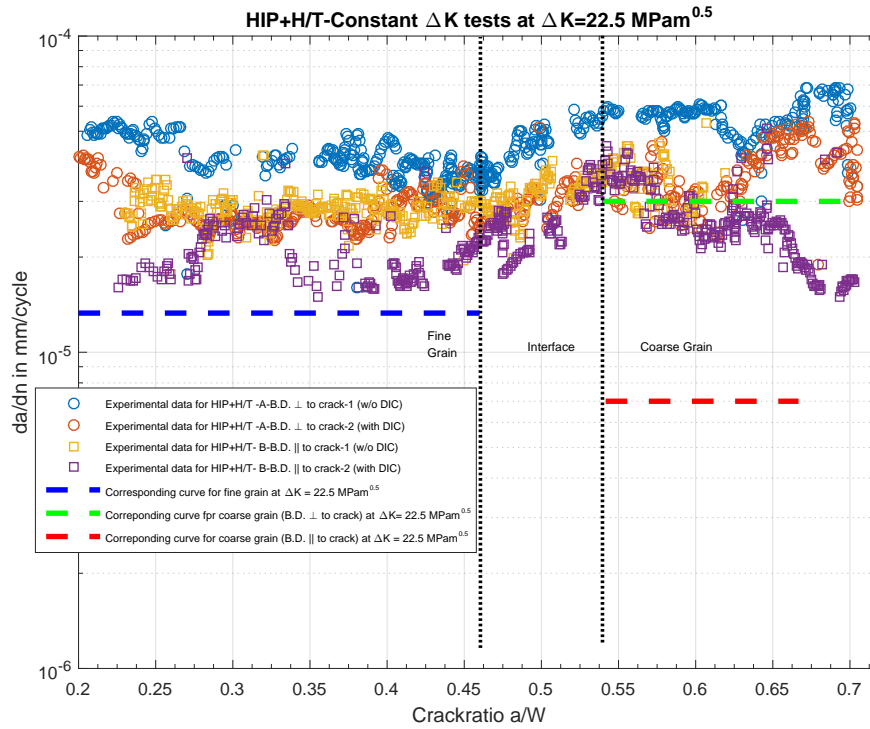


Figure G-2: Fatigue crack growth rate da/dn under constant ΔK as a function of crack ratio in HIP+H/T-A and B specimens.

Bibliography

- [1] A. Lingenfelter, "Welding of inconel alloy 718: A historical overview," *Superalloy 718*, vol. 718, pp. 673–683, 1989.
- [2] J. Franklin and W. Savage, "Stress relaxation and strain age cracking in rene 41 weldments," in *55th AWS Annual Meeting*, 1974.
- [3] B. G. Muralidharan, V. Shankar, and T. P. S. Gill, "Weldability of inconel 718-a review, department of atomic energy, government of india, kalpakkam," 1996.
- [4] H. Eiselstein, "Metallurgy of columbium hardened nickel-chromium-iron alloy," in *Advances in the Technology of Stainless Steels and Related Alloys and Committee-A10*, pp. 62–79, ASTM International, 1965.
- [5] G. Cao, T. Sun, and C. Wang, "Investigations of γ' , γ'' and δ precipitates in heat-treated inconel 718 alloy," *Materials Characterization*, vol. 136, pp. 398–406, 2018.
- [6] X. You, Y. Tan, and S. Shi, "Effect of solution heat treatment on the precipitation behavior and strengthening mechanisms of electron beam smelted inconel 718 superalloy," *Material Science & Engineering A*, vol. 689, pp. 257–268, 2017.
- [7] Z. Wang, K. Guan, and M. Gao, "The microstructure and mechanical properties of deposited-in718 by selective laser melting," *Journal of Alloys and Compounds*, vol. 513, pp. 518–523, 2012.
- [8] A. Mostafa, I. Rubio, and V. Brailovski, "Structure, texture and phases in 3d printed in718 alloy subjected to homogenization and hip treatments," *Metals*, vol. 7, no. 6, p. 196, 2017.
- [9] D. Deng, R. Peng, H. Brodin, and J. Moverare, "Microstructure and mechanical properties of Inconel 718 produced by selective laser melting: Sample orientation dependence and effects of post heat treatments," *Materials Science & Engineering A*, vol. 713, pp. 294–306, 2018.

- [10] X. Li, J. Shi, C. H. Wang, G. Cao, A. Russell, Z. Zhou, C. Li, and G. Chen, "Effect of heat treatment on microstructure evolution of inconel 718 alloy fabricated by selective laser melting," *Journal of alloys and compounds*, vol. 764, pp. 639–649, 2018.
- [11] D. Zhang, W. Niu, X. Cao, and Z. Liu, "Effect of standard heat treatment on the microstructure and mechanical properties of selective laser melting manufactured inconel 718 superalloy," *Materials Science & Engineering A*, vol. 644, pp. 32–40, 2015.
- [12] M. Sundaraman, P. Mukhopadhyay, and S. Banerjee, *Carbide precipitation in nickel base superalloys 718 and 625 and their effect on mechanical properties*, pp. 367–378. The Minerals, Metals & Materials Society, 1997.
- [13] V. A. Popovich, E. Borisov, A. Popovich, V. Sufiarov, D. Masaylo, and L. Arzina, "Impact of heat treatment on mechanical behaviour of Inconel 718 processed with tailored microstructure by selective laser melting," *Materials and Design*, vol. 131, pp. 12–22, 2017.
- [14] M. Chaturvedi and Y. Han, "Strengthening mechanisms in inconel 718," *Metal Science*, vol. 17, no. 3, pp. 145–149, 1983.
- [15] J. Oblak, D. Paulonis, and D. Duvall, "Coherency strengthening in ni base alloys hardened by d022 precipitates," *Metallurgical Transactions*, vol. 5, pp. 143–153, 1974.
- [16] S. M. Corporation, "Inconel 718," September 2007.
- [17] R. Hayes, "Creep deformation of inconel alloy 718 in the 650°C to 760°C temperature regime," *Superalloys 718*, vol. 625, 1991.
- [18] H. L. Eiselstein, "Age hardenable nickel alloy," 1962.
- [19] S. Singh and J. Andersson, "Hot cracking in cast alloy 718," *Science and Technology of Welding and Joining*, vol. 23, no. 7, pp. 568–574, 2018.
- [20] E. A. Loria, "The status and prospects of alloy 718," *Journal of Metals*, vol. 40, no. 7, pp. 36–41, 1988.
- [21] E. Akca and A. Gursel, "A review on superalloys and in718 nickel-based inconel superalloy," *Periodicals of Engineering and Natural Sciences*, vol. 3, no. 1, 2015.
- [22] A. F. Giamei, "Development of single crystal superalloys: a brief history," *Adv. Mater. Process*, vol. 171, no. 9, pp. 26–30, 2013.
- [23] ASTM, *Standard Terminology for Additive Manufacturing Technologies (Withdrawn 2015)*. F2792-12a, ASTM International, 2015.
- [24] R. C. Benn and R. P. Salva, "Additively manufactured inconel® alloy 18," in *7th International Symposium on Superalloy 718 and its derivatives*, 2010.
- [25] ISO/ASTM, *Additive manufacturing — General principles — Terminology*. 52900:2015, International Organization for Standardization, 2015.
- [26] Wikipedia, "Selective laser melting." https://en.wikipedia.org/wiki/Selective_laser_melting, accessed 18.02.2019.

-
- [27] Coating-Competence-center, “Selective laser melting.” <https://www.empa.ch/web/coating-competence-center/selective-laser-melting>, accessed 17.02.2019.
- [28] S. Kumar, *Selective Laser Melting*, ch. 10.05, pp. 93–134. Elsevier Ltd, 2014.
- [29] R. Konecna, G. Nicoletto, L. Kunz, and A. Baca, “Microstructure and directional fatigue behaviour of inconel 718 produced by selective laser melting,” *Procedia structural integrity*, vol. 2, pp. 2381–2388, 2016.
- [30] H. Wan, Z. Zhou, C. Li, and G. Chen, “Enhancing fatigue strength of selective laser melting-fabricated inconel 718,” *Advanced Engineering Materials*, vol. 20, 2018.
- [31] M. Aydinöz, F. Brenne, M. Schaper, C. Schaak, W. Tillmann, J. Nellesen, and T. Nien-dorf, “On the microstructural and mechanical properties of post-treated additively man-ufactured Inconel718 superalloy under quasi-static and cyclic loading,” *Materials Science & Engineering A*, vol. 669, pp. 246–258, 2016.
- [32] W. M. Tucho, P. Cuvillier, A. Sjolyst-Kverneland, and V. Hansen, “Microstructure and hardness studies of Inconel 718 manufactured by selective laser melting before and after solution heat treatment,” *Materials Science & Engineering A*, vol. 689, pp. 220–232, 2017.
- [33] B. Zhang, Y. Li, and Q. Bai, “Defect formation mechanisms in selective laser melting : A review,” *Chinese journal of Mechanical Engineering*, vol. 20, no. 3, pp. 515–527, 2017.
- [34] X. G. XiaoqingWang and K. Chou, “Review on powder-bed laser additive manufac-turing of inconel 718 parts,” *Journal of Engineering Manufacture*, vol. 231, no. 11, p. 1890–1903, 2017.
- [35] T. Raza, J. Andersson, and L. Svensson, “Microstructure of selective laser melted alloy 718 in as-manufactured and post heat treated conditions,” *Procedia Manufacturing*, vol. 25, pp. 450–458, 2018.
- [36] D. Deng, *Additively Manufactured Inconel 718 Microstructure and Mechanaical Proper-ties*. Linköping University, 2018.
- [37] A. Yadollahi, M. Mahtabi, A. Khalili, H. Doude, and J. N. Jr, “Fatigue life prediction of additively manufactured material: Effects of surface roughness, defect size, and shape,” *Fatigue and Fracture of Enineering Materials and Structures*, vol. 41, no. 7, pp. 1602–1614, 2018.
- [38] A. Balachandramurthi, J. Moverare, N. Dixit, and R. Pederson, “Influence of defects and as-built surface roughness on fatigue properties of additively manufactured alloy718,” *Materials Science & Engineering A*, vol. 735, pp. 463–474, 2018.
- [39] M. Ni, C. Chen, X. Wang, P. Wang, R. Li, X. Zhang, and K. Zhou, “Anisotropic tensile behavior of in situ precipitation strengthened Inconel 718 fabricated by additive manufacturing,” *Materials Science & Engineering A*, vol. 701, pp. 344–351, 2017.

- [40] M. Kirka, D. Greeley, C. Hawkins, and R. Dehoff, "Effect of anisotropy and texture on the low cycle fatigue behavior," *International Journal of Fatigue*, vol. 105, pp. 235–243, 2017.
- [41] S. International, *Nickel Alloy, Corrosion and Heat Resistant, Bars, Forgings, and Rings 52.5Ni 19Cr 3.0Mo 5.1Cb 0.90Ti 0.50Al 19Fe, Consumable Electrode or Vacuum Induction Melted 1775° F (968° C) Solution and Precipitation Heat Treated*. AMS5663, SAE International, 1965.
- [42] S. International, *Nickel Alloy, Corrosion and Heat-Resistant, Investment Castings, 52.5Ni - 19Cr - 3.0Mo - 5.1Cb(Nb) - 0.90Ti - 0.60Al - 18Fe, Vacuum Melted Homogenization and Solution Heat Treated*. AMS5383, SAE International, 1966.
- [43] S. International, *Metal Injection Molded Nickel Based Alloy 718 Parts Hot Isostatically Pressed, Solutioned and Aged*. AMS5917, SAE International, 2017.
- [44] M. D. Sangid, T. A. Book, D. Naragani, J. Rotella, P. Ravi, P. Kenesei, J. S. Park, H. Sharma, J. Almer, and X. Xiao, "Role of heat treatment and build orientation in the microstructure sensitive deformation characteristics of in718 produced via slm additive manufacturing," *Additive Manufacturing*, vol. 22, pp. 479–496, 2018.
- [45] J. Li, Z. Zhao, P. Bai, H. Qu, B. Liu, and L. Li, "Microstructural evolution and mechanical properties of IN718 alloy fabricated by selective laser melting following different heat treatments," *Journal of Alloys and Compounds*, vol. 772, pp. 861–870, 2019.
- [46] W. Tillmann, C. Schaak, J. Nellesen, M. Schaper, M. Aydinöz, and K. Hoyer, "Hot isostatic pressing of IN718 components manufactured by selective laser melting," *Additive Manufacturing*, vol. 13, pp. 93–102, 2017.
- [47] R. Seede, A. Mostafa, V. Brailovski, M. Jahazi, and M. Medraj, "Microstructural and microhardness evolution from homogenization and hot isostatic pressing on selective laser melted inconel 718: Structure, texture, and phases," *Journal of Manufacturing and Materials Processing*, vol. 2, no. 2, p. 30, 2018.
- [48] A. Mitchell, "Primary carbides in alloy 718," in *7th International Symposium on Superalloy 718 and its Derivatives*, 2010.
- [49] Y. L.Kuo, T. Nagahari, and K. Kakehi, "The effect of post-processes on the microstructure and creep properties of alloy718 built up by selective laser melting," *Materials*, vol. 11, no. 6, 2018.
- [50] A. S. JOHNSON, S. SHAO, N. SHAMSAEI, S. M. THOMPSON, and L. BIAN, "Microstructure, fatigue behavior, and failure mechanisms of direct laser-deposited inconel 718," *Journal of Metals*, vol. 69, no. 3, pp. 597–603, 2017.
- [51] S. Gribbin, J. Bicknell, L. Jorgensen, I. Tsukrov, and M. Knezevic, "Low cycle fatigue behavior of direct metal laser sintered inconel alloy 718," *International Journal of Fatigue*, vol. 93, pp. 156–167, 2016.
- [52] O. SCOTT-EMUAKPOR, J. SCHWARTZ, T. GEORGE, C.HOLYCROSS1, C. CROSS, and J. SLATER, "Bending fatigue life characterisation of direct metal laser

- sintering nickel alloy,” *Fatigue and Fracture of Engineering Materials & Structures*, vol. 718, no. 38, pp. 1105–1117, 2015.
- [53] E. Amsterdam, “Evaluation of the microstructure and mechanical properties of laser additive manufactured gas turbine alloys ti-6al-4v and inconel 718,” 2009.
- [54] U. Krupp, *Fatigue Crack Propagation in Metals and Alloys*. Osnabruck: Wiley-VCH, 2006.
- [55] A. Shyam and W. Milligan, “A model for slip irreversibility, and its effect on the fatigue crack propagation threshold in a nickel-base superalloy,” *Acta Materialia*, vol. 53, p. 835–844, 2005.
- [56] H. Mughrabi, “Cyclic slip irreversibility and fatigue life: A microstructure-based analysis,” *Acta Materialia*, vol. 61, pp. 1197–1203, 2013.
- [57] H. Ho, M. Risbet, and X. Feaugas, “A cyclic slip irreversibility based model for fatigue crack initiation of nickel base alloys,” *International Journal of Fatigue*, vol. 102, pp. 1–8, 2017.
- [58] M. Clavel and A. Pineau, “Fatigue behaviour of two nickel-base alloys i: Experimental results on low cycle fatigue, fatigue crack propagation and substructures,” *Materials Science and Engineering*, vol. 55, pp. 157–171, 1982.
- [59] S. Tammam-Williams, P. J. Withers, I. Todd, and P. B. Prangnell, “The effectiveness of hot isostatic pressing for closing porosity in titanium parts manufactured by selective electron beam melting,” *Metallurgical and Materials Transactions A*, vol. 47, no. 5, pp. 1939–1946, 2016.
- [60] J. Miao, T. M. Pollock, and J. W. Jones, “Microstructural extremes and the transition from fatigue crack initiation to small crack growth in a polycrystalline nickel-base superalloy,” *Acta Materialia*, vol. 60, pp. 2840–2854, 2012.
- [61] J. An, L. Wang, Y. Liu, W. Cai, and X. Song, “The role of δ phase for fatigue crack propagation behavior in a ni base superalloy at room temperature,” *Materials Science & Engineering A*, vol. 684, pp. 312–317, 2017.
- [62] M. Abikchi, T. Billot, J. Crépin, A. Longuet, C. Mary, T. F. Morgeneyer, and A. Pineau, “Fatigue life and initiation mechanisms in wrought inconel 718 da for different microstructures,” in *13th international conference on fracture*, 2013.
- [63] M. Janssen, J. Zuidema, and R. Wanhill, *Fracture Mechanics*. VSSD, 2006.
- [64] R. Konecná, L. Kunz, G. Nicoletto, and A. Baca, “Long fatigue crack growth in inconel 718 produced by selective laser melting,” *International Journal of Fatigue*, vol. 92, pp. 499–506, 2016.
- [65] K. Miller, “Metal fatigue-past current and future,” *Proceedings of the Institution of Mechanical Engineers, Part C: Mechanical Engineering Science*, vol. 205, no. 5, pp. 291–304, 1991.

- [66] Y. S. J. Yoo, T. A. Book, M. D. Sangid, and J. Kachera, "Identifying strain localization and dislocation processes in fatigued inconel 718 manufactured from selective laser melting," *Materials Science & Engineering A*, vol. 724, pp. 444–451, 2018.
- [67] C. Mercer, A. Soboyejo, and W. Soboyejo, "Micromechanisms of fatigue crack growth in a forged inconel 718 nickel-based superalloy," *Materials Science & Engineering A*, vol. 270, pp. 308–322, 1999.
- [68] H. Andersson and C. Persson, "In-situ sem study of fatigue crack growth behaviour in in718," *International Journal of Fatigue*, vol. 26, pp. 211–219, 2004.
- [69] Y. Shinohara, *Functionally Graded Materials*, pp. 1179–1187. Elsevier Inc., 2013.
- [70] J. J. Sobczak and L. Drenchev, "Metallic functionally graded materials: A specific class of advanced composites," *Journal of Material Science and Technology*, vol. 29, no. 4, pp. 297–316, 2013.
- [71] K. K. Pradhan and S. Chakraverty, *Overview of Functionally graded materials*, pp. 1–10. Academic press, 2019.
- [72] G. Udupa, S. Rao, and K. Gangadharan, "Functionally graded composite materials: An overview," *Procedia Materials Science*, vol. 5, pp. 1291–1299, 2014.
- [73] M. Naebe and K. Shirvanimoghaddam, "Functionally graded materials: A review of fabrication and properties," *Applied Materials Today*, vol. 5, pp. 223–245, 2016.
- [74] G. H. Loha, E. Pei, D. Harrison, and M. D. Monzón, "An overview of functionally graded additive manufacturing," *Additive Manufacturing*, vol. 23, pp. 34–44, 2018.
- [75] C. Zhang, F. Chen, Z. H. M. Jia, G. Chen, Y. Ye, Y. Lin, W. Liu, B. Chen, Q. Shen, L. Zhang, and E. J. Lavernia, "Additive manufacturing of functionally graded materials: A review," *Materials Science & Engineering A*, vol. 764, p. 138209, 2019.
- [76] X. Qian and D. Dutta, "Design of heterogenous turbine blades," *Computer-Aided Design*, vol. 35, pp. 319–329, 2003.
- [77] P. Muller, P. Mognol, and J. Y. Hascoet, "Modeling and control of a direct laser powder deposition process for functionally graded materials (fgm) parts manufacturing," *Journal of Materials Processing Technology*, vol. 213, pp. 685–692, 2013.
- [78] V. Popovich, E. Borisov, A. Popovich, V. Sufiarov, D. V. Masaylo, and L. Alzina, "Functionally graded inconel 718 processed by additive manufacturing: Crystallographic texture, anisotropy of microstructure and mechanical properties," *Materials and Design*, vol. 114, pp. 441–449, 2017.
- [79] V. E. Beal, P. Erasenthiran, N. Hopkinson, P. Dickens, and C. H. Ahrens, "The effect of scanning strategy on laser fusion of functionally graded H13/cu materials," *The International Journal of Advanced Manufacturing Technology*, vol. 30, pp. 844–852, 2006.
- [80] X. Wu, P. Jiang, L. Chen, F. Yuan, and Y. T. Zhu, "Extraordinary strain hardening by gradient structure," *Proceedings of the National Academy of Sciences*, vol. 111, pp. 7197–7201, 2014.

-
- [81] X. L. Wu, P. Jiang, L. Chen, J. F. Zhang, F. P. Yuan, and Y. T. Zhu, "Synergetic strengthening by gradient structure," *Materials Research Letters*, vol. 2, pp. 185–191, 2014.
- [82] M. Huang, C. Xu, G. Fan, E. Maawad, W. Gan, and L. Geng, "Role of layered structure in ductility improvement of layered ti-al metal composite," *Acta Materiala*, vol. 153, pp. 235–249, 2018.
- [83] C. Shao, P. Zhang, Y. Zhu, Z. Zhang, Y. Tian, and Z. Zhang, "Simultaneous improvement of strength and plasticity: Additional work-hardening from gradient microstructure," *Acta Materiala*, vol. 145, pp. 413–428, 2018.
- [84] N. Guo, Z. Zhang, Q. Dong, H. Yu, B. Song, L. Chai, and C. Liu, "Strengthening and toughening austenitic steel by introducing gradient martensite via cyclic forward/reverse torsion," *Materials and Design*, vol. 143, pp. 150–159, 2018.
- [85] M. BENEDETTI, J. HEIDEMANN, J. O. PETERS, and G. LÜTJERING, "Influence of sharp microstructural gradients on the fatigue crack growth resistance of $\alpha+\beta$ and near- α titanium alloys," *Fatigue & Fracture of Engineering Materials & Structures*, vol. 28, no. 10, pp. 909–922, 2005.
- [86] S. Zhang, J. Xie, Q. Jiang, X. Zhang, C. Sun, and Y. Hong, "Fatigue crack growth behavior in gradient microstructure of hardened surface layer for an axle steel," *Materials Science & Engineering A*, vol. 700, pp. 66–74, 2017.
- [87] Z. Ma, J. Liu, G. Wang, H. Wang, Y. Wei, , and . H. Gao, "Strength gradient enhances fatigue resistance of steels," *Scientific Reports*, vol. 6, p. 22156, 2016.
- [88] F. Erdogan, "Fracture Mechanics of functionally graded materials," *Composites Engineering*, vol. 5, no. 7, pp. 753–770, 1995.
- [89] F. Delale and F. Erdogan, "The crack problem for a nonhomogeneous plane," *Journal of Applied Mechanics*, vol. 50, no. 3, pp. 609–614, 1983.
- [90] J. W. Eischen, "Fracture of nonhomogenous materials," *International journal of fracture*, vol. 34, pp. 3–22, 1987.
- [91] Z.-H. Jin and N. Noda, "Crack-Tip Singular Fields in Nonhomogeneous Materials," *Journal of Applied Mechanics*, vol. 61, pp. 738–740, 09 1994.
- [92] P. Gu, M. Dao, and R. J. Asaro, "A Simplified Method for Calculating the Crack-Tip Field of Functionally Graded Materials Using the Domain Integral," *Journal of Applied Mechanics*, vol. 66, pp. 101–108, 03 1999.
- [93] J.-H. Kim and G. H. Paulino, "Finite element evaluation of mixed mode stress intensity factors in functionally graded materials," *International Journal for Numerical Methods in Engineering*, vol. 53, no. 8, pp. 1903–1935, 2002.
- [94] K. R. CHANDRAN and I. BARSOUM, "Determination of stress intensity factor solutions for cracks in finite-width functionally graded materials," *International Journal of Fracture*, vol. 121, pp. 183–203, 2003.

- [95] G. Irwin, "Analysis of stresses and strains near the end of a crack traversing a plate," *ASME Journal of Applied Mechanics*, vol. 24, pp. 354–361, 1957.
- [96] G. Vander Voort and E. Manilova, "Metallographic techniques for superalloys," *Microscopy and Microanalysis - MICROSC MICROANAL*, vol. 10, 08 2004.
- [97] ASTM-E399-19, *Standard Test Method for Linear-Elastic Plane-Strain Fracture Toughness K_{Ic} of Metallic Materials*. ASTM International, 2019.
- [98] W. A. Herman, R. W. Hertzberg, and R. Jaccard, "A simplified laboratory approach for the prediction of short crack behavior in engineering structures," *Fatigue & Fracture of Engineering Materials & Structures*, vol. 11, no. 4, pp. 303–320, 1988.
- [99] R. Pippin, H. Stüwe, and K. Golos, "A comparison of different methods to determine the threshold of fatigue crack propagation," *International Journal of Fatigue*, vol. 16, no. 8, pp. 579 – 582, 1994.
- [100] ASTM-E647-15e1, *Standard Test Method for Measurement of Fatigue Crack Growth Rates*. ASTM International, 2015.
- [101] H.-Y. Wan, Z.-J. Zhou, C.-P. Li, G.-F. Chen, and G.-P. Zhang, "Enhancing fatigue strength of selective laser melting-fabricated inconel 718 by tailoring heat treatment route," *Advanced Engineering Materials*, vol. 20, no. 10, p. 1800307, 2018.
- [102] X. Wang and K. Chou, "The effects of stress relieving heat treatment on the microstructure and residual stress of inconel 718 fabricated by laser metal powder bed fusion additive manufacturing process," *Journal of Manufacturing Processes*, vol. 48, pp. 154 – 163, 2019.
- [103] L. Kolbus, E. Payzant, P. Cornwell, T. Watkins, S. Babu, R. Dehoff, M. Lorenz, O. Ovchinnikova, and C. Duty, "Comparison of residual stresses in inconel 718 simple parts made by electron beam melting and direct laser metal sintering," *Metallurgical and Materials Transactions A*, vol. 46, p. 1419, 03 2015.
- [104] J. Yoon, N. Kim, J. Kim, J.-T. Yeom, and N.-K. Park, "Recrystallization and grain growth behavior of alloy 718 casting during hot working," *Key Engineering Materials - KEY ENG MAT*, vol. 345-346, pp. 57–60, 01 2007.
- [105] R. Barros, F. J. Silva, R. M. Gouveia, A. Saboori, G. Marchese, S. Biamino, A. Salmi, and E. Atzeni, "Laser powder bed fusion of inconel 718: Residual stress analysis before and after heat treatment," *Metals*, vol. 9, no. 12, p. 1290, 2019.
- [106] P. Liu, S.-y. Sun, S.-b. Xu, M.-q. Cao, C. Hong, and J.-y. Hu, "Effect of Solid Solution + Double Ageing on Microstructure and Properties in the Layer by Layer of the Z-Y Interface of Inconel 718 alloys Fabricated by SLM," *Materials Research*, vol. 21, 00 2018.
- [107] J. Wasén, K. Hamberg, and B. Karlsson, "The influence of grain size and fracture surface geometry on the near-threshold fatigue crack growth in ferritic steels," *Materials Science and Engineering: A*, vol. 102, no. 2, pp. 217 – 226, 1988.

- [108] J. E. King, "Effects of grain size and microstructure on threshold values and near threshold crack growth in powder-formed ni-base superalloy," *Metal Science*, vol. 16, no. 7, pp. 345–355, 1982.

